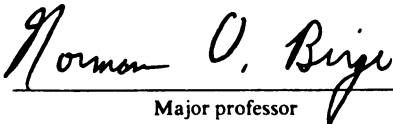This is to certify that the

dissertation entitled

Response of the Conductance and
Tunneling System Dynamics in
Mesoscopic Bismuth to Applied
Mechanical Strain

presented by

David William Hoadley

has been accepted towards fulfillment
of the requirements for

____Ph.D.____ degree in ___Physics___

Norman O. Birge

Major professor

Date___12/8/1999___

PLACE IN RETURN BOX to remove this checkout from your record.
TO AVOID FINES return on or before date due.
MAY BE RECALLED with earlier due date if requested.

DATE DUE	DATE DUE	DATE DUE

11/00   c:/CIRC/DateDue.p65-p.14

RESPONSE OF THE CONDUCTANCE AND TUNNELING SYSTEM DYNAMICS
IN MESOSCOPIC BISMUTH TO APPLIED MECHANICAL STRAIN

By

David William Hoadley

A DISSERTATION

Submitted to
Michigan State University
in partial fulfillment of the requirements
for the degree of

DOCTOR OF PHILOSOPHY

Department of Physics and Astronomy

1999

ABSTRACT

RESPONSE OF THE CONDUCTANCE AND TUNNELING SYSTEM DYNAMICS
IN MESOSCOPIC BISMUTH TO APPLIED MECHANICAL STRAIN

By

David William Hoadley

We have introduced mechanical strain to mesoscopic bismuth wires at low

temperature as a new experimental tool. Typical samples have dimensions of 1.5μm x

70nm x 25nm and electrical resistances of 10-20 kΩ. We introduce strain by attaching

the substrate to a PZT-5A piezoelectric wafer. Our observations showed that the

conductance of the wires varies randomly but reproducibly with strain, in a manner

reminiscent of Universal Conductance Fluctuations. Surprisingly, application of strains

($\Delta L/L$) as small as 10^{-6} can change the conductance by order of e^2 / h below

temperatures of 100 mK. In addition to these static fluctuations, the wires exhibit

dynamic fluctuations seen as random telegraph signals in the conductance. These

dynamic fluctuations, due to the motion of two-level tunneling systems (TLS), vary in

both amplitude and switching rate under strain. The amplitude variation is random, while

the tunneling rates vary in a systematic way. The response of a TLS to strain in lowest

order is described by the deformation potential for the asymmetry, ε: $\gamma \equiv \dfrac{1}{2}\dfrac{d\varepsilon}{d\sigma}$, where σ

is dimensionless strain. We have made the first observations of this response to strain for individual TLS's, and compare our results to those of measurements in bulk glass samples. In our experiments, γ varied from 0 to 1.7 eV.

To Leah, my love

ACKNOWLEDGEMENTS

TABLE OF CONTENTS

LIST OF TABLES

LIST OF FIGURES

Chapter 1

Introduction

Before the 1970's, it had been expected that at low temperatures, the differences in physical properties between crystalline and amorphous solids would disappear. As temperature was lowered, the dominant phonon wavelengths would become much longer than the average inter-atomic spacing. At very low temperatures, insulating glasses could then be described as Debye solids, with phonon specific heat proportional to T^3 [Ashcroft & Mermin]. Experiments on a glass in 1971 showed, however, that there was a contribution to the specific heat linear with temperature below 1K [Zeller and Pohl]. This was the first evidence that amorphous solids contain a fundamental set of excitations not present in their highly ordered, crystalline counterparts. The disordered nature of such solids produces many atomic-sized configurations with two or more potential energy local minima. The tunneling model [Phillips, 1972] [Anderson, et al.] describes these excitations as two-level systems (TLS) that tunnel between configurations with a broad probability distribution in energy and tunneling matrix element. At very low temperatures, these tunneling systems produce an observable quasi-linear contribution to the specific heat of glasses.

The tunneling model predicts other features of the low-temperature thermal and acoustic properties of amorphous materials. The distribution of TLS excitations gives

rise to anomalous thermal conductivity [Zaitlin and Anderson], phonon attenuation [Arnold, et al.], and sound velocity dispersion [Piché, et al.]. Another dramatic result was the observation of phonon echoes produced with a series of ultrasonic pulses [Golding and Graebner].

Disordered metals also exhibit properties that can be explained by a broad distribution of disorder-induced excitations. The presence of quasiparticles in normal metals makes it difficult to measure the effects of TLS on thermal and acoustic properties, however. The TLS linear specific heat contribution, for example, is much smaller than that of electrons. Successful measurements of the TLS contributions were made in disordered metals below the normal-superconductor transition temperature [Graebner et al., 1977] [Weiss and Golding].

A large body of experimental work supports the tunneling model idea and shows that disorder produces a fundamental set of excitations in solids [Phillips, 1981]. Thermal and acoustic measurements provide information about the distribution of these excitations and also about their interactions with phonons. These bulk experiments can only probe the average parameters of the TLS, however. Any such bulk measurement returns information that is averaged over the distribution of tunneling parameters for the TLS's. Therefore, 20 years after their discovery, little was known about the detailed nature of these two-level systems.

In the late 1980's, advances in the fabrication and understanding of sub-micron sized metallic samples opened the door to a new approach to studying TLS. In a metallic sample at low-temperature, the electrical conductance becomes sensitive to the motion of scatterers, such as impurities or lattice dislocations. Long-range electron phase coherence

enhances the change in conductance produced by mobile defects. This enhancement is maximized when electrons can coherently travel through a sample for most or all of its extent, a situation known as the mesoscopic regime. There, the motion of individual, atomic-sized scatterers can produce measurable changes in the conductance of a sample, as predicted by the theories of Quantum Transport [Al'tshuler and Spivak] [Feng, et al.]. It is in a mesoscopic metallic sample that we have the unique opportunity to observe the motion of an individual TLS.

The dynamics of individual mobile defects have been successfully studied in this decade. The variation of TLS tunneling rates with temperature has been observed [Golding et al., 1992] [Chun and Birge, 1993]. As we will discuss in chapter 2, these tunneling rates can have a novel temperature dependence in a dissipative environment, such as that provided by the quasiparticles in a metal [Leggett et al.]. Once the TLS dynamics were understood, observations focused on the effects of external perturbations. Magnetic fields were shown to modify TLS dynamics in a mesoscopic metal through changes induced in their environments [Zimmerman, et al.]. The energy coupling of a TLS to the quasiparticle bath was observed and the TLS was used as a thermometer in an electron heating experiment [Chun and Birge, 1994].

To probe the TLS more deeply, we have examined their response to externally applied mechanical strain. From thermal and acoustic measurements on bulk samples, we have seen that the TLS have a strong coupling to strain realized as phonons [Beret and Meissner]. By studying the dynamics of individual two-level systems, we can unambiguously see how the microscopic potential of a TLS couples to strain.

I will also describe here the first observation of strain-induced conductance fluctuations in a mesoscopic metallic sample [Birge, et al., 1996]. These fluctuations are random, reproducible changes in conductance similar in character to those induced by varying chemical potential [Skocpol, et al.] [Licini, et al.] or applied magnetic field [Umbach, et al.].

The Thesis is organized as follows: Chapter 2 gives an introduction to the Tunneling Model and identifies many of its consequences for the thermal and acoustic properties of amorphous solids. Predictions based on the distribution of TLS's in glasses and their interactions with phonons are described, and examples are given of observations of these. The theory of Dissipative Quantum Tunneling is also presented in Chapter 2. It describes the modifications of the dynamics of a tunneling TLS due to the presence of quasiparticles in a metal. Chapter 3 focuses on the implications of long-range electron phase-coherence in a disordered metal. There I describe in detail several Quantum Transport theories, including the mechanism that allowed us to observe individual TLS tunneling from state to state via changes in the sample's conductance. Chapter 4 describes some details about the experimental techniques and sample preparation. In Chapter 5, I describe the first observation of random, reproducible strain-induced conductance fluctuations. Chapter 6 is the main result of the work, and in it I present detailed results on the first measurements of the effect of strain on the dynamics of individual TLS. Chapter 7 concludes the body of the Thesis, and the Appendix describes the low-temperature calibration process for strain that was applied to the sample.

4

Chapter 2

Tunneling, Two-Level Systems

I.   Tunneling Model

There is a large body of work, which began in the early 1970s, that is concerned

with the thermal and acoustic properties of amorphous insulators at low temperatures.

There we see the effects of a fundamental set of excitations not present in crystalline

solids, which have long range order. For example, the linear specific heat anomaly,

observed first in vitreous silica glass below 1K [Zeller and Pohl], can not be described by

conventional lattice contributions. The well-known result for the (Debye) phonon

specific heat in a crystal lattice at very low temperatures is

$$c_v \approx \frac{2\pi^2}{5} k_B \left(\frac{k_B T}{\hbar c} \right)^3 \text{ [Ashcroft and Mermin].} \qquad (2.1)$$

Prior to the work of Zeller and Pohl, it had been expected that as the phonon wavelength

became much larger than the inter-atomic spacing, disorder would become decreasingly

important. The amorphous state of a material, at low enough temperatures, would feature

the same specific heat as its crystalline counterparts. After 1971, however, the specific

heat of many amorphous solids was seen to vary nearly linearly with temperature below

1K. In 1972, a model was developed by two groups [Anderson et al., 1972] [Phillips,

1972], that described the observed specific heat anomaly. There they show a specific

heat contribution nearly linear with temperature arising from a broad distribution of

excitations. These excitations are present due to the disorder inherent to the amorphous state and are identified as tunneling two-level systems (TLS). In a disordered solid, there are a vast number of structural configurations with energies very close to each other. Even at very low temperatures, the model assumes that some of these configurational states feature low enough potential barriers that transitions can occur via tunneling.

For simplicity, we will consider the problem of a single particle in a double-well potential. We model a TLS as shown in Figure 2.1. The abscissa represents a general configurational coordinate for the system, arising perhaps from the rearrangement of a few atoms in the solid. The two local minima differ in energy by ε, the asymmetry of the TLS potential. At low temperature, i.e. where kT << V, the dynamics are dominated by quantum mechanical tunneling. The Hamiltonian is given concisely by

$$H = \frac{1}{2}\varepsilon\sigma_z - \frac{1}{2}\Delta_0\sigma_x,$$ (2.2)

where σ_i are the Pauli spin matrices. We can express the tunneling matrix element as

$$\Delta_0 = \hbar\omega_0\, e^{-\lambda},$$ (2.3)

where ω_0 is the oscillation frequency in the well, and $\lambda \approx d \cdot \sqrt{\dfrac{2mV}{\hbar^2}}$ is given in one dimension by the WKB approximation, where m and d are the mass and separation between wells for the model single-particle problem. The energy eigenstates of this problem are readily determined. In the energy eigenstate basis, we have $H = \frac{1}{2}E\sigma_z$, and the energy eigenvalues are

$$\pm\frac{E}{2} = \pm\frac{1}{2}\left(\varepsilon^2 + \Delta_0^2\right)^{\frac{1}{2}}.$$ (2.4)
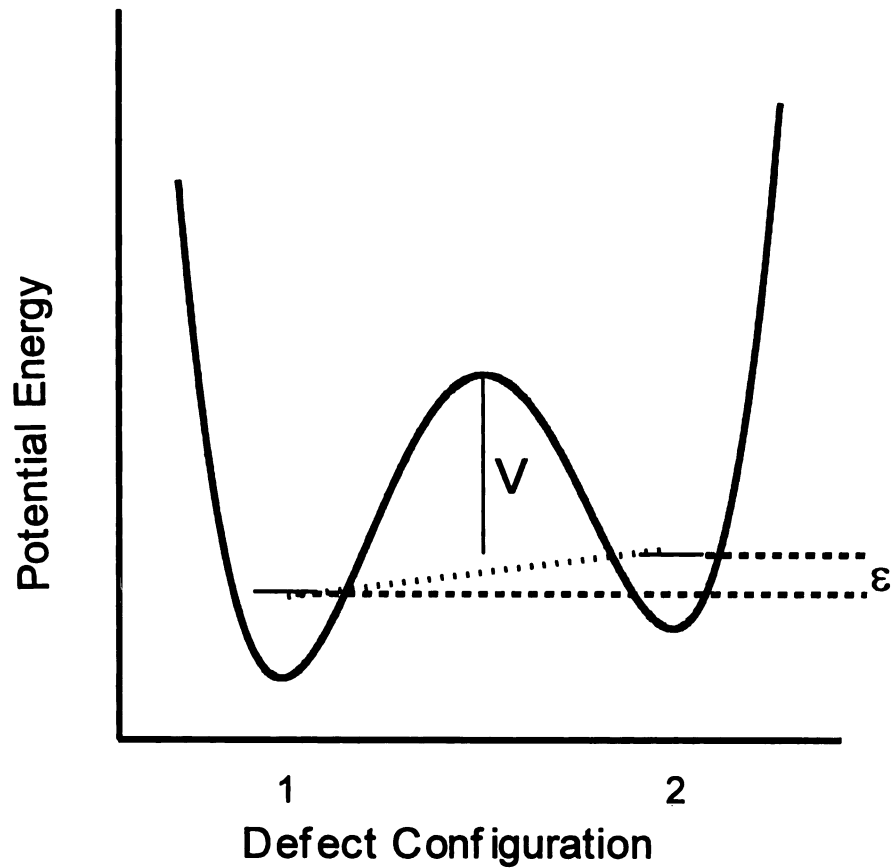
Figure 2.1 - Schematic of the Potential of a Two-Level System. Here we see a realization of the type of potential described by the tunneling model in amorphous solids. The abscissa represents a generalized configuration coordinate. In order that this describes a two-level system, we require that the potential barrier, V is much greater than $\hbar\omega_0$ for either well. In addition, the asymmetry, ε, and kT must be much smaller than V.

The eigenstates are linear combinations of the left and right states, given by

$$|\Psi_+\rangle = \cos\theta|l\rangle + \sin\theta|r\rangle$$
$$|\Psi_-\rangle = \sin\theta|l\rangle - \cos\theta|r\rangle$$
, where $\tan 2\theta = \frac{\Delta_0}{E}$. (2.5)

Note that the in the zero-bias case ($\varepsilon = 0$) we recover the familiar symmetric and anti-symmetric combinations.

II.   Thermal Properties

The Tunneling Model contains assumptions about the distribution of TLS present in an amorphous solid. The idea is that there is a wide distribution of such TLS, and that in the relevant range of energies and parameters, we can consider it to be constant as a function of asymmetry and tunneling parameter, $P(\varepsilon, \lambda) = \bar{P}$. TLS will exist that display asymmetries from zero to some fraction of the glass transition temperature, since this indicates the energy scale for the disorder present in the glassy state [Phillips, 1972]. Due also to the disordered nature of the solid, we expect a broad distribution of barrier heights ranging from 0 to the energy associated with the glass transition temperature ($\approx$ 0.1 eV in vitreous silica) [Anderson et al., 1972]. With this assumption, we can derive the contribution to the specific heat due to these excitations. For a single TLS, we have

$$F(E) = -k_B T \ln[2\cosh(E/k_B T)], \tag{2.6}$$

and

$$C(E) = -T \frac{\partial^2 F}{\partial T^2} = \frac{E^2}{k_B T^2} \text{sech}^2(E/k_B T). \tag{2.7}$$

For a distribution of independent tunneling states, n(E), we have that

$$C = \int_0^\infty C(E)n(E)dE = \int_0^\infty \frac{E^2}{k_B T^2} \text{sech}^2(E/k_B T)n(E)dE. \tag{2.8}$$

8

The integrand is large only when $E \approx kT$. If $n(E)=n_0$ is constant (or nearly so) near kT, we find, upon substitution with $x = E/k_B T$, that

$$C \approx n_0 k_B^2 T \int_0^\infty x^2 \operatorname{sech} x\, dx = \left(\frac{\pi^2}{12}\right) n_0 k_B^2 T \quad \text{[Phillips, 1972].} \quad (2.9)$$

This approximation for $n(E)$ deserves further exposition. Recall that $E = E(\varepsilon, \Delta_0)$ (Equation 2.4). It is clear that for a given E, the maximum value of Δ_0 is E, when $\varepsilon=0$. This implies that the minimum value of λ for a given E is

$$\lambda_{\min} = \ln(\frac{\hbar \omega_0}{E}). \quad (2.10)$$

Since $\Delta_0/\hbar$ is the tunneling rate for the system, we should ignore those states that relax only after times longer than the measurement's duration when calculating the specific heat. This implies that there is also a physical cutoff for a maximum λ. We can consider the probability density of states as a function of ε and λ for a fixed E (Figure 2.2).
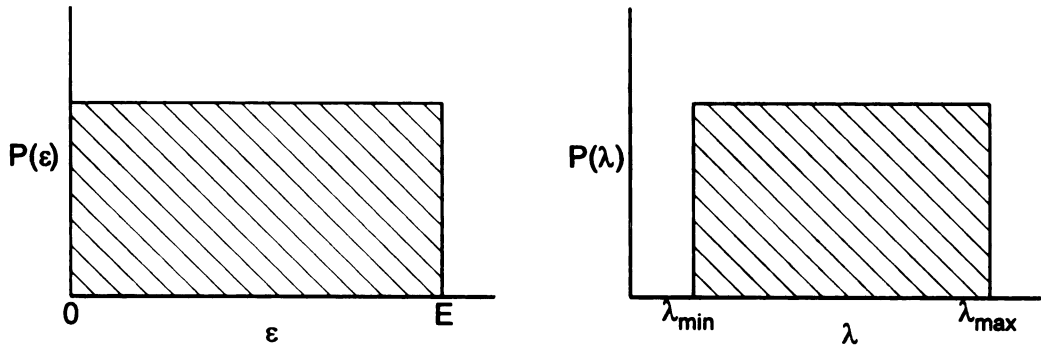
Figure 2.2 - Probability Density of TLS as a Function of the Parameters ε and λ.

From Equation 2.4 we see that for a given E, ε can vary from 0 to E. The Tunneling Model assumes that $P(\varepsilon)$ for the distribution of TLS is constant. We have seen that there are minimum and maximum values of λ allowed, and $P(\lambda)$ is assumed constant within

those bounds. As we increase E, we add more states proportionally to E due to the increase in the maximum value of ε. This produces the specific heat's linear temperature dependence we saw above. The fact that λ_{min} decreases logarithmically as energy increases implies that the specific heat should increase faster than that by a logarithmic term. This "superlinear" specific heat more closely describes the observations [Stephens].

A TLS interacts with its surroundings via distortions in its local environment produced by phonons. The dominant effect of strain on the TLS potential is through first order changes in asymmetry, ε, induced by long-wavelength strain fields [Phillips, 1981] [Halperin]. The interaction with the phonon bath takes the form

$$H_1 = \frac{1}{2}\begin{pmatrix} \delta\varepsilon & 0 \\ 0 & -\delta\varepsilon \end{pmatrix} = (\gamma)(\delta\sigma)\sigma_z . \tag{2.11}$$

$$\gamma \equiv \frac{1}{2}\frac{\partial\varepsilon}{\partial\sigma} \tag{2.12}$$

is the deformation potential for ε, and σ represents dimensionless strain. For simplicity, the tensor nature of γ has been suppressed. The relaxation rate for a single TLS can be calculated from this interaction using Fermi's Golden Rule [Jäckle]:

$$\tau^{-1} = \left(\frac{1}{v_l^5} + \frac{2}{v_t^5}\right)\frac{\gamma^2\Delta_0^2 E}{2\pi\rho\hbar^4}\coth\left(\frac{\beta E}{2}\right), \tag{2.13}$$

where v_x is the sound velocity for longitudinal or transverse phonon modes, ρ is the density of the solid, and β is the inverse temperature.

Now we can discuss the probability distribution for TLS as a function of energy and relaxation time. Jäckle gives

$$P(E,\tau^{-1}) = \frac{\overline{P}}{2} \frac{1}{\tau^{-1}(1-\tau^{-1}/\tau_m^{-1}(E))^{1/2}}, \qquad (2.14)$$

where $\overline{P}$ is the (constant) $P(\varepsilon, \lambda)$, and $\tau_m(E) = \tau(E, \Delta_0 = E)$ is the minimum relaxation

time for a given energy E, which corresponds to $\varepsilon = 0$. These symmetric states are the

ones most strongly coupled to phonons. The derivation of this probability density is

straightforward, since the infinitesimal element of probability must be the same

regardless of the choice of variables. $P(E,\tau^{-1})dEd\tau^{-1} = P(\varepsilon,\lambda)d\varepsilon d\lambda$, so

$P(E,\tau^{-1}) = \overline{P}J(\varepsilon,\lambda,E,\tau^{-1})$, where J is the Jacobian, the determinant of the matrix of

partial derivatives: $J(\varepsilon,\lambda,E,\tau^{-1}) = \det \begin{pmatrix} \dfrac{\partial\varepsilon}{\partial E} & \dfrac{\partial\lambda}{\partial E} \\ \dfrac{\partial\varepsilon}{\partial\tau^{-1}} & \dfrac{\partial\lambda}{\partial\tau^{-1}} \end{pmatrix}$. The remarkable feature of this

distribution in Equation 2.14 (see Figure 2.3) is the increase in the number of states at

very long relaxation times. This leads to a logarithmic increase in specific heat as a

function of time. Changing the measurement time from 1 microsecond to 1 second

increases the observed specific heat by a factor of three (Jäckle). This is an important

prediction of the Tunneling Model assumptions that has been experimentally confirmed

[Meißner and Spitzmann] [Loponen et al.].
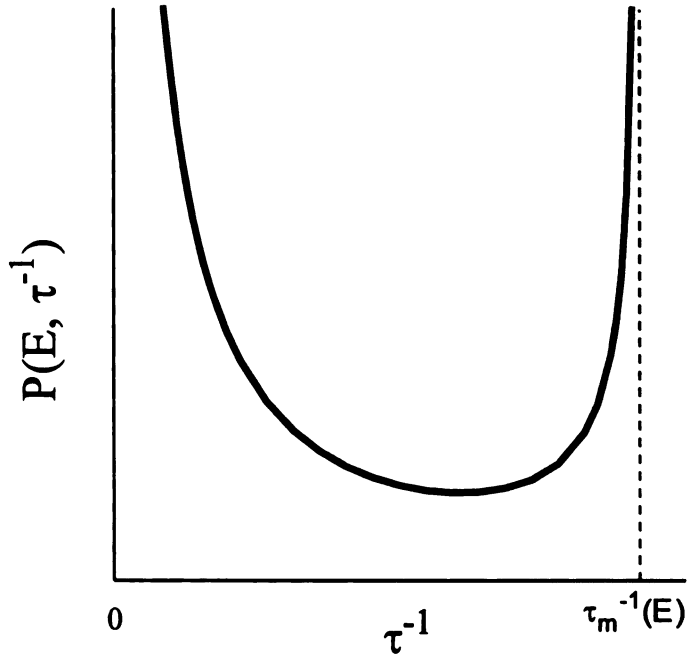
Figure 2.3 Probability Density of TLS as a Function of Relaxation Rate at Fixed Energy
The divergence of P as τ^{-1} approaches 0 gives rise to a time-dependent increase in the
TLS specific heat contribution

Another consequence of this broad distribution of tunneling levels can be seen in

the temperature dependence of the low-temperature thermal conductivity of amorphous

insulators. Observations suggested that the thermal conductivity varied as nearly T^2 [Pohl

and Salinger]. We will now show that the tunneling model predicts this. The phonon

mean free path through the TLS scatterers is given by [Phillips, 1972], [Black]

$$l_\alpha^{-1} = \left(\frac{\pi\omega}{\rho v_\alpha^3}\right) \overline{P}\gamma_\alpha^2 \tanh\left(\frac{\hbar\omega}{2k_BT}\right),\qquad(2.15)$$

where α is for transverse or longitudinal modes. Here ρ is the (mass) density, γ_α is the

appropriate TLS deformation potential, and v_α the mode's sound velocity. Starting from

Kinetic Theory, we can express the thermal conductivity through the bath of phonons as

$$\kappa = \frac{1}{3}C_{phonon}vl\,.\qquad(2.16)$$

12

For these TLS, summing over one longitudinal and two transverse phonon modes [Golding, Graebner, and Kane], one finds that

$$\kappa(T) = \frac{1}{3} k_B \sum_\alpha \int_0^\infty d\omega \left[\left(\frac{\beta \hbar \omega}{2} \right)^2 \mathrm{csch}^2 \left(\frac{\beta \hbar \omega}{2} \right) \left(\frac{\omega^2}{2\pi^2 v_\alpha^3} \right) \right] v_\alpha \left[\frac{\pi \omega}{\rho v_\alpha^3} \overline{P} \gamma_\alpha^2 \tanh \frac{\beta \hbar \omega}{2} \right]^{-1} . \quad (2.17)$$

$\beta = (kT)^{-1}$ and the bracketed terms represent C_{phonon} and l, respectively. After integration, we have

$$\kappa(T) = \frac{\rho k_B^3}{6\pi \hbar^2} \left(\sum_\alpha \frac{v_\alpha}{\overline{P} \gamma_\alpha^2} \right) T^2 \quad (2.18)$$

Experimentally, $\kappa(T)$ varies as T^α, where $\alpha \approx 1.8$-2.0 for many amorphous insulators [Stephens].

III. Acoustic Properties

Many low-temperature acoustic phenomena in amorphous insulators result from the coupling of TLS to phonons. Ultrasonic attenuation, velocity of sound shift, and, most strikingly, phonon echoes provide evidence of the presence of these excitations.

TLS-phonon scattering is a source of ultrasonic absorption in amorphous solids. These excitations couple to phonons through the deformation potential, which shows how spatial distortions in the lattice affect the energy of the two-level systems. We can estimate the acoustic power input at which saturation effects become apparent following Jäckle [Jäckle]. The absorption rate of phonon mode $\mathbf{k},\alpha$ is given by

$$\tau_{\mathbf{k},\alpha}^{-1} = \frac{\pi \overline{P} \gamma^2 \omega}{\rho v_\alpha^2} \tanh \left(\frac{\beta \hbar \omega}{2} \right) \equiv \tilde{\tau}_{\mathbf{k},\alpha}^{-1} \tanh \left(\frac{\beta \hbar \omega}{2} \right) \quad (2.19)$$

where $\omega = v_\alpha k$ and $\beta^{-1} = kT$. $\tau_{\mathbf{k},\alpha}^{-1}$ depends on temperature through the population factor

$$\tanh \left(\frac{\beta E}{2} \right) = 1 - 2n_0(E), \quad n_0(E) = \frac{1}{e^{\beta E} + 1} . \quad n_0 \text{ is the distribution function for the TLS in}$$

thermal equilibrium. Note that resonant absorption decreases with increasing temperature as the population difference decreases. We should therefore see the resonant absorption saturate at sufficient input power levels. Starting from the phonon emission rate, we can find the saturation absorption, since, in the stationary saturated case, these two are equal. The recombination rate of the TLS j is

$$-\dot{n}_j = \frac{n_j(1 + N_0(E_j)) - (1 - n_j)N_0(E_j)}{\tilde{\tau}_j},$$ (2.20)

where $N_0(E) = \dfrac{1}{e^{\beta E} - 1}$. The left side of the numerator is the contribution from spontaneous phonon emission, the right is that from stimulated absorption, and $\tilde{\tau}_j$ is the temperature-independent part of the TLS relaxation time (Equation 2.19). The maximum for this rate occurs at $n_j = \frac{1}{2}$, so the stationary (maximum) absorption is given by

$$\dot{Q}_s = \hbar\omega \sum_{j,|E_j - \hbar\omega| < \Gamma} \dot{n}_j^{(s)} = \frac{\hbar\omega}{2} \sum_{j,|E_j - \hbar\omega| < \Gamma} \tilde{\tau}_j^{-1}.$$ (2.21)

The sum is over all states within Γ (the level width) of the incident frequency. We can also incorporate (experimental) phonon frequency uncertainty in Γ. We can evaluate this sum with Equation 2.14:

$$\dot{Q}_s = \frac{\hbar\omega}{2} 2\Gamma \int_0^\infty d(\tau^{-1}) \tilde{\tau}^{-1} P(\hbar\omega, \tau^{-1}).$$ (2.22)

This becomes

$$\dot{Q}_s = \left(\frac{1}{v_l^5} + \frac{2}{v_t^5}\right) \frac{\overline{P}\gamma^2 \Gamma \omega^4}{2\pi\rho}.$$ (2.23)

Now we can estimate the input power at which saturation effects become important by setting the linear absorption equal to this maximum rate. The linear absorption rate is j_i/l,

where j_i is the incident power and l is the phonon mean free path (Equation 2.15). The saturation value of input power, j_i^s, becomes

$$j_i^s = \dot{Q}_s l = \left(\frac{1}{v_l^5} + \frac{2}{v_t^5} \right) \frac{\Gamma c_a^3 \omega^3}{2\pi^2} \coth\left(\frac{\beta \hbar \omega}{2} \right). \tag{2.24}$$

Jäckle evaluated this for fused silica at 1K and found that for a 1 GHz incident frequency, the saturation incident power is of the order of 10^{-8} W/cm^2. This small power level made experimental confirmation of resonant saturation absorption difficult, but not impossible [Hunklinger et al., 1972] [Golding et al., 1973].

The most striking acoustic property due to TLS may be phonon echoes [Golding and Graebner]. At temperatures below about 100 mK, the relaxation time of a TLS (Equation 2.13) can be longer than the duration of a typical ultrasonic pulse of 100 nS. This implies that coherent effects can be observed. Above (Equation 2.2), we saw that the problem of a two-level system can be expressed in terms of that of a spin system. Specifically, we can write the Hamiltonian as

$$H = H_0 + H_1 = \frac{1}{2} E\sigma_z - \left(M\sigma_x + \frac{1}{2} D\sigma_z \right) e \tag{2.25}$$

where $M = \dfrac{\gamma \Delta_0}{E}$ and $D = \dfrac{2\gamma \varepsilon}{E}$. This shows formal correspondence between the TLS and a spin-1/2 object in a magnetic field. We can therefore define a pseudopolarization vector, **P**, and discuss the effects of external fields in terms of the expectation value of this operator. The x and y components of **P** are related to the components of stress in phase and out of phase with the applied strain field, analogous to the transverse components of spin in the magnetic case. Components of <P> must satisfy the coupled

Bloch and wave equations, analogous to the case of light traveling through a resonantly absorbing medium [Allen and Eberly].

Upon application of a strain $e = e_0 \cos(\omega t - kz)$, we find that the nutation frequency in the usual rotating coordinate frame is given by $\omega_1 = \dfrac{M e_0}{\hbar}$. The maximum echo amplitude occurs with a sequence of pulses of 'areas' $\pi/2$ and π. The $\pi/2$ pulse rotates polarizations initially along the z-axis (for those TLS that are resonant with the pulse frequency) into the x-y plane. The spread in frequencies of the excited states causes rapid dephasing of those rotated polarization vectors. The second pulse rotates the polarizations by π radians, and now they tend to become phase-coherent again, doing so after a length of time that is equal to the separation between the two pulses. Once the polarizations become coherent again, a spontaneous echo is produced. Note that the time between pulses must be shorter than the relaxation time for the TLS in order to observe echoes. In the simple case of the symmetric TLS problem, $E = \Delta_0$ and $M = \gamma$ (see Equation 2.4). The pulse area for a rectangular pulse of duration τ is given by

$$\theta = \int_{-\infty}^{+\infty} \omega \, dt = \frac{\gamma e_0}{\hbar} \tau . \tag{2.26}$$

Since the symmetric TLS scatter most strongly, we can use Equation 2.26 to determine γ, the deformation potential. Experiments measured deformation potentials for Suprasil-W of 1.5 eV, consistent with earlier expectations [Phillips, 1972] [Anderson et al., 1972] [Jäckle] and values inferred from other experiments [Zaitlin and Anderson] [Berret and Meißner]. Other experimental determinations of γ actually measure the product $\bar{P}\gamma^2$

(see Equations 2.15, 2.18 for example) and so "consistency" is a more accurate description of the situation than "agreement".

IV.   TLS in Metals

The behavior of tunneling, two-level systems is quite different in amorphous metals. Electron-hole excitations can interact strongly with tunneling lattice defects that we can describe as TLS. The theory of Dissipative Quantum Tunneling describes the dynamics of a two-level system in contact with a thermal bath of excitations [Kondo] [Leggett et al.]. Interaction with conduction electrons can change even the qualitative behavior of the TLS dynamics, as we shall see.

The Hamiltonian for an isolated TLS was given above as Equation 2.2. We have already discussed the effects of interaction between that system and phonons through the strain dependence of the TLS potential. We will now model the interaction of the TLS with conduction electrons and its effects on the tunneling parameters and dynamics. This interaction renormalizes the effective tunneling parameters, removes the coherence of the tunneling process (when $\Delta_0 \ll kT$), and can alter the temperature dependence of the tunneling rates in a dramatic fashion, leading to an *increase* of tunneling rate with decreasing temperature [Leggett et al.] [Grabert and Weiss] [Fisher and Dorsey]. This inverse temperature dependence is a signature phenomenon of dissipative quantum tunneling.

In this treatment, we are concerned with a limited range of the full parameter space available to the problem. Our TLS model implies that we need to consider only configurations where the wavefunction overlap is much smaller than the ground state energy in a potential well: $\Delta_0 \ll \hbar\omega_0$. This is due in part to the nature of the experiments

in question. We resolve defects switching states in the time domain on the order of seconds, where the vibrational frequency in a well is on the order of 10^{12} s^{-1}[Cukier et al.]. Faster defects have been observed and give rise to anomalies in the I-V characteristic of ultrasmall samples [Ralph and Buhrman]. In addition, we require that kT<<V,$\hbar\omega_0$, resulting in a true two-level system in the tunneling regime. We have no *a priori* relation between the energy splitting, ϵ, and kT to consider. In fact, the relative magnitude of these two energies will play an important role in the dynamics of the TLS in the presence of dissipation. Finally, the TLS tunnels in an incoherent manner, due to the rapid dephasing effect of interactions with thermal electron-hole excitations. This implies that the well occupation states form the correct basis with which to consider the problem of a TLS in a metal, rather than the energy eigenstate basis that is appropriate in insulators.

There are three regimes into which we can divide the electron-hole excitations for consideration of their interaction with the TLS. Two of these, excitations with energy much larger or much smaller than $\hbar\Delta$, are excluded from the Hamiltonian by renormalization of the tunneling rate, which I will describe below. The third, intermediate group produces interactions that can be modeled with a bath of harmonic oscillators [Caldiera and Leggett]. What results is then a truncated spin-boson Hamiltonian:

$$H = \frac{\epsilon}{2}\sigma_z - \frac{\Delta_r}{2}\sigma_x + \sigma_z \sum_j G_j(b_j + b_j^\dagger) + \sum_j \hbar\omega_j b_j^\dagger b_j. \qquad (2.27)$$

Here the $b_j^\dagger$ and b_j are the creation and annihilation operators for the model harmonic oscillators, G_j are the interaction between the defect and the harmonic oscillator state j,

and Δ_r is the renormalized tunneling matrix element. This problem is tractable [Leggett et al.], and one finds that the thermal bath only affects the dynamics of the TLS through the spectral density of its excitations,

$$J(\omega) = \left(\frac{2}{\hbar^2}\right) \sum_j G_j^2 \delta(\omega - \omega_c).$$ (2.28)

For a metal, the form of $J(\omega) = \alpha\omega$ for $\omega < \omega_c$, which gives Ohmic dissipation [Chakravarty and Leggett]. The parameter α is very important; it determines the coupling of the TLS to the bath of interactions. In metals, α lies between 0 and ½ [Yamada et al.].

Let us return to the renormalization of the tunneling rate and provide some motivation. One can separate the high-energy excitations because above some cutoff frequency, ω_c, we expect the oscillators to be fast enough to follow the motion of the defect adiabatically [Kagan and Prokof'ev]. ω_c is naturally between the tunneling rate and oscillation frequency of the TLS well; $\Delta_0 \ll \omega_c < \omega_0$. This adiabatic interaction leads to a renormalization of the bare tunneling matrix element:

$$\Delta = \Delta_0 \left(\frac{\omega_c}{\omega_0}\right)^\alpha.$$ (2.29)

In addition, the oscillators with frequencies smaller than the tunneling rate of the TLS can have little effect on its dynamics, since their periods are longer than the average dwell time in any one well. This leads to a renormalization of Δ:

$$\Delta_r = \Delta \left(\frac{\Delta}{\omega_c}\right)^{\frac{\alpha}{1-\alpha}} = \Delta_0 \left(\frac{\Delta_0}{\omega_0}\right)^{\frac{\alpha}{1-\alpha}}.$$ (2.30)

Note that the final form of Δ_r does not depend on the choice of ω_c.

One can now calculate the relaxation rate of the TLS by considering the transition probability from the higher-energy to the lower-energy state, $P(t)=<\sigma_z(t)>$, given that $<\sigma_z(t\le0)>=1$. One finds that

$$P(t>0) = -\tanh\left(\frac{\varepsilon}{2kT}\right) + \left[1 + \tanh\left(\frac{\varepsilon}{2kT}\right)\right]e^{-\gamma} , \qquad (2.31)$$

where the total tunneling rate, γ, is given as

$$\gamma = \frac{\Delta_r}{2\hbar}\left(\frac{2\pi kT}{\Delta_r}\right)^{2\alpha-1} \frac{\cosh\left(\frac{\varepsilon}{2kT}\right)}{\Gamma(2\alpha)} \left|\Gamma\left(\alpha + i\frac{\varepsilon}{2kT}\right)\right|^2 . \qquad (2.32)$$

Note that $\Gamma(a + ib)$ is the complex gamma function, $\Gamma(z) = \int_0^\infty e^{-x} x^{z-1} dx$. The transition rates from the higher-energy state to the lower-energy state ($\gamma_{f(ast)}$) and vice-versa ($\gamma_{s(low)}$) must obey detailed balance. Therefore $\frac{\gamma_f}{\gamma_s} = e^{\frac{\varepsilon}{kT}}$, since the energy splitting between the two levels is the asymmetry, ε. The total tunneling rate is the sum of these rates, $\gamma = \gamma_f + \gamma_s$, giving

$$\gamma_f = \frac{\Delta_r}{4\hbar}\left(\frac{2\pi kT}{\Delta_r}\right)^{2\alpha-1} \frac{e^{\frac{\varepsilon}{2kT}}}{\Gamma(2\alpha)} \left|\Gamma\left(\alpha + i\frac{\varepsilon}{2kT}\right)\right|^2 \text{ and } \gamma_s = \gamma_f\, e^{-\frac{\varepsilon}{kT}} \qquad (2.33)$$

[Leggett et al.] [Grabert and Weiss] [Fisher and Dorsey].

For $0 < \alpha < \frac{1}{2}$, the behavior of these rates is quite different depending on the relative sizes of ε and kT. For $\varepsilon < kT$, the tunneling rates increase with decreasing temperature; $\gamma_f, \gamma_s \propto T^{2\alpha-1}$ [Kondo]. This is a signature feature of Dissipative Quantum Tunneling. It has been experimentally verified, first in studies of muon diffusion in

metals [Clawson et al.] [Kehr et al.] [Welter et al.]. When kT < ε, the rates depend on temperature following a simple model: decay (γ_f) can occur via stimulated or spontaneous emission, while γ_s is due to stimulated absorption. As the temperature decreases, the fast rate remains roughly constant, since the kT < ε relationship implies that the spontaneous emission process dominates relaxation. The slow rate decays as $e^{-\frac{\varepsilon}{kT}}$ as the thermal bath excitations decrease in number.

V.   Single Defect Studies

The coupling of two level systems to phonons in amorphous solids is through the effect of strain on the local, microscopic potential. We have seen that Equations 2.15 (phonon mean free path), 2.18 (thermal conductivity), and 2.26 (phonon echo pulse area) are examples of the influence of this strong coupling parameter, γ. All of these measurements sample large numbers of TLS parameters and therefore are affected by assumptions about the distributions of those parameters. Mesoscopic, metallic samples in the Quantum Transport (QT) regime (i.e., the quasiparticle de-phasing rate is less then the total scattering rate) offer a new opportunity. At low temperatures in small samples, electrical transport shows effects due to the interference of electrons as they travel through a field of scatterers [Lee and Ramakrishnan]. These interference effects can lead to a remarkable sensitivity of the electrical conductance on the location of these scatterers. Even the small change due to the motion of an individual TLS can produce a measurable effect on the conductance [Al'tshuler and Spivak] [Feng et al.].

In 1991, the first observation was made of an individual TLS in a mesoscopic metal [Zimmerman et al]. Subsequently, the detailed form of the tunneling rates

(Equation 2.33) was confirmed, establishing the validity of the Dissipative Quantum Tunneling behavior of TLS in metals [Golding et al., 1992] [Chun and Birge, 1993].

This approach provides our best opportunity to uncover information about the nature of the TLS that pervade disordered systems. We can now observe a single defect incoherently tunneling between two states. By applying perturbations that affect the dynamics of a TLS, we can learn details about its microscopic potential.

Chapter 3

Quantum Transport

I.   Introduction

Electrical conduction in bulk metals at temperatures above a few K is accurately

described by the ideas of semi-classical, Boltzmann transport. Quasiparticles, which are

excitations of the filled Fermi sea of electrons, travel through the periodic potential of the

lattice under the influence of externally applied electrical fields. In the weakly-

disordered limit, they move diffusively, scattering from lattice imperfections and each

other [Lee and Ramakrishnan]. These imperfections include the thermally-induced

motion of lattice ions (phonons), structural defects, and impurities. We begin by

assuming that the scattering events are inelastic, isotropic, and random events, and that

the probability of a collision occurring in a time dt is dP = dt/τ, where τ is the average

time between scattering events. We then find that the conductance in this model is given

by the familiar Drude formula,

$$\sigma = \frac{ne^2\tau}{m}.$$ (3.1)

An interesting question is how this picture changes when we increase the disorder

present in the lattice. For the semi-classical, diffusive quasiparticle description to hold,

we require that $k_F l \gg 1$; that is, the elastic mean free path must be much longer than the

quasiparticle Fermi wavelength. Otherwise, the random-walk picture of diffusion breaks

down, since we can no longer consider the scatterers as independent point-scatterers. The

goal of this chapter will be an explanation of some phenomena specific to disordered metals. In particular, we will explore how elastic scattering with a rate larger than the inelastic rate alters this simple picture.

Quasiparticle scattering in pure metals at temperatures above a few degrees K is dominated by interaction with phonons. This can be seen in the resistance versus temperature of metals from 10 K to room temperature [Ziman]. Electron-phonon scattering events are inelastic; in fact they represent the mechanism by which the quasiparticle system comes to thermal equilibrium with the lattice. At low temperatures, phonons become rare and other scattering mechanisms become more important to conduction. Eventually the impurity scattering rate becomes larger than the phonon rate, leading to a low-temperature residual resistivity common for metals [Ziman]. Then, a quasiparticle can travel through many elastic collisions before its energy has changed. Elastic scattering does not destroy the phase coherence of the quasiparticles, and so we must consider interference effects to determine the trajectory of the particle. As the quasiparticle coherence length increases, conduction processes change character from classical diffusion mechanisms (if phase is always randomized at every collision) to transmission of incident wavefunctions through a disordered medium [Landauer]. Phase-coherence effects on conduction are described by the theories of Quantum Transport (QT).

One of the foundations upon which quantum transport theory is built is the early work of Anderson [Anderson]. He considered the effects of disorder on a conductor by trying to reason what the form of a single electron state in a random potential would be. He concluded that a sufficiently disordered potential should produce localized states,

rather than extended, conducting ones. To lowest order, the electrons would be bound in random potential wells, and the degree of mixture of these locally bound states would determine whether the states would be ultimately localized or extended, as the sample size was extended to infinity. The case of a crystalline lattice, in which neighboring wells are identical to each other, is a very special case. There, the degeneracy of states and their proximity induce large overlaps that produce extended Bloch states in metallic crystal lattices. Anderson argued that in a random potential, the states in neighboring wells have no special relationship in energy, thereby lowering their overlap integrals. Degenerate states of course still exist, but they would in general be far removed spatially, decreasing the amount of admixture exponentially with separation. If sufficient disorder exists in the potential, single electron states will be localized and decay exponentially beyond a localization length. Samples larger than this localization length would be insulating, and this describes the metal-insulator transition as a function of sample size. We can also consider this transition as a function of Fermi energy, for moderately disordered samples. The critical energy above which states become extended represents the mobility edge [Mott], since extended states give rise to nonzero conductance at zero temperature.

Several years later, Thouless introduced the foundations for the scaling theory of localization, based on Anderson's work [for review, see Thouless, 1974]. Thouless started by considering the assembly of a $(2L)^d$ hypercube of material by placing L^d samples together. He questioned whether the eigenstates of the larger system could be easily related to those of the smaller system. States in the $(2L)^d$ sample are linear combinations of those in the $(L)^d$ system, and the degree of mixing is determined by the

overlap of the wavefunctions and their energy differences. The level spacing in the smaller region sets the scale of the perturbation theory energy denominator, $\delta W = (N_0 L^d)^{-1}$, where N_0 is the density of states. The overlap of wavefunctions is identified as δE. Thouless estimated δE by observing that if periodic boundary conditions are applied to the L^d region, its eigenstates will broaden into bands. He surmised that the bandwidth would be a good estimate of the wavefunctions' overlaps. Consider again the transition from L^d to $(2L)^d$: if states remain localized, then the overlap integrals must be exponentially small, and therefore $\delta E / \delta W$ is small. If $\delta E / \delta W$ is large, then the (L^d) states will be extended through the $(2L)^d$ region. Thouless observed that the parameter $\delta E / \delta W$ determines the degree of localization of the electron states in the (L^d) sub-regions. In fact, the zero-temperature conductance of the sample is directly related to $\delta E / \delta W$ [Anderson and Lee].

Thouless later argued that at non-zero temperature, inelastic scattering randomizes the phase of electronic states and therefore destroys the interference that causes the localization due to phase coherence [Thouless, 1977]. If the elastic scattering rate is faster than the inelastic rate, then we define a diffusive phase-breaking length:

$$L_\phi = \sqrt{D\tau_\phi} \qquad (3.2),$$

where $D = (v_f^2 \tau / d)$ is the diffusion constant, and v_f is the Fermi velocity, τ is the elastic scattering time, and d is the dimensionality. L_ϕ is the average distance that an electron will diffuse before being de-phased by an inelastic scattering event. L_ϕ determines the length scale over which the effects of electron quantum interference can persist. At low temperatures, L_ϕ can commonly extend over a micron in length in readily fabricated

samples. This has allowed broad experimentation in mesoscopic physics, where samples
are fabricated that have dimensions less than the phase-breaking length.

Another important conceptual advance was made when a connection was
discovered between conductance and quantum interference effects in 1-dimensional
metallic samples [Landauer]. In particular, he found a relationship between the
conductance of a metallic region with scatterers and the transmission matrix for incident
flux from one side of that region to the other. Conduction in coherent samples becomes a
scattering problem and can be calculated via the transmission of states in one perfect,
infinite lead to that on the other side of the disordered region. The Landauer equation
states that

$$G = \frac{2e^2}{h} \text{Tr}(tt^+), \qquad (3.3)$$

where t is the transmission matrix across the disordered region. Conduction occurs
through quasiparticle 'channels', representing the quantization of transverse momentum
states in the disordered region. The total number of channels is k_F^2 times the cross-
sectional area of the region, and each channel has a maximum possible conductance of
e^2/h. $\text{Tr}(tt^+)$ is often identified as the number of effective conduction channels. The
factor of two comes from the spin-degeneracy of the quasiparticles. Note that we are
discussing the diffusive regime, and here $\text{Tr}(tt^+)$ is much less than the total number of
channels in the sample. The Landauer equation has also been generalized to higher
dimensions and multi-probe measurement geometries [Büttiker] [Stone and Szafer]. The
multi-dimensional form of the Landauer equation shares with Equation 3.3 the essential
feature that the conductance of the sample is a function of its transmission properties,
when it is considered as a scattering region for coherent incident electron flux. The

Landauer idea has helped the understanding of some of the physical phenomena attributed to quantum transport effects.

II.   Weak Localization

I will now review some phenomena that result from quantum mechanical corrections to the conductance of disordered metals at low temperature. First, I will describe the physical picture that leads to the quantum transport phenomenon known as Weak Localization (WL). WL corrections to the resistance of metals and 2-d electron inversion layers are observed as low temperature resistance anomalies [Dolan and Osheroff] [Kobayashi et al.] [Van den dries et al.] that feature a strong dependence on applied magnetic field [Bergmann, 1979]. The observations [Bergmann, 1984] have been very well described by an application of quantum transport theory [for a review, see Al'tshuler et al., 1987].

Imagine that the sample is a region of crystalline metal at low temperature with some localized scatterers. These could be lattice dislocations, vacancies, impurities, etc. We want to describe the motion of the quasiparticles, which are the excitations of the electronic system without the disorder present. These quasiparticles move by diffusing from one scatterer to another, traveling undisturbed between scattering events. If the elastic scattering rate is higher than the inelastic scattering rate, then we must consider the possibility that the various possible paths that a quasiparticle could traverse can interfere. To determine the particle trajectories, the wavefunction amplitudes must be added.

Suppose for simplicity that we can construct a film with thickness $t < L_\varphi$, making the sample quasi-2D. This geometry is not required to observe WL effects, but it is

useful for making the usual magnetoconductance measurements described below. Now we must consider interference effects when describing electrical transport through any region of size roughly L_φ^2 in the sample. Consider the special subset of quasiparticle Feynman paths that contain closed loops.
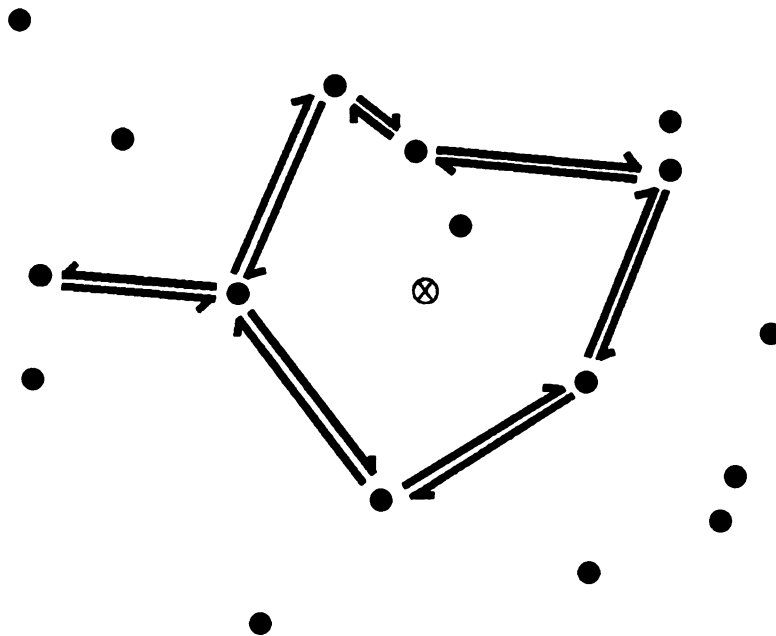
Figure 3.1 Quasiparticle Trajectories in a Small Part of a Weakly Disordered Conductor. The paths only differ in the direction of traversal of the closed loop. Lateral dimensions of the region shown are smaller than the phase-breaking length. The average distance between scattering centers is the mean free path, *l*.

In Figure 3.1, we see a schematic representation of a weakly disordered region of a conductor, with scattering centers represented by the filled circles. Two possible quasiparticle trajectories are drawn that differ only by the direction of traversal of the closed loop portion of the path. A quasiparticle can traverse such a loop either clockwise or counterclockwise. These two traversals have exactly the same accumulated phase at

29

the end of the trip around the loop, as long as their energy remains constant. Thus, the wavefunctions add constructively at the return vertex. (This constructive interference persists regardless of the impurity configuration. Hence, WL survives impurity averaging.) The net result of this constructive interference is to increase the probability that any quasiparticle will return to its origin during its diffusive motion, leading to a decrease in conductance:

$$\Delta G_{square} = -\frac{e^2}{\pi\hbar}\ln(\frac{3L_\varphi^2}{l^2}) \quad \text{(quasi-2D result)}. \tag{3.4}$$

As inelastic scattering becomes more rare, τ_φ and therefore L_φ increase, leading to a decrease in conductance as sample temperature is lowered.

The detailed temperature dependence of τ_φ depends on the dominant quasiparticle de-phasing mechanism. Above a few K, this appears to be electron-phonon scattering and below that low-energy-transfer electron-electron scattering [Bergmann, 1984]. Electron-electron interaction in a disordered metal also decreases the conductivity as temperature is lowered [Al'tshuler et al., 1987] [Lee and Ramakrishnan], but WL has a definitive magnetic field dependence that sets its contribution apart. Since the interfering quasiparticle paths traverse closed loops in opposite directions, introduction of a perturbation that breaks the time-reversal symmetry of that process destroys this constructive interference. Magnetic flux threading the loop introduces a relative phase shift between the paths of

$$\Delta\phi = \frac{2e}{h}\oint \mathbf{A} \cdot \mathbf{dl} \tag{3.5}$$

via the Aharonov-Bohm effect. This flux is depicted as the circled 'X' in Figure 3.1. If the applied field is perpendicular to our 2-D example, then this phase shift is roughly $e/\hbar$

30

$(B * L_\varphi^2)$. When this phase shift is of order $\pi/2$, then the interference at the paths' crossing-point is no longer constructive.

In precisely the same way, the conductance of a metallic cylinder or ring with diameter smaller that L_φ features oscillations in conductance as a function of magnetic field along its axis [Sharvin and Sharvin]. Paths that traverse the circumference in opposite directions get a relative phase shift from the Aharonov-Bohm effect, implying that the conductance is periodic in applied magnetic flux, with the period of $\phi = h/2e$. The 2 in the denominator is due to the fact that the area is enclosed twice by the interfering partial waves. Rings exhibit oscillations with period h/e as well [Webb et al.], but their physical origins are different (they are due to a different interference process, closely related to Universal Conductance Fluctuations and described below). The h/e oscillations are sample-specific and therefore ensemble-average to zero in structures such as long tubes or arrays of rings.

In a metal film at a few K, L_φ is on the order of $1\mu m$, implying that fields less that 100 Gauss would begin to affect the conductance. As the strength of the field is increased, the constructive interference in smaller and smaller loops is quenched, leading to the following expression for the magnetoconductance due to WL of a quasi-2D conductor:

$$\Delta\sigma(\omega = 0, B) = -\frac{e^2}{2\pi^2 h}\left[\psi\left(\frac{1}{2} + \frac{B_1}{B}\right) + \frac{1}{2}\psi\left(\frac{1}{2} + \frac{B_2}{B}\right) - \frac{3}{2}\psi\left(\frac{1}{2} + \frac{B_3}{B}\right)\right],$$

where

$$B_1 = B_O + B_{SO}$$
$$B_2 = B_\varphi$$
$$B_3 = \frac{4}{3}B_{SO} + B_\varphi$$

and ψ is the digamma function.

Note that $B_0\tau_0 = \frac{3\hbar}{4eD}$, and for B_φ and B_{SO},

$$B_x\tau_x = \frac{\hbar}{4eD}$$

$$D\tau_x = L_x^2,$$

$\qquad\qquad(3.6)$

where D is the diffusion constant.

B_0 is due to elastic scattering, while B_{so} and B_φ are from spin-orbit and inelastic scattering, respectively. This quantum transport correction to the conductance is calculated by using the Kubo formalism and evaluating the appropriate diagrams with impurity-averaged perturbation theory. The above results are based on the work of several groups [Al'tshuler et al., 1980] [Maekawa and Fukuyama] [Hikami et al]. The expression is valid when there is no appreciable magnetic impurity (spin-flip) scattering, which would be a further source of dephasing [Bergmann, 1984].

Notably, strong spin-orbit (SO) scattering changes the sign of the interference in zero field, giving an impurity-averaged correction (when $\tau_{so}^{-1} >> \tau_\varphi^{-1}$) of $-1/2$ of the previous WL correction to the conductance (Equation 3.4). In a system with strong spin-

orbit scattering, the resistance anomaly becomes an increase in conductance proportional to ln(T) [Bergmann, Phys. Rev. Lett., 1982] [Bergmann, Solid State Comm., 1982]. When the spin-orbit scattering rate is higher than the dephasing rate, the SO scattering effectively rotates the spin of the quasiparticles without destroying the coherence between a path and its time-reverse. The direction of rotation is opposite for the two paths, however. When the relative rotation is 2π, one spin wavefunction picks up a factor of -1 relative to the other, and so the partial waves interfere destructively.

III.   Universal Conductance Fluctuations

III A.   Introduction

Starting in 1984, observations of the low-temperature conductance of small metallic wires revealed fluctuations as a function of magnetic field [Umbach et al., 1984] [See Figure 5.1b for an example of G vs B]. These fluctuations are random, reproducible changes in conductance versus field that are in detail unique to a particular sample. G(B) vs. B has therefore been called the magnetofingerprint. The average magnitude of the fluctuations for any sufficiently small sample (i.e., smaller than L_φ) is seen to have the universal amplitude of e^2/h, regardless of the size of the conductance in zero field. This led to the naming of the phenomenon as Universal Conductance Fluctuations (UCF). Small metallic rings also exhibit UCF in addition to the Aharonov-Bohm oscillations due to the magnetic flux through the rings [Webb et al] [Washburn et al.] [Chandrasekhar et al.] [Umbach et al., 1986]. The UCF were also observed in semiconductors, and there the fluctuations exist in conductance as a function of chemical potential as well as magnetic field, with similar amplitude [Skocpol et al] [Licini et al.].

The UCF in a given sample were seen to increase in amplitude as the temperature was lowered until they reached the universal amplitude of e^2/h. This indicated that a possible mechanism to explain the insensitivity to sample size was that a temperature-dependent length scale increased until it exceeded the dimensions of the sample, at which point the scale of the phenomenon would be set by the sample size. It was known that quantum interference effects generate length scales that increase as temperature is lowered (L_φ, e.g.) and this provided impetus to theoretical investigations in quantum transport as a source of UCF. In addition, interference effects could explain the sample-specific nature of the detailed behavior of conductance versus field or chemical potential, since they depend on the microscopic details of the region's impurity potential.

UCF theoretical studies began by considering the possible statistical fluctuations in conductance between members of an ensemble of disordered metallic regions that differ only in their microscopic impurity potentials. An ergodic hypothesis was formulated to connect these statistical deviations with the sample-specific observations of conductance versus field or chemical potential [Lee and Stone] [Al'tshuler and Khmel'nitskii]. This was essential in comparing the statistical theoretical results to experiments, where only a limited number of samples could be measured. The basic tenet of this hypothesis is that once the applied magnetic field or chemical potential has been changed by an amount large enough to significantly alter the quasiparticle interference pattern in the sample, the new conductance should be no more related to the old one than it is to any other member of its ensemble of possible impurity configurations.
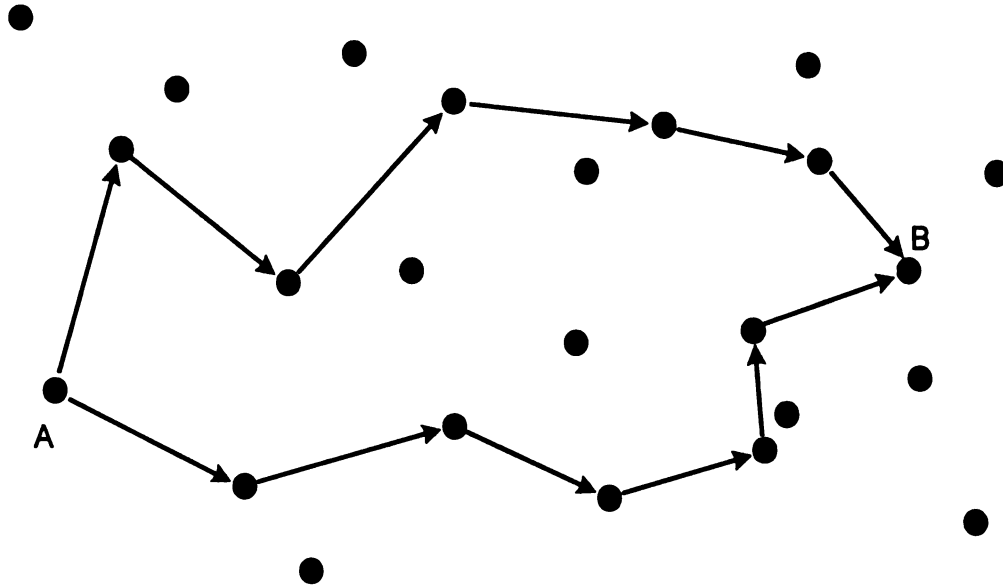
Fig 3.2 A Region of a Disordered Conductor in the UCF Regime. Two possible diffusive quasiparticle paths are illustrated from point A to point B. Filled circles represent scattering centers. The region shown is smaller than the phase-breaking length, L_φ.

In Figure 3.2, we see a section of a UCF sample, where two possible quasiparticle paths are highlighted from points A to B. The average spacing of scatterers represents the elastic mean free path, which is much smaller than the phase-breaking length. The total conductance from A to B is derived from adding the amplitudes for all possible (Feynman) paths between the two points, as long as $k_F l \gg 1$. By adding magnetic flux, this interference pattern is changed in a random way due to the particular relative locations of the scatterers. Each path gets a unique relative Aharonov-Bohm phase shift due to the applied flux, and the conductance changes. This is the physical mechanism behind the variation of the conductance with magnetic field. This interference mechanism makes clear why the observed fluctuations are random and sample-specific. The finite size of the interfering region sets the scale of the correlation field, similar to

the WL phenomenon. If the center of the region were hollow, this diagram would represent the case of a ring structure rather than a film. Such mesoscopic rings (diameter $\leq L_\varphi$) also exhibit h/e periodicity with applied magnetic flux, due to the periodic phase shifts induced between paths along the top and bottom portions of the ring. Random phase shifts within each arm of the ring still provide aperiodic changes in conductance.

We must add other considerations to this simple picture to explain the universal amplitude of the fluctuations, however. I will describe in the following sections three approaches to understanding UCF. The first is an heuristic physical argument that will show that the UCF arise quite naturally from correlations between energy levels in a disordered region. In the next section, I will discuss more rigorously the unusual statistics observed among the eigenvalues of the transmission matrices of disordered conductors. Here, we will find an origin for the correlations between transmission eignestates and also some predictions for UCF relative amplitudes as a function of the symmetry of the transmission matrix. By applying external perturbations to a given sample to change that symmetry, experiments can verify the predictions of the Random Matrix Theory description of UCF. The third UCF section describes a perturbation theory calculation for UCF. By using diagrammatic techniques to calculate the ensemble average conductance and conductance correlation functions for Fermi energy and magnetic field, the greatest number of details about UCF measurements are described. UCF amplitude as a function of sample size, sample dimensionality, and temperature are revealed. Also, the correlation magnetic field and Fermi energy can be derived. These correlation fields set the scale for applied perturbations that alter the conductance of the

sample and allow a theoretical connection between experimental fingerprint data and ensemble average quantities.

III B. Thouless Argument

Recall the Landauer idea that conduction occurs through quasiparticle channels that cross the sample. These effective channels are extended states that couple lead states from one side of the region to the other. Since electrons spend a finite time diffusing across the sample, there is an associated energy uncertainty that broadens the energy level of the electron while it is in the sample. This uncertainty is $\hbar/\tau_D$, where τ_D is the time to diffuse across the sample: $\tau_D = (L_x^2/D)$, where L_x is the sample length. This energy uncertainty has been called the Thouless energy,

$$E_c = \hbar/(\min \{\tau_D, \tau_\varphi\}) \qquad (3.7)$$

E_c is either set by the sample length or L_φ, whichever is shorter. (Recall that τ_φ is the maximum time for which a quasiparticle can travel and remain coherent, and the levels are broadened only by the coherent time spent within them.) In this picture of conduction, the sample conductance is set by the number of channels with energy within E_c of the chemical potential of the measuring lead. The number of effective conduction channels is then given by $E_c/\delta E$, where δE is the average level spacing. Equation 3.3 reduces to

$$G = \frac{2e^2}{h} \cdot \frac{E_c}{\delta E}. \qquad (3.8)$$

The expected fluctuation of the conductance when chemical potential or impurity configuration is varied would be $2e^2/h$ times the change in the number of effective channels in the broadened energy scale. If the energy levels obeyed Poisson statistics, the

expected fluctuation would be $N_{channels}^{1/2}$. Even in a mesoscopic sample, the number of

effective channels is typically very large; a 100 Ohm sample has hundreds of effective

conduction channels. Observations show that in sufficiently small samples (i.e., $L_x < L_\varphi$),

the observed change in number of effective channels is always of order 1. This indicates

that some other statistical ensemble must describe the spectrum of energy eigenvalues in

the sample.

It should be pointed out, however, that we have assumed that the entire sample is

phase-coherent. For larger samples, we effectively have several independently

fluctuating regions. The relative size of fluctuations then decreases normally as the

square root of the number of independent regions.

III C.   Transmission Matrix Eigenvalue Statistics

Consider the origin of the transmission eigenstates, which are determined by the

transmission matrix through the sample. This matrix is in general quite large, since it has

terms for flux between every state in the ideal leads on one side of the sample and the

other. The statistics of the eigenvalues of large, random matrices have been studied,

however, first in the context of the excitation spectra of compound nuclei [Wigner]

[Dyson]. The eigenstates of such matrices follow different statistical ensembles based on

the symmetry properties of the matrix. The symmetry classes are Gaussian Orthogonal

Ensemble for time-reversal and spin symmetry, Gaussian Unitary Ensemble for spin

symmetry only, and Gaussian Symplectic Ensemble for broken time and spin symmetry.

All of these ensembles feature level repulsion. That is, the probability that two states will

exist with a given energy separation goes to zero as the separation goes to zero. This

reduces the size of fluctuations in the spectra significantly, and makes the expected size

of fluctuations in a region of energy independent of the number of eigenstates in that region. Schematically, the eigenstate spectrum can be compared to a ladder, where the spacing between rungs usually only varies by a limited amount. The expected number of rungs in a given distance (energy range) does not change much in different regions of the ladder, compared to the expected fluctuations if we remove the constraint that controls the rung spacing. The size of the fluctuations in conductance can be calculated based on the number of independent statistical sequences of eigenstates and the symmetry of the transmission matrix or Hamiltonian [Imry] [Al'tshuer and Shklovskii] [Muttalib et al.] [Beenakker]:

$$\left\langle \left(g - \langle g \rangle \right)^2 \right\rangle \propto \left(\frac{e^2}{h} \right)^2 \frac{ks^2}{\beta}. \tag{3.9}$$

The brackets represent averaging over the ensemble of impurity configurations. Here k is the number of independent sequences of eigenvalues of the transmission matrix, s is the degeneracy of eigenvalues, and β is 1, 2, or 4 for GOE, GUE, or GSE, respectively. The constant of proportionality depends on sample dimensionality. As we can see, Random Matrix Theory (RMT) allows us to relate the size of conductance fluctuations to e^2/h, irrespective of the sample's conductance.

This RMT approach is particularly useful when we can experimentally change the symmetry of the transmission matrix or Hamiltonian. Then dramatic relative changes in the amplitude of the variance of g (Equation 3.9) can be observed. One such application is the observation of the factor of two reduction of low temperature 1/f noise at large magnetic fields [Stone] [Birge et al., 1989]. In this example, application of a magnetic field breaks time-reversal symmetry in the sample, and we see a drop in noise power of a

factor of 2. In order to consider the effects of finite temperature and sample size in UCF, however, another theoretical approach was required.

III D.   Perturbation Theory

Using perturbation theory under the Kubo formalism, one can calculate the ensemble average conductance and its variance directly. Lee, Stone, and Fukuyama used the ergodic hypothesis described earlier to relate changes in magnetic field or chemical potential to (impurity) ensemble-averaged calculations in perturbation theory. Their expansion parameter was $(k_f l)^{-1}$, which is much larger than 1 in weakly-disordered metallic samples. They diagrammatically calculated the correlation function for conductance as a function of magnetic field and chemical potential:

$$F(\Delta E, \Delta B, B) = \langle \delta g(E_F, B) \delta g(E_F + \Delta E, B + \Delta B) \rangle, \qquad (3.10)$$

where $\delta g(E, B) = g(E, B) - \langle g(E, B) \rangle$. (See Lee et al. for the results of this calculation). Note that $F(\Delta E, \Delta B = 0)$ is simply $Var(g)$. The scales in energy or magnetic field where F falls to $\frac{1}{2} Var(g)$ were identified as the correlation energy or field. Lee, Stone, and Fukuyama calculated the correlation field and energies as a function of sample size and dimensionality, temperature, and τ_φ. They found that the correlation energy is sometimes determined by the Thouless energy, E_c, and other times by kT, depending on sample geometry and temperature. The correlation magnetic field is basically set by the condition that magnetic flux through the coherent region be equal to h/e, but the size of the coherent region can be determined by L_φ, the sample size, or the thermal "coherence" length, $L_{th} = (\hbar D / kT)^{1/2}$. Recall that the breadth of the Fermi-Dirac distribution function about E_F is set by kT. L_{th} represents the distance that two nearly coherent quasiparticles

separated in energy by kT can diffuse before they accumulate enough phase shift to become incoherent.

III E.   UCF-Enhanced Sensitivity to Impurity Motion

Another feature of the UCF mechanism is that the conductance of mesoscopic metallic samples is highly sensitive to small changes in the impurity potential. Multiple visits to impurities by coherently diffusing quasiparticles magnify the effects of motion of those impurities on the conductance [Al'tshuler and Spivak] [Feng et al.]. In fact, the motion of one scatterer could cause the conductance to fluctuate by up to e^2/h in sufficiently small samples. This is the same fluctuation that is expected when all of the scatterers are randomly relocated; that is, the conductance of two ensemble members is expected to differ by e^2/h. Experimentally, samples are not usually in this so-called "saturated" regime, and the change due to the relocation or reorientation of a single defect is much less than e^2/h. This sensitivity explains many early observations. Discreet jumps in resistance were observed in very small, cold conductors, attributed to the motion of defects [Beutler et al.]. Defect electromigration was evidenced by changes in the resistance noise amplitudes in metal nanobridges [Ralls et al.]. Conductance fluctuations in silver samples were shown to have both magnetic field-dependence and time-dependence, with similar amplitude [Meisenheimer and Giordano]. Tunneling defects resolved in resistance jumps at low temperature in amorphous conductors were shown to have roughly consistent densities with those inferred from the specific heat anomaly of glasses [Garfunkel et al.]. In addition, this mechanism was proposed as a source of the 1/f noise enhancement in metals observed at low temperature [Feng et al.].

In metals, a broad distribution of excitations leads to resistance noise with a power spectrum that increases as $1/f^{\alpha}$, with $\alpha \approx 1$. From 100K to 500K, a distribution of thermally-activated, hopping systems with barrier heights about 1eV and a width of 0.3 eV can explain the observed resistance fluctuations in a variety of metals [Dutta et al.]. Consider the case of a two-level system that is activated by thermal fluctuations. The transition rate of such a system is given by $\tau = \tau_0 e^{\frac{E}{kT}}$, where E is the energy barrier height and τ_0 is the average time between attempts. If we assume a wide distribution of E compared with kT, then the density of states as a function of $\ln(\tau)$, $D(\ln(\tau))$, will be constant. The power spectrum of one switching two-level defect is a Lorentzian, with knee frequency given by the total transition rate. Specifically,

$$S(\omega) = \frac{2\tau}{1 + (\omega\tau)^2}, \tag{3.11}$$

where $\frac{1}{\tau} = \frac{1}{\tau_{up}} + \frac{1}{\tau_{dn}}$. The total fluctuation for the distribution of TLS we write as

$$S_R(\omega) = \int D(\tau) \frac{2\tau}{1 + (\omega\tau)^2} d\tau. \tag{3.12}$$

If $D(\ln(\tau))$ is constant, or $D(\tau) \propto 1/\tau$ (which is equivalent), then the resulting spectrum of fluctuations is proportional to $1/\omega$ (1/f) [Dutta and Horn]. Later, it was pointed out that a broad distribution of tunneling excitations could also provide a 1/f noise spectrum [Ludviksson et al.].

The 1/f noise power in metals is seen to increase as temperature decreases below a few K and electron coherence becomes important to conduction processes. A proposed explanation [Feng et al.] was that L_{φ} and L_{th} increase as temperature is lowered, and

therefore so does the sensitivity of the conductance of the sample to defect motion. In Chapter 2, we saw that the under the Tunneling Model of amorphous solids, a distribution of two-level systems exists with a broad range of excitation energies and asymmetries. Their effects persist in the thermal and acoustic properties of glasses at temperatures below 1 K. Recall that the incoherent tunneling rate of a TLS in a metal (Equation 2.31) is a function of the broadly-distributed tunneling parameter Δ_r. This results in a broad distribution of tunneling rates and a slowly-varying density of states as a function of the logarithm of the tunneling rates. Thus, we find a $1/f$ fluctuation spectrum, following Equation 3.12. We can surmise that in amorphous metals, tunneling defects may provide the mechanism for $1/f$ noise to persist even below 1 K.

The definitive test that showed that low-temperature $1/f$ noise is enhanced by the UCF mechanism was application of a magnetic field. Fields large enough to break the time-reversal symmetry of the scattering matrix lower the noise power by a factor of two, due to changes in the statistics of the eigenstates. The detailed crossover function between RMT statistical ensembles has been calculated for $1/f$ noise power as a function of magnetic field, again using impurity-averaged perturbation theory [Stone] [Hoadley et al.].

The next experimental advance was measurement of the tunneling parameters of individual mobile defects in mesoscopic metals. The dynamics of TLS in metals are described by the theory of Dissipative Quantum Tunneling, as was described in Chapter 2 of this thesis. By measuring the tunneling rates (Equation 2.31) from observations of resistance jumps, the energy asymmetry of a single TLS as a function of magnetic field was studied [Zimmerman et al.]. Later, the detailed dependence of the tunneling rates on

the ratio of ε to kT was observed [Golding et al., 1992] [Chun and Birge, 1993]. Excellent agreement was found with Dissipative Quantum Tunneling theory, including the novel increase of tunneling rate as temperature is lowered. These observations have established resistance measurement as a probe of the dynamics of individual tunneling defects in disordered metals.

IV.   Conclusion

The work described in this Thesis is a study of the effects of an external perturbation on individual, atomic-scale tunneling systems. We observe the motion of an active TLS by measuring the conductance of a mesoscopic metallic sample at low temperature. Due to quasiparticle coherence, conductance becomes a probe into atomic-scale changes in the microscopic impurity potential. In practice, we locate a bi-stable defect system with resistance values different enough to be easily resolvable (at least a few Ohms). Then, we can apply a perturbation to the system and measure directly the effects that it produces on the dynamics of the defect. The TLS in amorphous solids are strongly coupled to strain, as has been seen in the average values of the deformation potential that have been inferred from acoustic and thermal measurements in glasses [Beret and Meiβner]. By applying known strain to a metallic sample in the UCF-regime and observing the corresponding changes in tunneling rates, we directly measure the deformation potential for individual tunneling systems.

Chapter 4

Experimental Concerns

I.   Introduction

In this Chapter I will discuss various steps required in the fabrication and measurement of a sub-micron sample. In order to conduct these experiments, samples were fabricated, mounted and cooled in a cryostat, and subjected to external perturbations. Our results were all obtained from measurements of the conductance of the samples under those circumstances.

Samples are produced via electron beam lithography (EBL), an established method of fabricating sub-micron sized metallic samples [Broers, et al.]. The process involves application to a suitable substrate of at least one layer of a chemical sensitive to bombardment by electrons, called e-beam resist. After a controlled exposure in a scanning electron microscope (SEM), the desired regions of this film are removed by a developer. Metal is then deposited everywhere on the substrate, and the underlayer of e-beam resist is removed, leaving behind only the metal which landed directly on the substrate.

Electrical connection between the EBL sample and the electrical leads in the cryostat is facilitated by a larger lead pattern produced with another step of lithography, this time using resist which is sensitive to light. Photolithography affords lower

45

resolution, with the wavelength of the UV exposure light being the ultimate limit, but a broader field of view. At 1500x in the SEM, the maximum field of view is typically less than 100μm. Thus, a larger field, lower resolution exposure is essential. It is useful to use a different deposition step for the outer leads, both to lower the sample's two-terminal resistances and in order to have a more robust contact for final connection to the world off of the substrate. We chose 120nm gold pads. The disadvantage, however, is that alignment of the EBL pattern onto the existing contact pattern is necessary. An SEM micrograph of a finished sample can be seen in Figure 4.1.

Once produced, the sample is mounted in a cryostat and mechanical strain is induced via a wafer of PZT-5A, a piezoelectric ceramic. Magnetic fields were applied with a superconducting solenoid that is wrapped around the outside of the sample chamber in the cryostat. All of these steps will be described in greater detail in the sections that follow.

II.   Sample Preparation

II A.   Electron Beam Lithography

Electron beam lithography involves the use of a scanning electron microscope in a modified way. The focused electron beam, which usually rasters across the sample, is controlled via a computer and used to write a pattern on the desired sample. The two main parts of this system are X and Y position controls, which are realized as currents in the scan coils of the SEM, and a beam blanker, which allows exposure only when the beam has reached its desired position. The remainder of the system is mostly a user interface. There are software packages to turn an input drawing into parameters to be
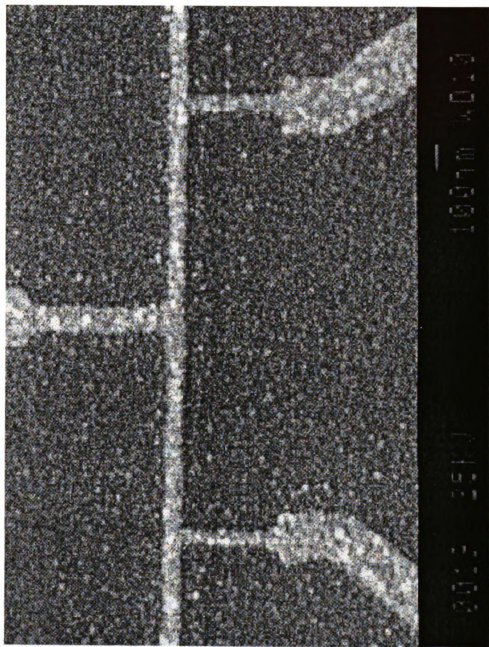
Figure 4.1 SEM micrograph of a Test Sample at 50,000 X Magnification. The line width is 60-70 nm.

passed to the SEM. The software that I used was the Nabity Pattern Generation System, NPGS. The user inputs a DesignCAD drawing of the sample area, and can assign different electron beam doses to different regions of the drawing, denoted as layers or colors in the CAD drawing. Typical doses for these samples were 0.8 - 1.2 nC/cm as line dose and 275 μC/cm^2 in the large area pads. The ultimate resolution of PMMA is about 20 nm, but in general a few factors degrade this. The first requirement for good lithography is a highly accurate correction to the shape of the electron spot, accomplished by removing astigmatism from the electron optics. Additionally, the focus on the surface of the resist should be of the highest quality. A fundamental limitation, however, is the widening of written patterns by the backscattering of electrons from the substrate, either during exposure of the pattern or from areas of the pattern nearby. These degradations are known in this field as proximity effects. They are lowered by increasing the acceleration voltage, since higher energy electrons are more likely to travel through the resist and be lost deep in the substrate. There are always some of these effects present, however. I have used a bi-layer resist scheme to produce a good undercut, allowing ease of liftoff in the last step of this processing procedure. After exposure, the pattern is developed in methyl-isobutyl-ketone (MIBK), which develops the top and bottom layers one after the other. The bottom layer has an increased sensitivity to electron dose which provides the essential undercut for liftoff processing. The choice of electron beam resist is very important, and the particular resists I used will be described below. Further description of the EBL process itself can be found in the doctoral theses of J. S. Moon and K. Chun [Chun] [Moon].
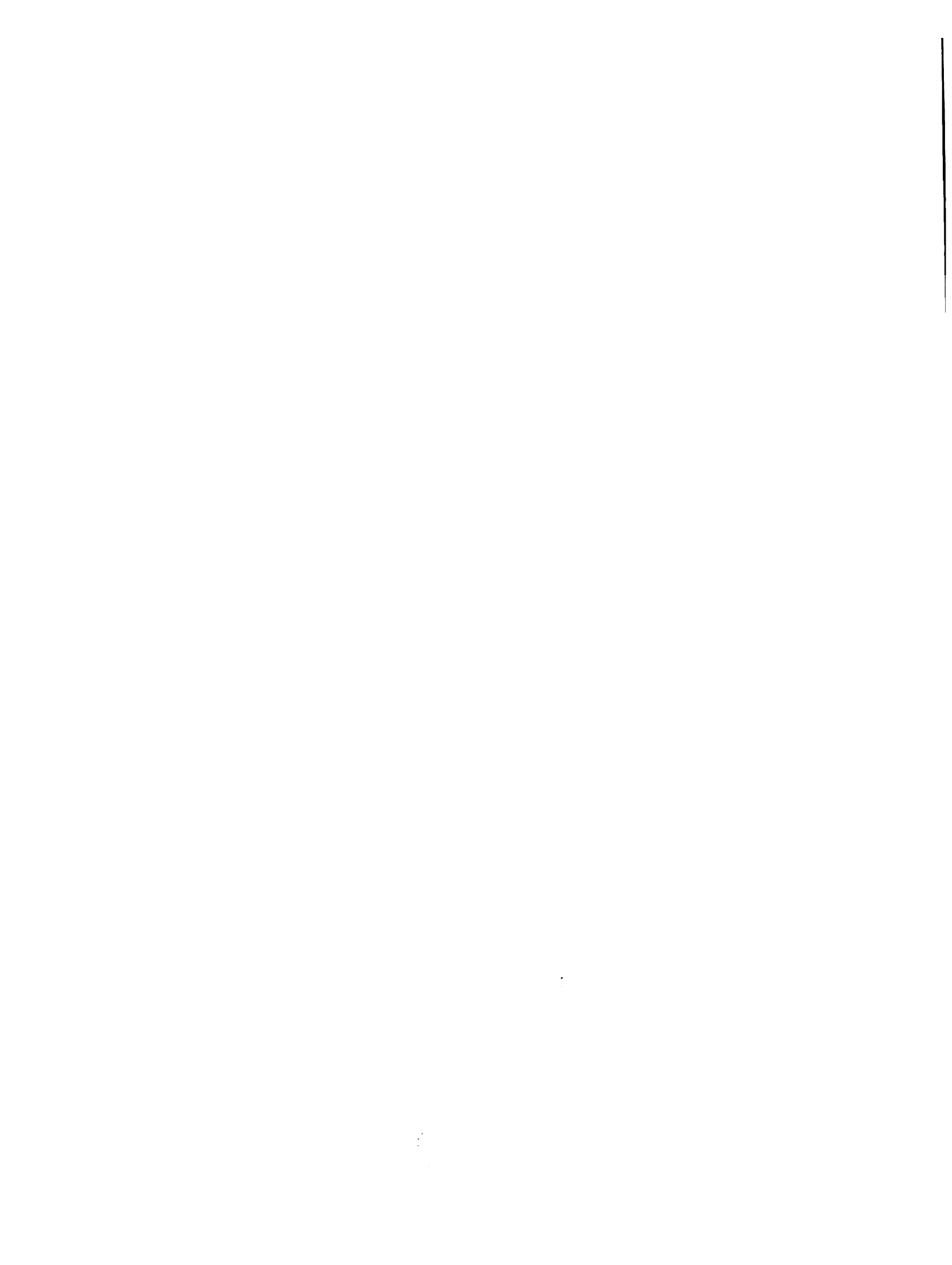
II B. Choice of Substrate Material

Substrate choice plays a very important role. The initial data run for the defect-strain experiment was performed on a glass substrate, formed from a fraction of a Corning #1 glass cover slip. This was chosen due to its availability, electrically insulating nature, and most importantly its thickness - roughly 5 thousands of an inch (mils). One possible choice of substrate would have been the PZT-5A wafer itself. These materials are porous, however, and a very effective planarization step would have been necessary to carry out the lithography. It seemed simpler to use a very thin substrate atop the PZT and calibrate the strain for losses thereby incurred (See Appendix A for strain calibration details). The cover slips thus seemed a natural choice. Unfortunately, EBL is not reproducible on top of an insulator. The incident writing beam deposits charge on the substrate, changing the character of the beam as it scans over the sample. This is a familiar occurrence to SEM users, since long-term beam exposure degrades images. We attempted to remove substrate charging with the deposition of a 15nm thick aluminum layer atop the e-beam resist. The metal layer was thin enough that it was nearly transparent to the incident high-energy beam electrons but still electrically continuous. This was a step in the right direction, but still left us with dissatisfying results. These problems were solved with the use of 5 mil (.005") thick silicon wafers, P-type doped to 1-10 Ω-cm, as substrates. (These wafers were commercially available from Silicon Quest International, a silicon wafer broker.) At room temperature, these substrates are conductive and we achieve very reproducible lithography. At low temperature, the carrier density plummets and the substrates become insulating. The only

disadvantage here is that we could not determine with total certainty whether a sample

existed on the substrate at room temperature. By 77K, however, the substrate

conductance could easily be separated from that of the sample, as the former is already

nearly an order of magnitude smaller than the latter.

II C.   Substrate Preparation

Careful substrate preparation is also vital to successful EBL. Table 4.1 shows the

"recipe" that I followed. Additionally, I will point out some details. Precise substrate

cleaning is essential. Treatment with hot Micro (a commercial soap) has proven to be a

suitable degreasing and dust-removing process. The e-beam resists that I have used are

2% PMMA (Polymethyl Methylacrilate) dissolved in chlorobenzene and 9%

PMMA/MAA copolymer dissolved in 2-ethoxyethanol. As a final note, I point out that

the use of a controlled, clean environment is very helpful. The MSU Microfabrication

Facility features a class 1000 clean room with controlled temperature and humidity.

II D.   Photolithography

To make contact with the small features written with the SEM, we use optically

patterned leads. The particular process we use is a type of triple-layer photolithography

and is pictured schematically in Figure 4.2. The bottom layer is a blanket-exposed layer

of a standard photoresist, in this case Shipley type 1813. The evaporation mask is formed

by the middle layer, 35 nm of thermally evaporated aluminum. The top layer is again

photoresist, in which the desired pattern is exposed. The pattern is developed using

Microposit 452 photoresist developer. The development process proceeds in this manner:

first, the top layer of photoresist is developed, revealing the aluminum layer in the shape

of the exposure pattern. Next, the pattern is etched into the aluminum layer.

1)

Photoresist
Substrate

Blanket Exposure

2)

Aluminum —
Photoresist
Substrate

Metallization

3)

Al
Photoresist
Photoresist
Substrate

Pattern Exposure

4)

Photoresist
Al Photoresist
Substrate

1.3 microns
35 nm
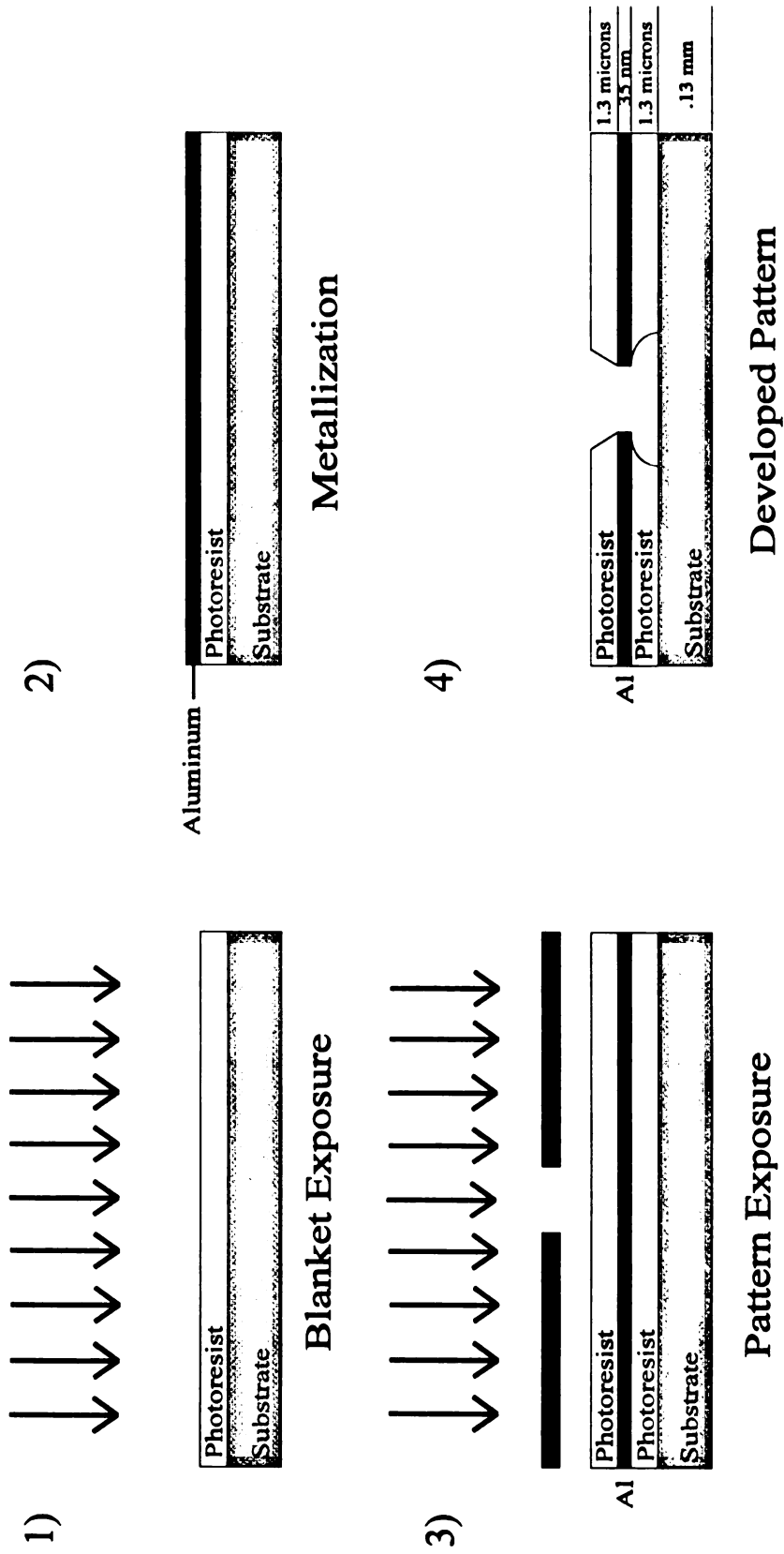1.3 microns

.13 mm

Developed Pattern

Figure 4.2 Schematic Depiction of the Processing Steps in Photolithography
The first three panels show the substrate in various stages of completion.
In the last we see a developed pattern with a typical undercut of a few microns.

Fortuitously, our photoresist developer served as a useful etch for the aluminum, and no separate etch processing step was required. Once the aluminum is etched, the bottom photoresist layer develops rapidly. This step exposes the bare substrate in the shape of the top-layer pattern, but with a large undercut. Gold leads are then deposited onto a spinning substrate at an angle of roughly 45 degrees through this mask, producing a lead pattern with tapered edges (Figure 4.3). These allow good contact between the typically 120 nm-thick gold pads and the <30 nm samples. Adhesion of the gold to the substrate is assisted by a thin layer (2 nm typically) of chromium, deposited immediately before the gold.

II E.   Metal Deposition

Metallization of the substrate occurs in a thermal evaporation system. A molybdenum boat is used to heat high-purity (5 9's) bismuth under moderate vacuum conditions ($<10^{-6}$ torr). The mean free path of a gas at this pressure is much larger than the dimensions of the system's bell jar, so bismuth atoms travel directly from the boat to the sample and arrive with little transverse momentum. 25 nm of material is deposited at rate of 1-2 nm per second, monitored by a crystal film thickness monitor. This process produces polycrystalline films with typical grain sizes of about 30 nm. Low temperature sheet resistances are in the range of a few hundred ohms per square (Figure 4.4). The resistivity varies very rapidly with film thickness in this regime, so the uncertainty in the film thicknesses here play a major role in the variation seen in film resistances.

III.   Cryostats

Bismuth defect experiment sample measurements took place in a pumped liquid helium-4 cryostat at temperatures from 1.2 to 2.2 K for the study of single defects.

Microscope   NSIII AFM
Scan size   15.2 μm
Setpoint   0.0 U
Scan rate   1.9 Hz
Number of samples   256

view angle
light angle

0 deg

X   5.000 μm/div
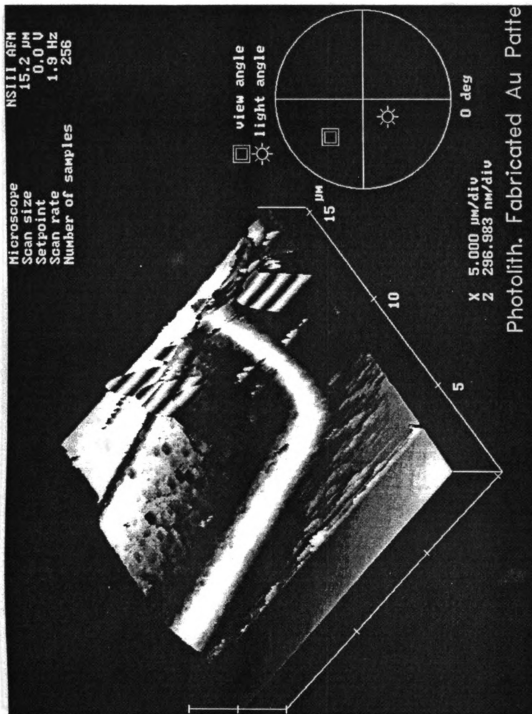2   296.983 nm/div

Photolith. Fabricated Au Patte

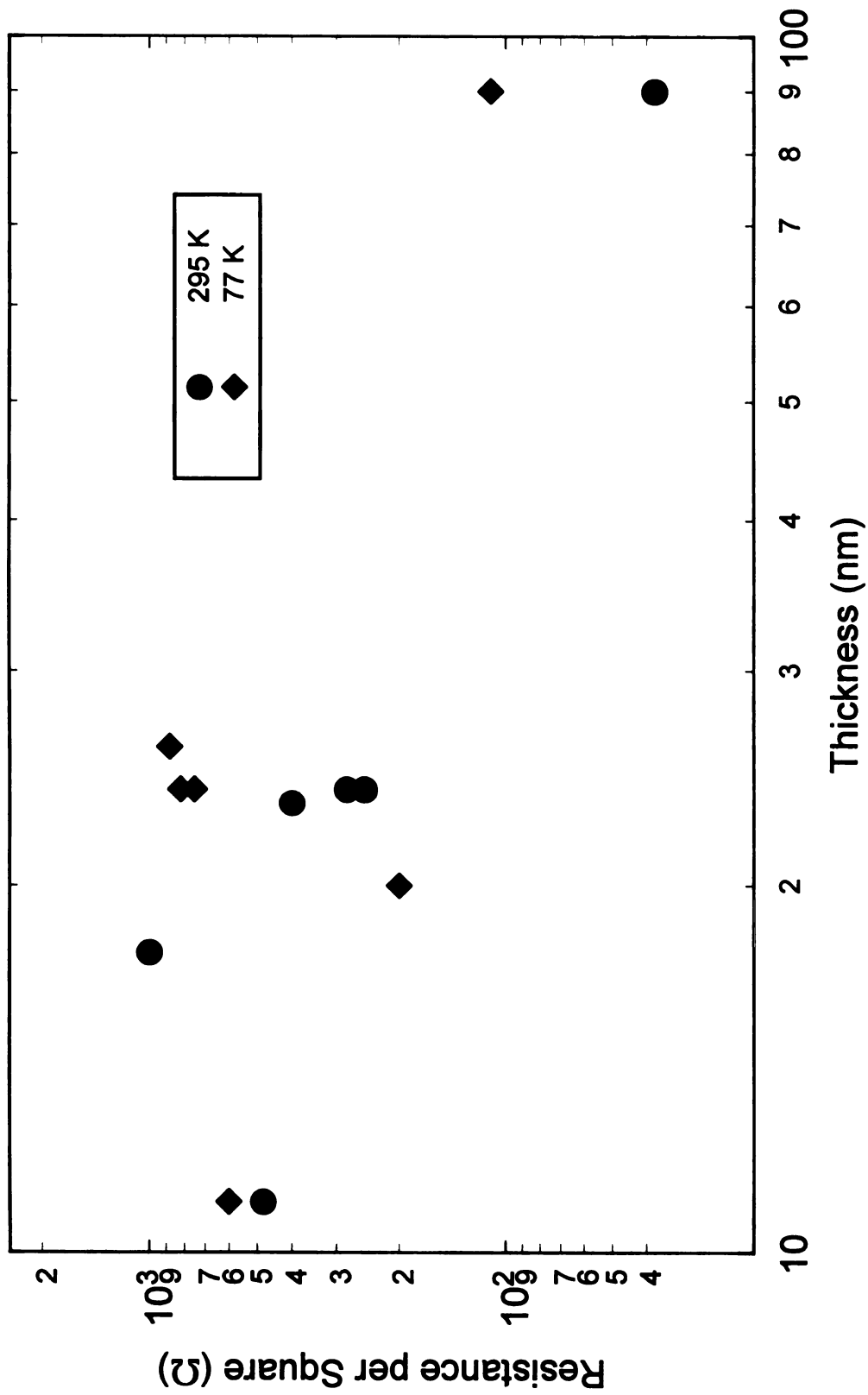Figure 4.3   AFM Image of Gold Contact Pads With Tapered Edges

Figure 4.4 Variation of Sheet Resistance for Thin Film Bismuth

This Figure shows that the sheet resistance of bismuth films deviate from 1/thickness behavior over the observed range of thicknesses due to sample preparation, since these data represent films fabricated by three different people using two different evaporators.
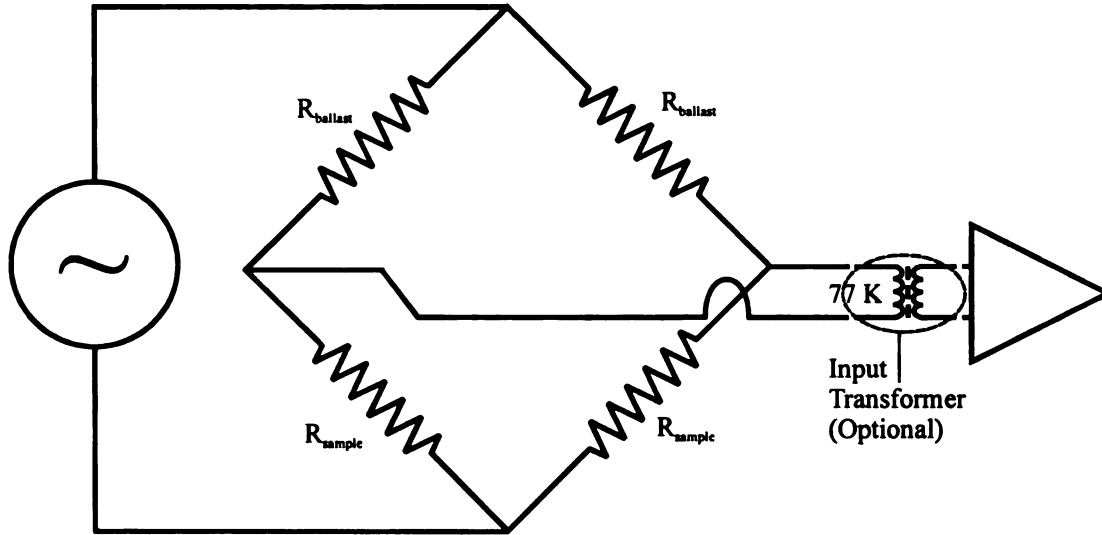
54

Figure 4.5a - Five terminal circuit diagram. The excitation voltage passes through ballast resistors and the sample resistances, arranged as a Wheatstone bridge. When the signal is nulled properly, the output of the pre-amp will be very sensitive to changes in one arm of the sample or the other. The optional 77 K cooled input transformer can be used for samples with low resistance.
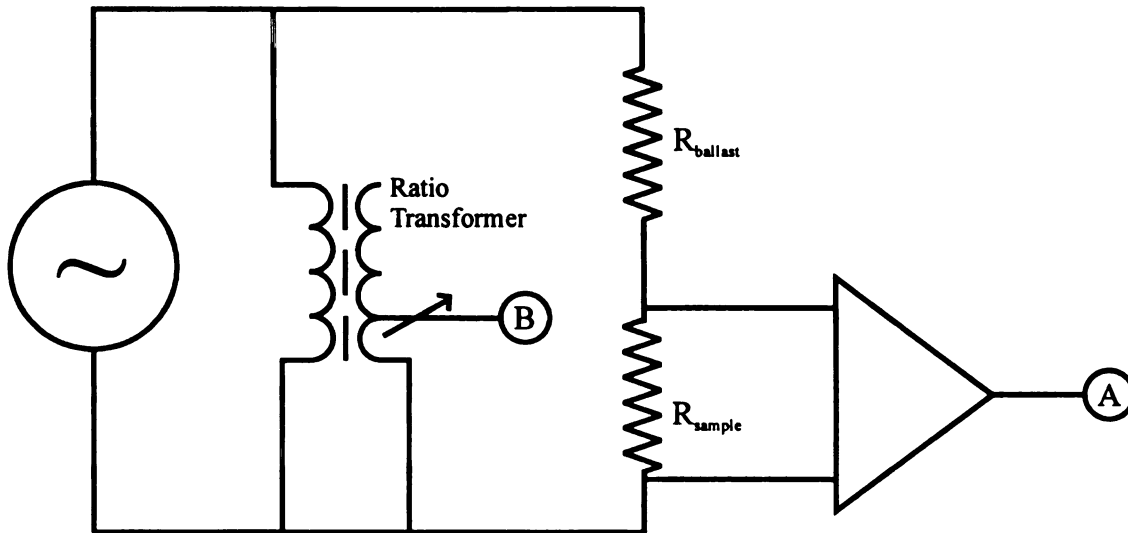

Figure 4.5b - 4-terminal measurement circuit. Excitation is provided by a voltage source and then passes through a ballast resistor. With values of the ballast much larger than the sample resistance, we simulate a current source. The final stage of amplification is the difference between signals A and B, the output of the ratio transformer. This circuit allows measurements of $\Delta R/R$ as small as 1 part per million..

The cryostat uses a 1K pot system to provide cooling power. Data for the silver project were collected in a similar cryostat in the temperature range from 1 to 29 K. The study on conductance fluctuations as a function of strain was carried out in a helium-3/-4 dilution refrigerator from 29 to 200 mK. In all cases, magnetic field was applied with superconducting solenoids, providing fields of 0-7 Tesla in the helium-4 cryostat and 0-9 Tesla in the dilution refrigerator.

IV.   Measurement Circuits

IV A. 5-Terminal AC Bridge

Defect sample measurements were made using an AC bridge method [Scofield]. The circuit uses the two arms of our five-terminal samples as the bottom half of a Wheatstone bridge (see Figure 4.5a). There are several advantages that we gain from this type of measurement. The first is that the circuit is insensitive to noise in the driving voltage, since both arms of the bridge receive an equal contribution. Another large advantage is the insensitivity of a balanced bridge to interference, which enters both arms. As long as the preamplifier has good common mode rejection, these fluctuations are largely suppressed. Additionally, the bridge circuit allows us to compensate for any difference between sample resistances by changing the relative size of the ballast resistors. We can null the average signal from the two channels, thereby increasing our sensitivity to change in one arm of the sample or the other. Sample resistance fluctuations of one part in 10^5 are then easily resolved.

IV B. 4-Terminal Measurement

Another circuit was used for magnetoresistance measurements. Rather than using all five terminals of a sample in a bridge circuit, we made direct four terminal resistance

measurements. We formed a modified bridge in this case with a ratio transformer as one arm (Figure 4.5b). This allowed once again a differential measurement that achieved one part in 10^6 accuracy.

IV C. RF Filters

Missing from all of the simplified circuit diagrams shown in Figures 4.5 a and b are numerous RF filters on the lines leading into the cryostat. Every electrical lead on the cryostat is filtered at least once with an LC filter with loss of 20 dB at 10 MHz. These are mounted at the ends of cables leading into the cryostat. The sample leads and high voltage leads also have RC filters with a rolloff frequency of 1 MHz after the leads enter the vacuum can. It seems that these RC filters were necessary to stop the all-too-frequent destruction of a sample caused by propagation of some transient high-frequency signal during loading or mounting. Attesting to their effectiveness, the sample measured after the addition of the RC filters survived three cool-downs and the repair of a high voltage lead. This was unprecedented robustness for sub-micron samples in our 1K system.

V.   Strain System

Strain is induced in our submicron bismuth sample via voltage applied to the electrodes of a piezoelectric wafer. PZT-5A is the industry name for a particular lead zirconate titanate ceramic that exhibits a ferroelectric phase transition with Curie temperature of 350 ° C. The strain produced upon application of an electric field between the top and bottom electrodes of the type of wafers that we used was uniform planar strain. We performed experiments with two kind of PZT-5A wafers. The first was a bimorph, featuring two PZT layers separated by a middle electrode. Later, we found similar results with a single-layer wafer, where we could use a simpler wiring technique.

The single-layer PZT-5A were purchased from Staveley Sensors. PZT-5A wafers are commercially available in various thicknesses. The amount of strain produced is proportional to the electric field between the electrodes. Therefore, thinner layers of PZT produce more stain for a given voltage. The piezoelectric layer needs to be thicker than the sample substrate, however, in order to produce strain in the sample. Our bi-morph wafers had two 10-mil layers of PZT, and the single-layer wafers had one 10-mil layer. We operated the bi-morphs with the back electrode shorted to the middle one, effectively reducing the wafer thickness. Both wafers then produced low-temperature dimensionless strains of roughly 10^{-5} with an applied voltage of 100 V, giving a low temperature measurement of $d_{31} = 33 \times 10^{-12}$ m/V as the strain response of the PZT. d_{31} is the strain induced in the plane perpendicular to the voltage applied between electrodes on the top and bottom of the PZT wafer.

The temperature dependence of PZT-5A has been previously studied [Fein, et al.] [Vandervoort, et al.], and we have used commercial alloy strain gauges to calibrate the strain propagated through both the glass and silicon substrates. We found similar reductions in the strain produced by the PZT at low temperature with a previous study. For details of the calibration process, see the Appendix.

Table 4.1 Electron Beam Lithography Procedure on Non-insulating Substrates

Substrate cleaning:

    30 minute soak in 70 ° C 5% Micro soap, 95% deionized water (DI)

    Thorough rinse in DI

Resist preparation:

    Spin on PMMA/MAA (9%) at 4900 RPM for 60 seconds (200-300 nm)

    Bake bottom layer at 160 ° C for 60 minutes

    Cool to room temperature

    Spin on PMMA (2%) at 4900 RPM for 60 seconds (150 nm)

    Bake top layer at 160 ° C for 60 minutes

    Cool

Exposure:

    Add trace amounts of silver conducting paint for focus target on substrate

    Load into microscope; saturate filament at 35 KV accelerating voltage

    Allow 10 minutes after saturation for beam stability

    Focus and stigmate on standard

    Repeat on Ag paint target on substrate

    Align sample areas and expose to beam

Developing:

    Soak in MIBK/isopropanol (IPA) 1:3 for 70 seconds at 20 ° C, agitating

    Rinse in IPA for 30 seconds

    Rinse in DI for 30 seconds

Chapter 5

Strain-Induced Conductance Fluctuations

I.   Introduction

Here I will describe measurements of the conductance of a mesoscopic bismuth

sample (100 nm x 1.5 μm x 20 nm thick) as a function of applied magnetic field and

strain. Figure 5.1a shows the variation of the conductance of such a sample at four

temperatures (45, 90,145,200 mK) as a function of applied strain. Present are random,

reproducible fluctuations that have suggestively similar amplitude to those in Figure 5.1b.

There we see a plot of the magnetofingerprint of the sample at the same temperatures,

which is explained by UCF theory [Lee et al.]. These random, reproducible fluctuations

grow in amplitude as the temperature is lowered, while the amount of field change

necessary to significantly alter the sample conductance decreases. This observed

sensitivity to applied strain, however, was an unexpected result. The amount of strain

necessary to change the conductance is $4*10^{-7}$ at 45 mK. I will now describe the analysis

that explains the existence of the "strain fingerprint" of this mesoscopic sample. These

effects can be described by the theory of UCF as described in Chapter 3.

II.   Data Analysis

Fingerprint data is analyzed via the autocorrelation function,

$$F(\Delta B) = <G(B)G(B+\Delta B)>, \text{ or } F(\Delta e) = <G(e)G(e+\Delta e)> \qquad (5.1)$$

in the case of strain-induced fluctuations, averaged over the range of field of the experiment. This is realized computationally by stepping along the data points in the trace and calculating the product of G(B) and G(B+ΔB) (or G(e) and G(e+Δe)). G(B+ΔB) is found by simple interpolation between the data points nearest B+ΔB. This allows continuous calculation of the autocorrelation as a function of ΔB and is immune to inconsistent data point spacing in field, which can occur due to limitations in the data collection system. Plots of all of the autocorrelation functions for conductance versus magnetic field and strain for all measured temperatures are shown as Figures 5.2a-e and 5.3a-f. The behavior of these plots at large ΔB or Δe comes from the lack of sufficient statistics due to the finite range of field which can be applied in these experiments. From these plots we can obtain two physically interesting quantities. The first is the variance of the conductance fluctuations, given by $<(G^2(B)-<G(B)>^2 >= F(\Delta B = 0)$ (Equation 5.1). The same is of course true for strain-induced fluctuations on replacement of B by e. Secondly, the value of ΔB when the autocorrelation function falls to 1/2 its zero-field value is defined as the correlation field, B_c. This value sets the scale of the change in field required for the conductance to change by on average the r.m.s. value of the fluctuations. Both of these quantities are predicted in the case of magnetic field by UCF theory. It was natural to try and determine whether the same mechanism was at work in the case of the strain fingerprint.

61

III.   Dephasing Length

The prediction for the correlation field of a quasi-1D sample is given by the simple expression

$$B_c = \frac{1.2\phi_0}{L_\varphi W},$$

(5.2)

where W is the width of the sample [Lee et al.]. Equation 5.2 holds true when the sample width and thickness are less than L_φ. In these .1 μm wide by 25 nm thick samples, this is always the case below about 0.5 K. Figure 5.4 shows the dependence of the phase-breaking length versus temperature obtained from the values of B_c shown in Figures 5.2 a-e. The low-temperature behavior of the phase-breaking length in metals is not yet completely understood. The $T^{-1/3}$ dependence predicted in a 1-D sample due to small-energy-transfer electron-electron interactions [Al'tshuler, Aronov, and Khmel'nitskii] is not realized in our data. There is also a recent experimental result that shows a saturation in the phase-breaking length for many different metals [Mohanty et al.]. This result is also not indicated by our data, however. We consider L_φ to be only an experimentally determined parameter for the purposes of calculations in the remainder of this chapter. We do not have enough data to make convincing arguments for or against a particular temperature dependence of L_φ.

IV.   Amplitude of Fluctuations

UCF theory gives the expected value of the amplitude of magnetic-field-induced conductance fluctuations for samples of varying dimensionality based on the relative sizes of applicable length scales [Lee et al.]. A difficulty arises, however, in describing the complete set of physical parameters for bismuth films. The properties of thin film

62

bismuth are quite different from that of its bulk form [Komnik et al.] [Kochowski and

Opilski] [Komori et al.]. For UCF theory calculations, we need to compare the dephasing

length from Figure 5.4 with the size of the thermal length, which reduces the fluctuations

observed due to the distribution of electron energies at the Fermi level:

$$L_{th} = \sqrt{\frac{\hbar D}{kT}} \, .$$

(5.3)

The difficulty arises in estimating D, the diffusion constant, for our films, which can vary

extensively with sample preparation and thickness. We have chosen a value of $D = 30$

cm^2/s for our films [Birge et al, 1990]. This leads to a thermal length that varies from .7

to .34 μm as $1/\sqrt{T}$ from 45 mK to 200 mK. In the regime of $L_\varphi < L_{th}, L_{sample}$, we can

express the variance of the conductance fluctuations at finite temperature as

$$\delta G^2 = C \left(\frac{e^2}{h} \right)^2 \cdot \left(\frac{L_\varphi}{L_{sample}} \right)^3 \, .$$

(5.4)

The value of the constant C is determined by the symmetry of the Hamiltonian of the

system and the dimensionality of the wire. In a magnetic field larger than B_c, the

contribution to the fluctuations due to the Cooperon channel are suppressed, leading to a

decrease by a factor of two in the size of the observed fluctuations. In bismuth at low

temperature, strong spin-orbit scattering reduces the observed fluctuations by a factor of

4. C is then 0.53 * 1/2 * 1/4 for this quasi-1D conductor in the strong spin-orbit regime

and in the limit of large field $(B > B_c)$. We exclude the region $B < B_c$ from the

autocorrelation calculations, which is roughly 1% of the total field range at 45 mK.

There is an additional factor to consider due to our experimental setup, which is that the

two arms of a five terminal sample are modeled as two independently fluctuating

samples. Thus, the total variance we measure is twice that of a sample 1/2 as long. This is a poor approximation when the sample size is not much larger than the phase-breaking length, however. Additionally, I have assumed that the two samples are identical, when in fact their resistances differ slightly. This enters calculations of the variance of g in the fourth power, however, since $\left|\dfrac{\delta G}{G}\right| = \left|\dfrac{\delta R}{R}\right| \Rightarrow \delta G = R^2 \delta R$. In Figure 5.5, we plot the conductance fluctuations as a function of temperature due to variation of both strain and magnetic field. There is some scatter among these points, but we must recall that the number of independent fluctuations that occur is small over the entire accessible range of strain, and so the uncertainties are expected to be large. We see that the fluctuation amplitudes increase as temperature is lowered and the phase-breaking length increases. Since L_φ varies as $T^{-1/2}$, we can expect the variance of G(B) to increase as $T^{-3/2}$ (Equation 5.4), which is consistent with our data. Most importantly, we note that at each temperature the amplitude for strain-induced fluctuations is nearly twice that of their magnetic field counterparts. This is exactly what one would expect if the strain-induced fluctuations were a UCF phenomenon, since the variance with strain was measured at zero magnetic field, which corresponds to an increase of a factor of two as compared with the variance at fields larger than B_c. Table 5.1 compares the values of the variance of the conductance expected due to UCF with those measured as a function of strain and magnetic field. Given this expected factor of two difference, the variance of G(e) and G(B) agree remarkably. All of the factors that lend uncertainty to the UCF calculation in the last column of Table 5.1 do not affect the agreement of the first two, since both sets of measurements were carried out in the same sample.

Table 5.1 - Conductance Fluctuation Variance Comparison. For five temperatures, we compare the variance of the conductance as a function of magnetic field and strain. The last column is the single-parameter UCF prediction. Variance data is displayed in units of $(e^2/h)^2$.

Temperature (mK)	Var(G(B)) $(e^2/h)^2$	1/2Var(G(e)) $(e^2/h)^2$	$C/8(L_\varphi/L)^3$
45	.0066	.0068	.029
65	.0054	.0055	.020
90	.0058	.0036	.0090
145	.0033	.0023	.0048
200	.0016	.0012	.0028

V.   Strain Correlation Field

The autocorrelation functions of conductance versus strain give a measure of the amount of strain necessary to produce a change in conductance of order e^2/h (see Figure 5.6). The surprising thing to note is that at 29 mK, this correlation strain, σ_c, is 5×10^{-7}. This corresponds to a change in length less than $1/100^{th}$ the size of one atom over the length of the sample. We believe that the unusual sensitivity of the Fermi energy in bismuth to strain explains this result.

Our initial attempt to calculate the strain correlation field began by applying a uniform strain, σ, to the entire sample. Recall that quasiparticles move diffusively between scattering centers in a mesoscopic metallic sample at low temperature (Figure 3.2). The total phase-coherent path length of a diffusing quasiparticle is given by d = $v_F \tau_\varphi$. We know $L_\varphi^2 = D\tau_\varphi$ (Equation 3.2), where D is the diffusion constant, $\frac{1}{3} v_F l_{el}$.

The total diffusive path length is then $d = \dfrac{3L_\varphi^2}{l_{el}}$. The effect of isotropic planar strain will

be to increase this distance by d*σ. The accumulated phase change of the electron over

its entire phase-coherent path is therefore

$$\delta\phi = k_F d\sigma = 3\left(\frac{L_\varphi}{l_{el}}\right)^2 k_F l_{el}\sigma .$$

(5.5)

From UCF theory, we know that the conductance will change when this phase shift is of

order π, so we can write the correlation strain as

$$\sigma_c \approx \left(\frac{l_{el}}{L_\varphi}\right)^2 (k_F l_{el})^{-1}.$$

(5.6)

This can also be expressed as E_c/E_F, where E_c is the Thouless energy, $\dfrac{\hbar}{\tau_\varphi} = \dfrac{\hbar D}{L_\varphi^2}$

(Equation 3.7). Recall that E_c represents the energy uncertainty for an electron that

crosses a phase-coherent volume in a time τ_φ. For our sample, this gives a value of $\sigma_c =$

1.6×10^{-5} at 45 mK and 7×10^{-5} at 200 mK. These are about 50 times larger than the

observed values of 4×10^{-7} at 45 mK and 1.2×10^{-6} at 200 mK.

A more appropriate treatment considers the shift of Fermi energy in bismuth

under applied strain. Changing the Fermi energy by E_c leads to a change in conductance

of order e^2/h, as predicted by UCF theory [Lee et al.]. The conductance fluctuations we

see then are analogous to those observed in semiconductors as a function of applied gate

voltage. Then we have

$$\sigma_c = \frac{E_c}{\dfrac{dE_F}{d\sigma}} .$$

(5.7)

The value of the deformation potential for the Fermi energy in bismuth ranges from 2-7 eV, depending on the orientation of the applied strain relative to crystal axes [Hanson et al.]. Since we have measured a polycrystalline film, it is unclear which of these values should be used in comparison with our observations. With our value of E_c at 45 mK of 9.8×10^{-6} eV, this leads to a range of correlation strain of from 1.4 to 5×10^{-6}. This value is far closer to our observation at 45 mK of $\sigma_c = 4 \times 10^{-7}$. An important source of error could be the value of D we estimated earlier as 30 cm^2/s, since E_c is proportional to D. It should be noted as well that both of these estimates for σ_c vary as L_φ^{-2} (Figure 5.4) and therefore are expected to follow the observed temperature dependence, proportional to T (see Figure 5.6).

V.   Conclusion

In conclusion, we report the observation of strain-induced conductance fluctuations in a submicron bismuth sample at temperatures from 29 - 200 mK. These fluctuations have an amplitude that is described by the theory of Universal Conductance Fluctuations and feature very small correlation strains, as small as 4×10^{-7} at 45 mK. The size of the correlation strain field is explained by a shift in the Fermi energy of bismuth under application of strain, with deformation potentials for E_F in the realm of a few eV.
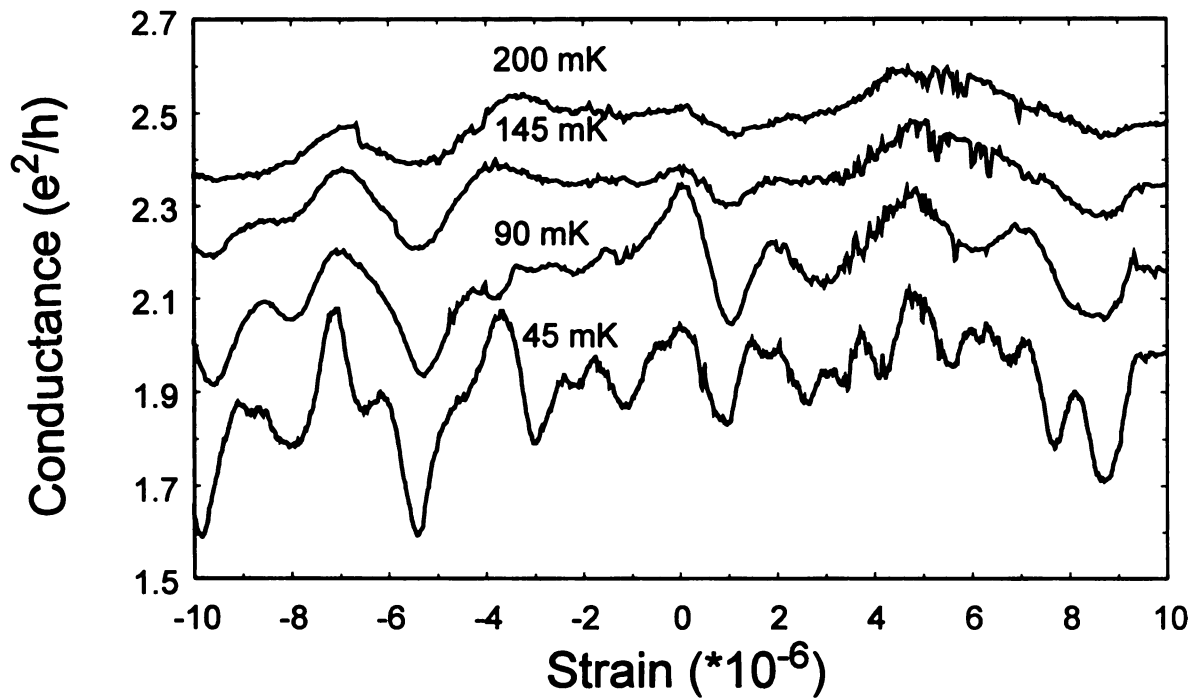
Figure 5.1a - Conductance Fluctuations as a Function of Mechanical Strain
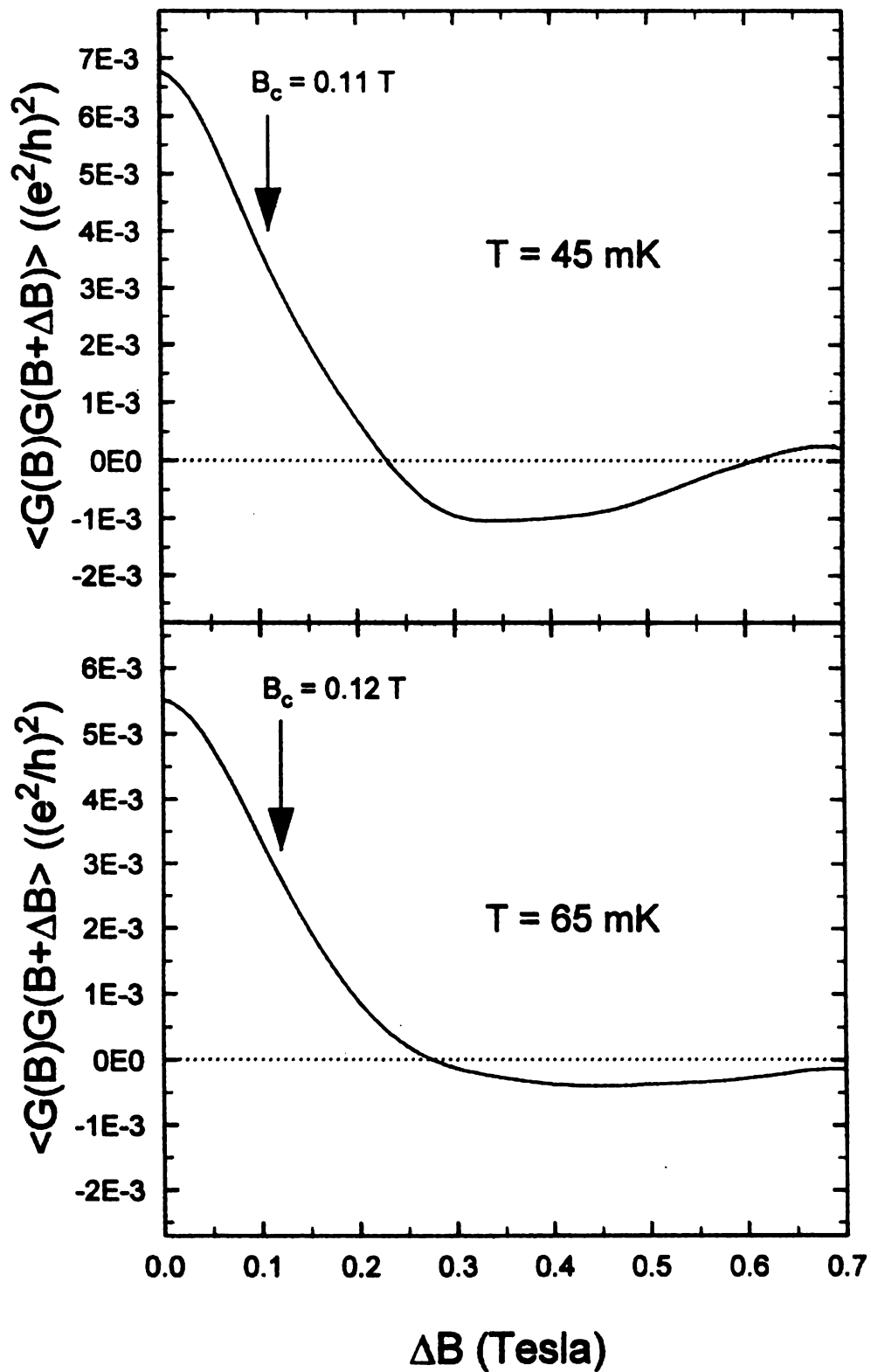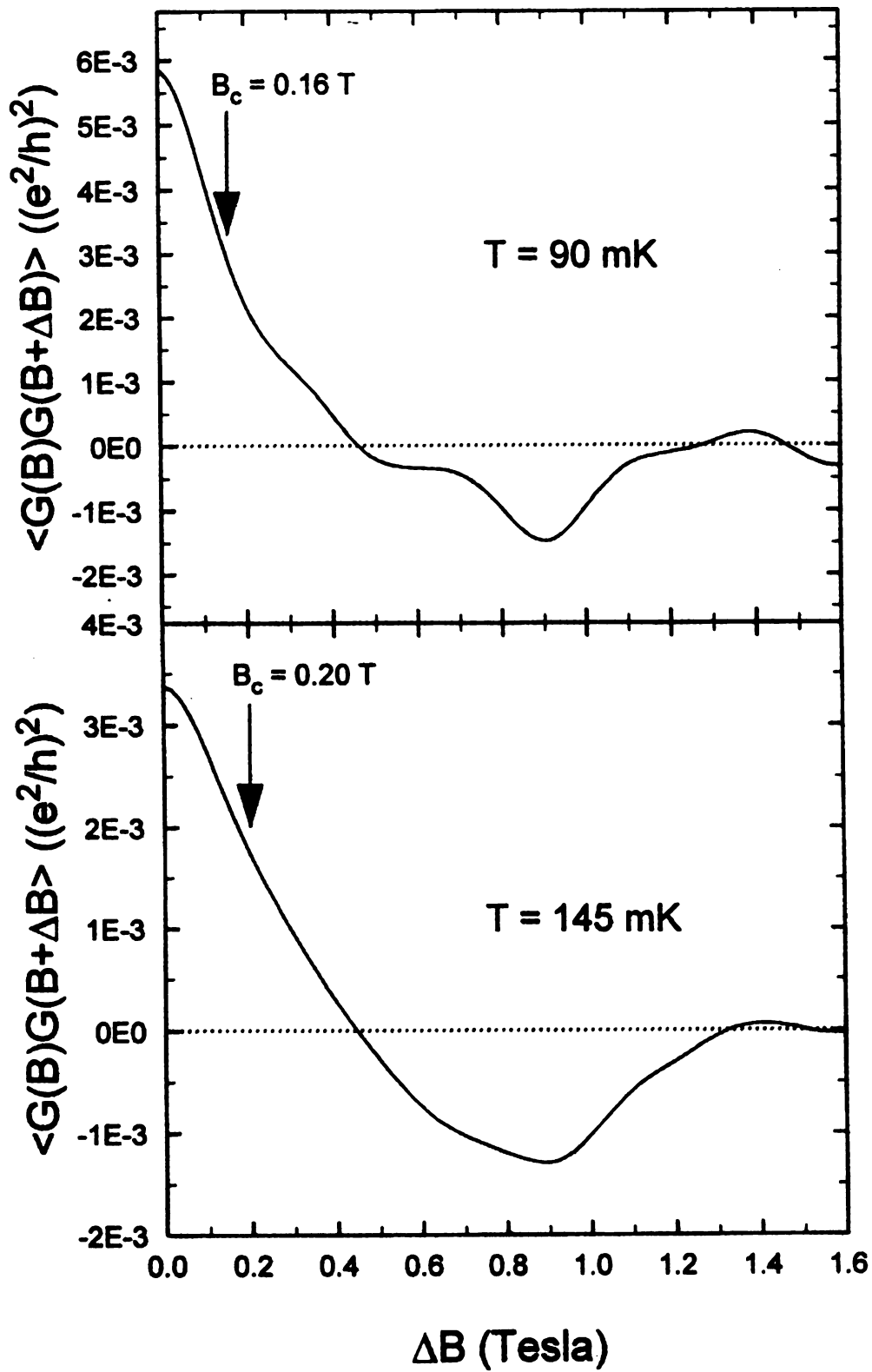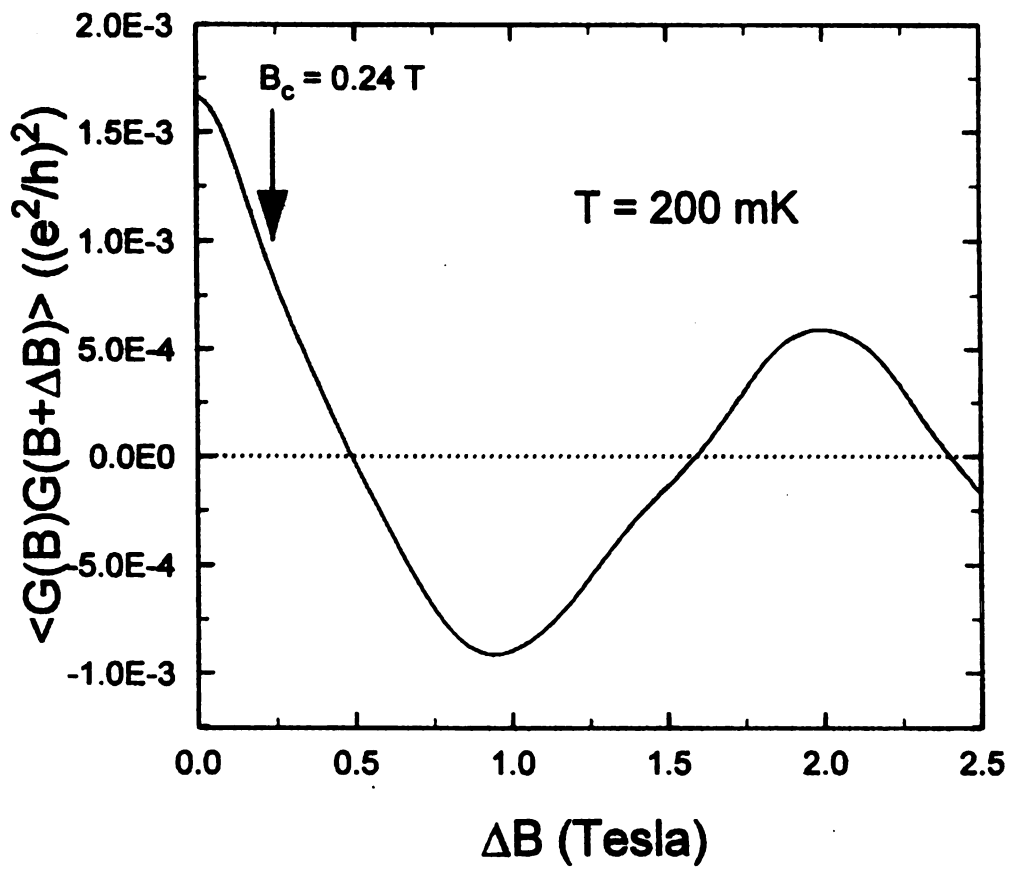The conductance of a mesoscopic bismuth sample varies by order e^2/h with strain.
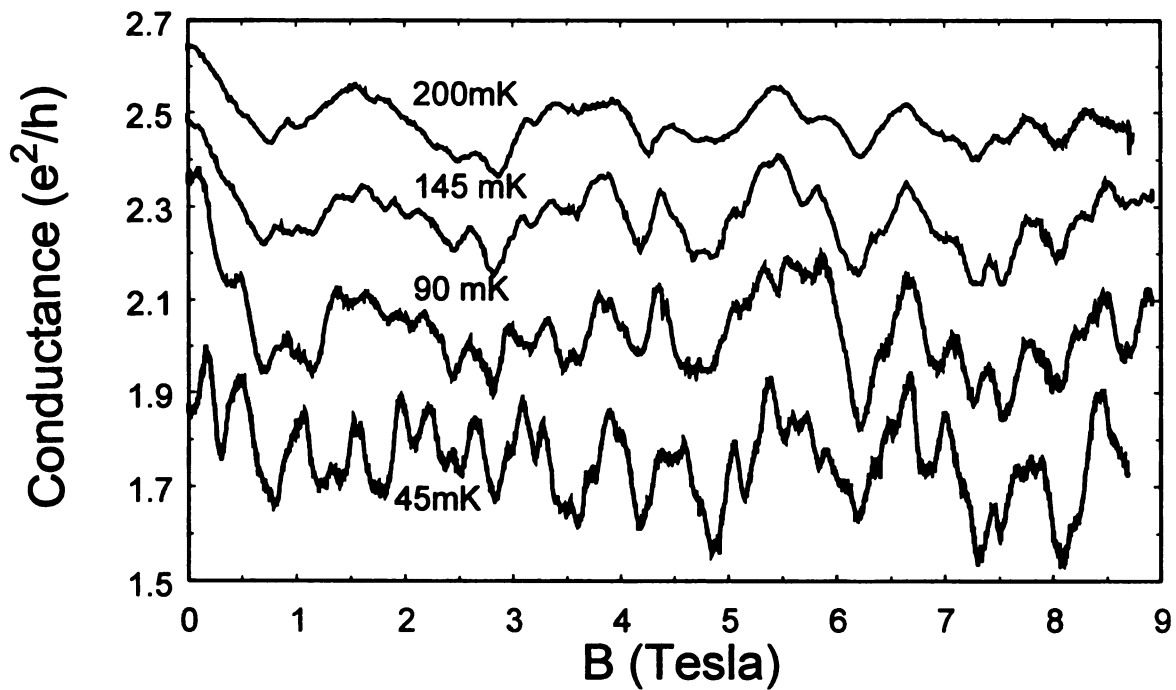
Figure 5.1b - Conductance Fluctuations as a Function of Magnetic Field
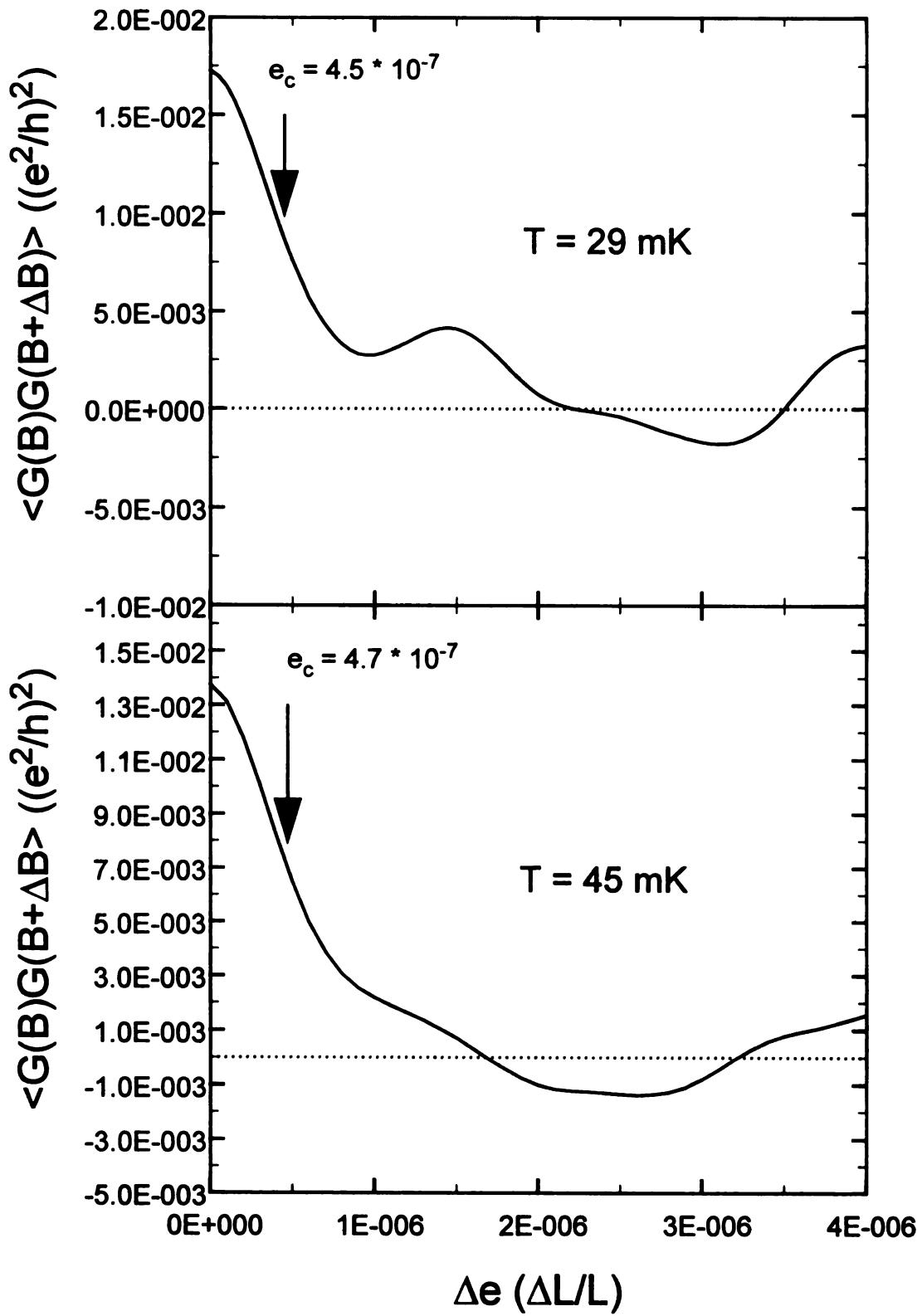This Figure shows the magnetofingerprint of the same sample.

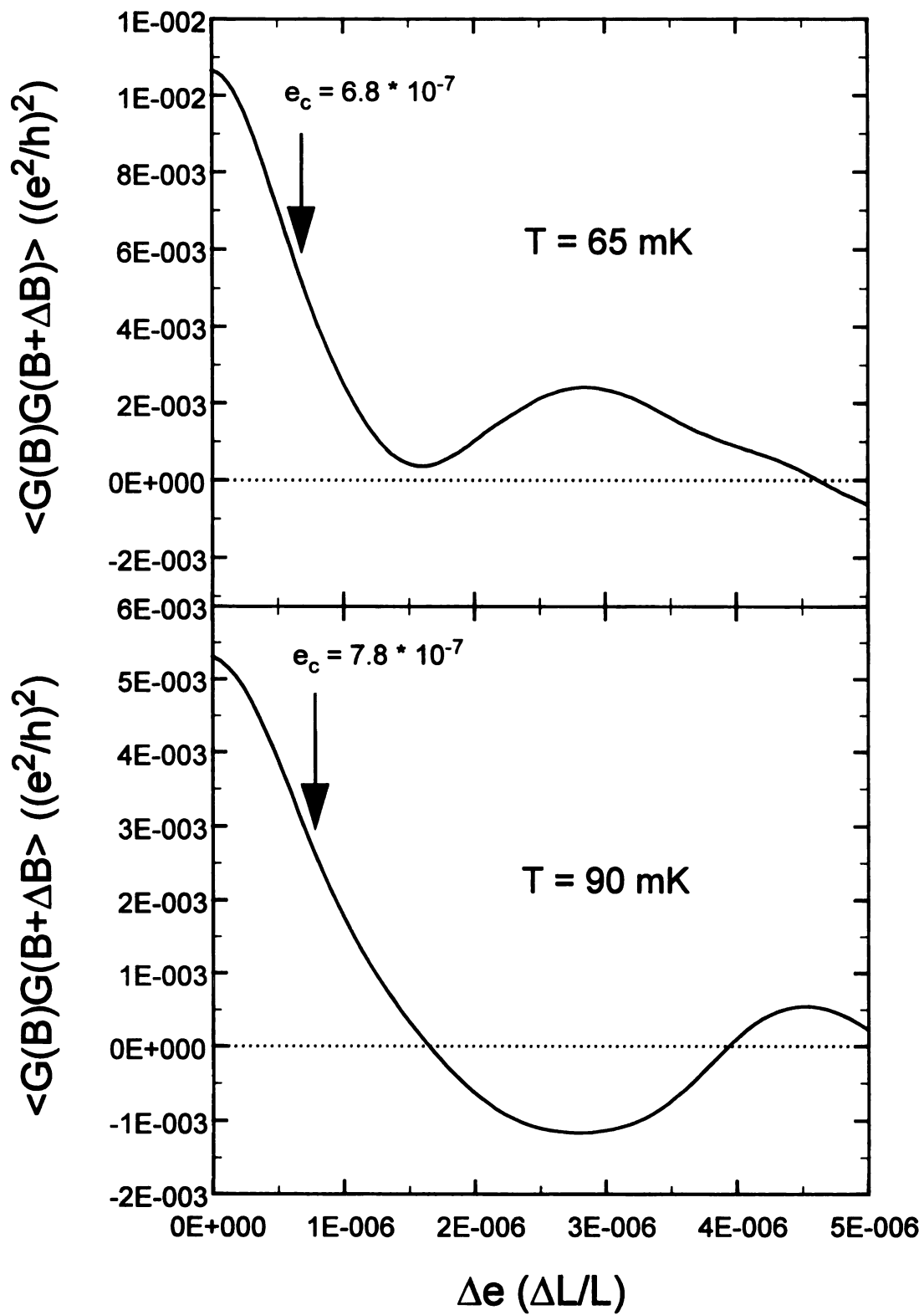Figures 5.2 a and b - Autocorrelation of Conductance vs Magnetic Field

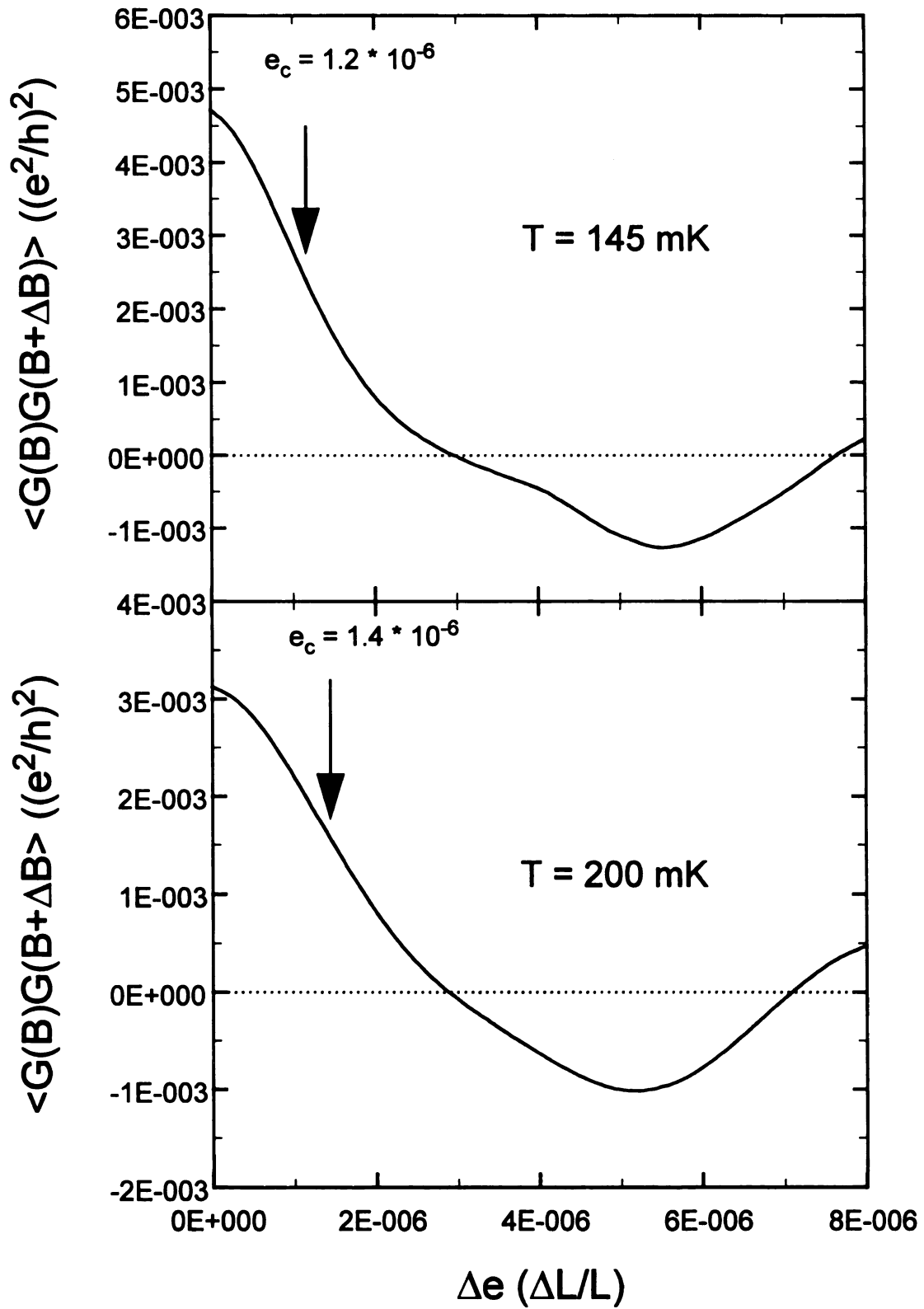Figures 5.2 c and d - Autocorrelation of Conductance vs Magnetic Field

Figures 5.2 e - Autocorrelation of Conductance vs Magnetic Field

Figures 5.3 a and b - Autocorrelation of Conductance vs Strain

Figures 5.3 c and d - Autocorrelation of Conductance vs Strain

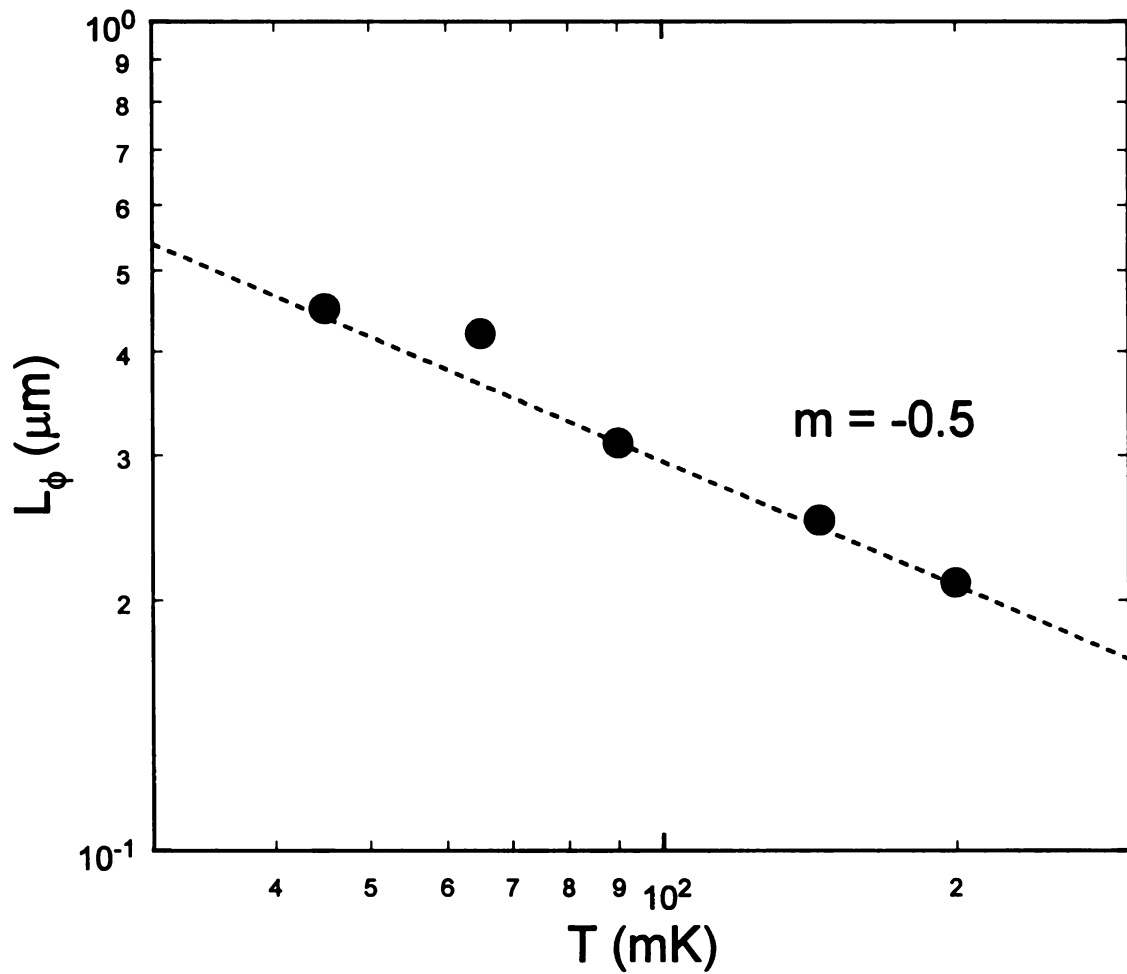Figures 5.3 e and f - Autocorrelation of Conductance vs Strain

Figure 5.4 Phase-Breaking Length Variation with Temperature
L_ϕ at each temperature is determined by the correlation fields found in Figures 5.2a-e.
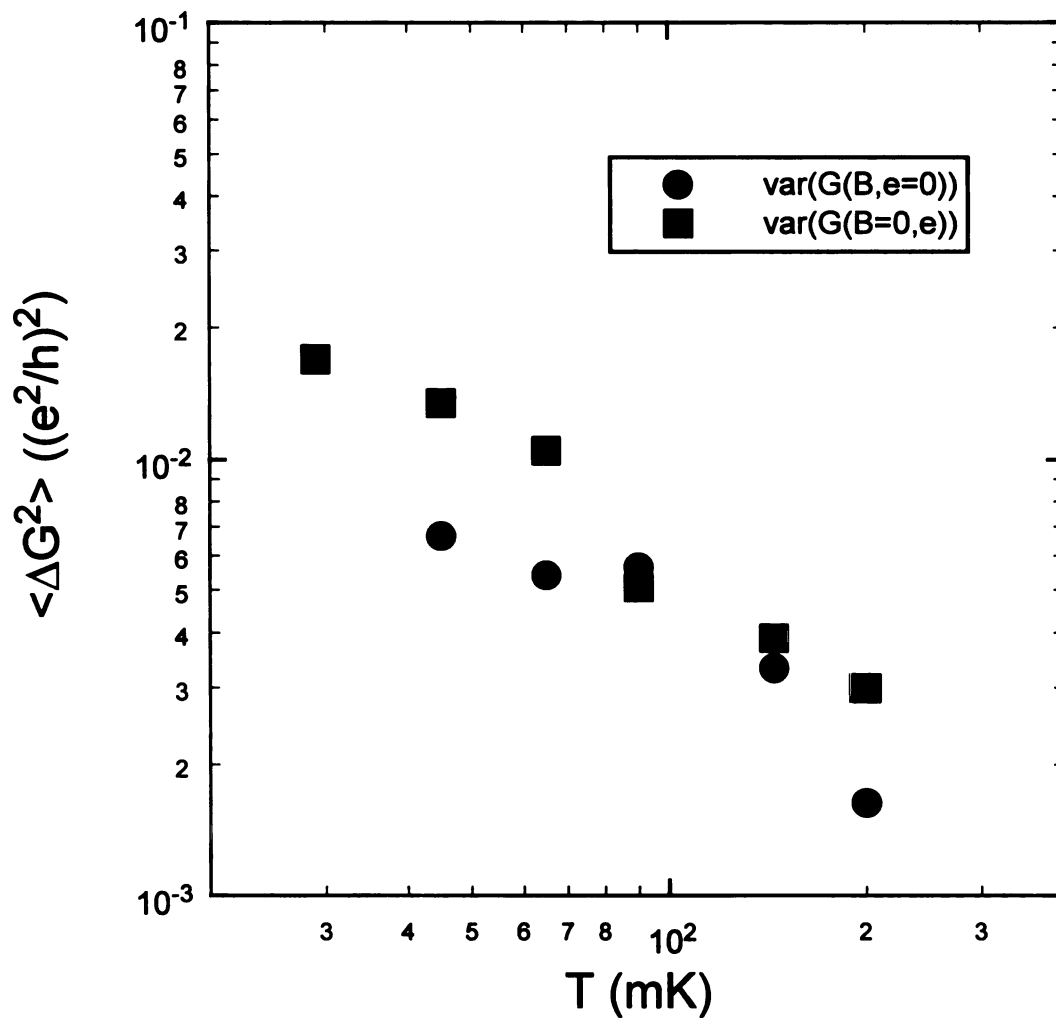The dashed line represents the observed temperature dependence, $T^{-1/2}$.

Figure 5.5 Variance of Conductance Induced by Magnetic Field and Strain
The average variance of conductance as a function of strain is roughly twice as large
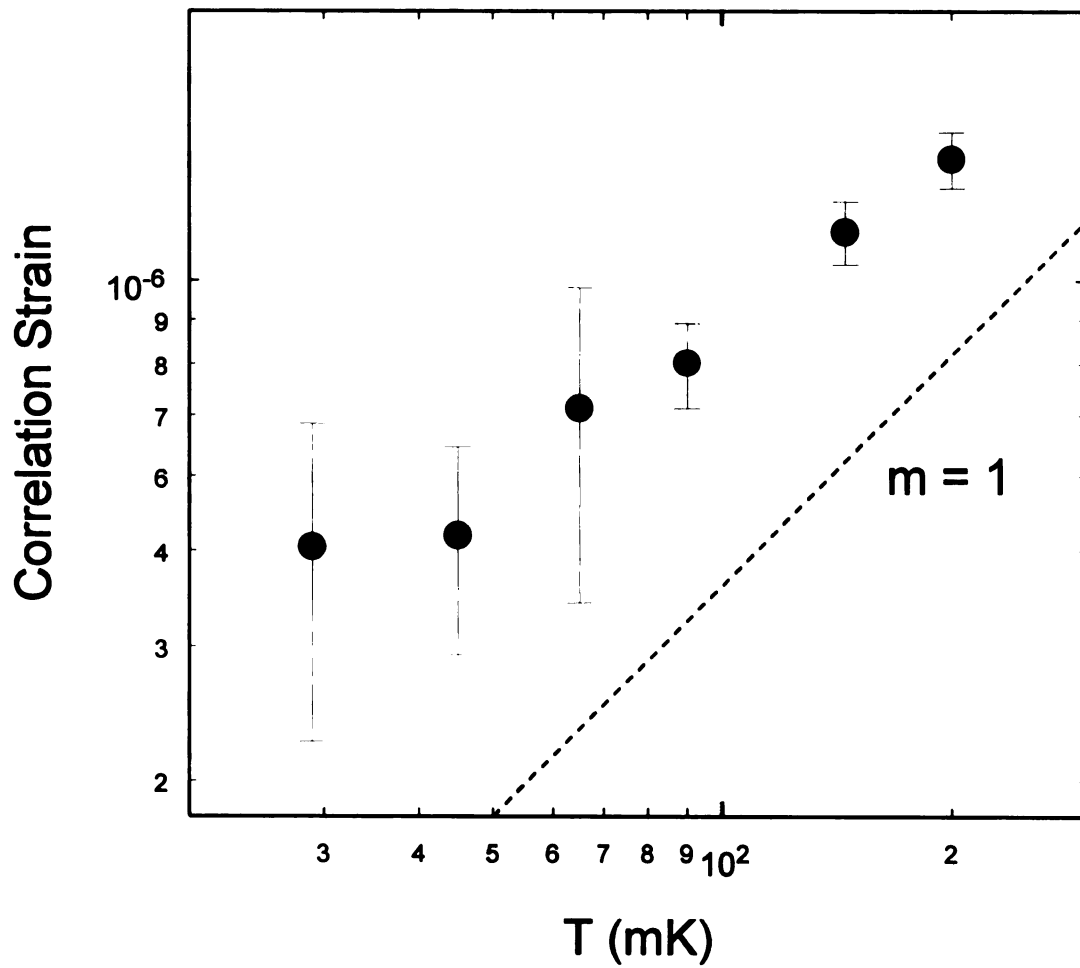as that induced by magnetic field.

Figure 5.6 Strain Correlation Field as a Function of Temperature
This Figure shows the correlation strain field obtained from Figures 4.3 a-f.
The dashed line indicates the apparent dependence on the temperature.

Chapter 6

Response of Defect Dynamics to Strain

I. Introduction

Here I describe the results of our studies of single defects under applied strain in four submicron bismuth samples. We will see the effect of strain on the microscopic local potentials of these defects, which induces changes in their tunneling parameters, most notably the energy asymmetry between wells, ε. The response of ε to strain is γ, the deformation potential of the TLS (Equation 2.12).

II. Data analysis

Defect data are collected over long time periods as traces of voltage versus time. In order to achieve sufficient precision in our determination of the dynamical parameters, we require the collection of from 500-1000 transitions. For example, in order to record 600 transitions with the defect labeled below as "C", the time required was roughly 12,000 seconds. This placed our statistical uncertainties ($1/\sqrt{N}$) at 5% or lower. The actual error estimates will be described in detail, but this is a good initial estimate. Data reduction from these time traces occurs via one of two methods, which we have found return statistically equivalent estimates of the desired parameters. These methods were developed by Kookjin Chun during his doctoral work at Michigan State University, and

are documented in his thesis [Chun]. I will briefly describe these data analysis methods here as well for completeness.

II A.   Schmidt Trigger Comparators

The first data reduction method is very labor-intensive. Each file is viewed a small portion at a time and comparator levels are set by the operator to indicate the voltage levels at which transitions take place. During the following description of the operation of the Schmidt triggers, I refer the reader to Figure 6.1. The user first inputs the initial state of the fluctuator at the beginning of the file (up, in this case) and then sets the desired trigger levels. The analysis algorithm marks transitions as events when, starting from the upper(lower) state, the voltage passes below(above) the position of the lower(upper) trigger level. The important feature of the Schmidt trigger algorithm is that noise in the voltage signal can be rejected by careful choice of the comparator levels. The output of the first reduction program is a pair of files of the dwell times in each state. The set of from 8 to 20 files for a given strain were analyzed in this method, with all dwell times stored in two files, one for the "up" state, and one for the "down" state. I should mention that the labels "up" and "down" refer only to the output voltage of the lock-in, and do not necessarily reflect the relationship of the potential energies of these states. The state with longer average dwell time is the one that lies ε in energy lower than the state with the shorter dwell time.

The second step in this analysis process involves fitting a histogram of the dwell times (such as that pictured in Figure 6.2) in each state to an exponential probability

distribution, given by $P(\tau) = e^{-\frac{\tau}{\tau_0}}$. The number of observations in each bin in the histogram should then be

$$N_{bin} = N_{total}(e^{-\frac{\tau_{min}}{\tau_0}} - e^{-\frac{\tau_{max}}{\tau_0}}),$$
(6.1)

where τ_{min} and τ_{max} describe the extent of the bin in question. We fit the logarithm of the frequency in each bin to a line, with slope given by the mean dwell time, τ_0, and intercept determined by the total number of transitions, N_{total}. (The fitting algorithm we have used is the standard Levenberg-Marquardt method [see, for example, *Numerical Recipes in C*, Press et al.]. It returns error estimates on the desired parameters, as well as the values of the parameters themselves.) Allowing the total number of transitions to vary has a distinct advantage over fitting to merely the mean lifetime. There is a maximum bandwidth in our measurement circuit determined by the sampling rate of the ADC. In fact, we filter at a frequency corresponding to 1/4 of the sampling rate (which is 1/2 of the Nyquist frequency) in order to remove frequency aliasing. This implies that transitions that occur on time scales less than the inverse of our bandwidth are always missed. This can be seen as a deficiency in the first bin of Figure 6.2, which is ignored during the fitting process. Another detail is that the last bin of the histogram will contain the integrated number of transitions from the right side of the next to last bin to $t = \infty$. This accounts for its seemingly large frequency in the last bin in Figure 6.2. As a final note, we have used Poisson errors for the expected deviation in each bin, which is applicable for a collection of independent events.

II B. Gaussian and Debye-Lorentzian Fits

The second data reduction technique directly measures the ratio of dwell times in time trace data. It also features a two-step process. The first step is accomplished by fitting the power spectrum of the time-trace data to that expected from a single fluctuator. That expected power spectrum is a Debye-Lorentzian, introduced by Equation 3.11:

$$S(\omega) = \frac{2A\tau}{1+(\omega\tau)^2}.$$ (6.2)

The constant A is proportional to the voltage jump squared of the fluctuator signal and $\frac{1}{\tau} = \frac{1}{\tau_{long}} + \frac{1}{\tau_{short}}$ is the total TLS tunneling rate. One example of such a fit is given as Figure 6.3 in the form of a plot of f*S(f). There are three parameters in this fit, namely the amplitude, the knee frequency $(2\pi/\tau)$ and a 1/f contribution from the background of unresolved mobile defects. The 1/f tail is visible in the change in curvature in this plot at high frequency. The fit is plotted as f*S(f) for clarity so that the knee frequency in S(f) corresponds to the location of the peak in f*S(f).

The second step begins when a histogram is produced of the voltages present in the raw data. This histogram is then modeled as two Gaussians, with peaks separated by the average voltage difference between the two levels and widths given by the size of the white noise background present in the signal. Since this width is independent of the defect's location, the same width is fit to both Gaussians. The exact form of probability distribution as a function of V is

$$P(V) = \frac{1}{\sqrt{2\pi\sigma^2}}(A_1 e^{-\frac{(v-v_1)^2}{2\sigma^2}} + A_2 e^{-\frac{(v-v_2)^2}{2\sigma^2}}).$$ (6.3)

σ is the width of the distributions, and A_i, v_i are the amplitude and position of the ith peak. One example of such a fit is given by Figure 6.4. There are five parameters of interest, given by the locations of the peaks, their amplitudes, and the width of the distributions. Unfortunately, an occasional shift of the background due to the activity of a second mobile defect that is resolvable can seriously impact this automated method. To compensate, we devised a strategy where parts of the data records are fit independently and the results averaged together to find the mean parameters over an entire set of data. This allows the removal of segments of time trace data that did not fit the above combinations of Gaussians well by a test of the merit function, χ^2. χ^2 is the sum of the square of the deviation of each point from the fitting function's value, weighted by the expected error in that data point. Also, segments for which the fit returned an unusual value of the voltage difference or width of the distributions (both also good indications of model failure) are removed. The remaining majority of the data are averaged and the error estimates are based upon the statistical deviation in the set of 100 or so groups of parameters. The ratio of the areas under each Gaussian, which is the same as the ratio A_1 and A_2 from the fits, is the ratio of the dwell times. Averaged over all fitted segments of the time traces, this should be equivalent to the ratio of the mean dwell times returned from the comparator fitting procedure. Evidence of the validity of this statement is found in Figure 6.5, where I present the results for

$$\varepsilon = kT \ln(\frac{\tau_{long}}{\tau_{short}}) \qquad (6.4)$$

determined with both methods. We used the comparator method as the primary fitting technique and the automated fitting routines as a consistency check.

III.   Results

III A. Deformation Potentials

Figures 6.6-6.11 show the results of our experiments on the effect of strain on the dynamics of six two-level tunneling systems. We have acquired data for these defects which range in asymmetry from 0.3 to 4.4 Kelvin. The results of linear regression fits to asymmetry versus strain are present in Table 6.1 for all six defects observed. These parameters are derived from the best fit lines shown in Figures 6.6-6.11. These values are the first measurements of the response of individual TLS to strain. They may be compared with the results of phonon echo measurements in vitreous silica of a mean value of 1.5 +/- .4 eV [Graebner and Golding], and with many others in other glasses, some of which were summarized later [Berret and Mießner]. There average deformation potentials vary from 0.13 eV to 1.46 eV.

Table 6.1 - Asymmetry and Response to Strain for Six TLS. Sample 1 fabrication and data collection and analysis for defects A and B was accomplished by J. S. Moon

Defect	Sample	Temperature (K)	ε (K)	$d\varepsilon/d\sigma$ (eV)
A	1	1.0	1.83 +/- 0.05	0.3 +/- 0.9
B	1	1.0	1.60 +/- 0.04	1.6 +/- 0.5
C	2	1.3	1.47 +/- 0.03	3.4 +/- 0.4
D	3	1.3	0.33 +/- 0.02	-0.1 +/- 0.3
E	2	1.9	4.04 +/- 0.05	-0.4 +/- 0.6
F	4	1.25	0.6 +/- 1	-2.9 +/- 0.4

III B. Discussion of γ

We have observed deformation potentials from 0.1 to 1.7 eV for these six defects. The rough energy scale of γ for a TLS in the Tunneling Model is expected to be 1 eV [Phillips, 1972] [Anderson et al.] [Jäckle], which is in agreement with our observations. There are certain other expectations based on the information in the tunneling model. For example, a broad distribution of γ should exist. The local environments that make up the TLS in amorphous solids feature wide variation in physical parameters. The probability distribution for TLS's as a function of the energy asymmetry and the tunneling matrix element exponent, λ, is assumed to be independent of ε and λ over broad energy ranges [Phillips, 1972] [Anderson et al.]. A distribution in the response of these systems to strain is therefore quite naturally expected. Additionally, we expect that γ can vary for a single defect, depending on the type of strain that is applied and that defect's orientation. In general, we should consider the interaction of ε with strain as

$$H_{int} = \begin{bmatrix} 1 & 0 \\ 0 & -1 \end{bmatrix} \sum_{i,j} \Lambda_{ij} \sigma_{ij} \,, \tag{6.5}$$

where σ_{ij} are components of the macroscopic strain tensor and Λ_{ij} are the coupling constants to the i,j[th] components of that strain [Halperin]. Experimentally, we can only measure the net response of the defect in question to the particular strain that we can apply. Since the principle axes of Λ are randomly oriented in a disordered sample, we expect some variation in γ. We are not able to distinguish this variation in the deformation potential from the distribution inherent in the tunneling model of amorphous solids.

We find also that the response of the asymmetry to strain does not correlate with ε, since our two most responsive defects (C and F) had asymmetries of 1.3 and 0.5 K. Defect E, with the largest asymmetry of 4 eV, had a much smaller deformation potential. This is consistent with the tunneling model, where no correlation exists between the size of ε and its sensitivity to strain. Additionally, we note that there is no reason for the deformation potential to have any particular sign, which is reflected in our observations. The astute reader will have noted that in sample 1 the defect measurements only proceeded up to small positive strains, $+10^{-6}$ for defect A and $2.5*10^{-6}$ for defect B. This is due to a UCF effect similar to the conductance strain fingerprint described in chapter 5. When sufficient strain is applied, the interference pattern of conduction electrons that determines the conductance of a mesoscopic bismuth sample can change. This new interference pattern may feature different local densities of quasiparticles near the defect. This is turn can lead to a different sensitivity of the conductance to the motion of the TLS seen as a "fluctuator amplitude" fingerprint as a function of strain. Similar fluctuations in TLS signals have been observed as a function of magnetic field [Zimmerman et al.]. All of our defect experiments took place at regions of magnetic field that maximized the change in conductance due to the motion of the TLS. Figures 6.12a and 6.12b show the defect fingerprints for defects B and C. For large positive strains, the signal from defect B became indistinguishable from the background noise. The variation of defect signals as a function of strain is very similar in both cases: a few Ohms over the range of applied strain. Defect C, however, had a far larger signal than B, and we were able to measure it

over our entire range of strain. This is due in part to the smaller linewidths in samples 2-4, which were 70 nm as opposed to 100 nm for sample 1, and in part to coincidence.

III C. Tunneling Rates

We will now discuss the change in the total tunneling rates that we see as a function of strain in Figures 6.6-.11c. The expectation from the tunneling model is that the dominant coupling of a TLS to a strain field is diagonal in the representation of well occupation; that is, that the effect of strain is to change the energy asymmetry of the two wells. It is natural to ask, then, whether such a change in ε would affect the total tunneling rate. We certainly see, most obviously in the case of defect C (Figure 6.8c) that the tunneling rate varies systematically with strain, increasing when strain and asymmetry increase. We wish to estimate the deformation potential for Δ_0, the off-diagonal element of the TLS Hamiltonian (Equation 2.2). Consider the expression for Δ_0 in the 1-D WKB approximation. Recall (Equation 2.3) that we have

$$\Delta_0 = \omega_0 \, e^{-d\sqrt{\frac{2mV}{\hbar^2}}} \equiv e^{-\lambda}, \tag{6.6}$$

where ω_0 is the vibrational frequency in a well, d is the separation between the wells, and m and V are the mass of the tunneling particle and the height of the potential barrier. This bare tunneling matrix element is renormalized due to interactions with conduction electrons and phonons, following the theory of dissipative quantum tunneling (Equation 2.30). The result is tunneling matrix element is renormalized by interactons between the TLS and quasiparticles (Equation 2.30). Recall that the total transition rate for a TLS (Equation 2.32) is

$$\Gamma_{total} = \frac{\Delta_r}{2}\left(\frac{2\pi kT}{\hbar\Delta_r}\right)^{2\alpha-1}\frac{\cosh(\varepsilon/2kT)}{\Gamma(2\alpha)}\left|\Gamma\left(\alpha+i\frac{\varepsilon}{2\pi kT}\right)\right|^2 \tag{6.7}$$

in the limit of incoherent tunneling, that is $\hbar\Delta_r \ll kT$. This functional form in this limit has been found to be in excellent agreement with defect data [Golding, Zimmerman, and Coppersmith] [Chun and Birge, 1993].

The tunneling parameters we find for defect C are, at zero strain, $\varepsilon = 1.4$ eV and $\Gamma_{total} = 0.19$ sec^{-1}. The measurement temperature was 1.3 K, and we estimate α, which must lie between 0 and 1/2 in at least crystalline metals [Yamada et al.], as 0.25. Some examples of experimental values of α are 0.24 [Golding et al., 1992] and 0.195 [Chun and Birge, 1993]. We can now proceed with a rough calculation of Δ_0. We find a value of $1.08*10^3$ s^{-1} for the renormalized matrix element that gives a total rate of 0.19 s^{-1}. This corresponds to $\Delta_0 = 2.35*10^5$ s^{-1}. Here we have used a cutoff frequency for conduction electron interactions of $\omega_0 = 2.5*10^{12}$ s [Cukier et al.]. With an estimated mass of $2*m_{Bi}$ for the tunneling particle and a separation of 0.1 nm, we find a value for V of $2.07*10^{-22}$ J, corresponding to a thermal energy of 15 K. These represent one plausible set of parameters, but by no means the only one that describes the observed tunneling rate.

In the limit of a very asymmetric TLS, the total tunneling rate is dominated by the fast transition rate. We could expect, then, that an increase in the asymmetry would effectively reduce the barrier height for transitions from the high energy state to the low one. Naively, we might expect the potential barrier to vary proportional to ε, at most as $V_{effective} = V_0 - \varepsilon/2$. This situation is shown schematically in Figure 6.13. As a function of strain, we can write this as

$$V(\sigma) = V(0) - \frac{(\varepsilon(\sigma) - \varepsilon(0))}{2}.$$

(6.8)

Then

$$\frac{dV}{d\sigma} = -\frac{1}{2}\frac{d\varepsilon}{d\sigma},$$

(6.9)

and we can calculate the effect on the tunneling matrix element due to the change in asymmetry as a function of strain. Recall that ε is 1.4 K at zero strain, or $1.9*10^{-23}$ J. The changes in V due to $\varepsilon(\sigma)$ are then much less than the value at zero strain.

$$\frac{d\hbar\Delta_0}{d\sigma} = -\frac{d\hbar\Delta_0}{dV} \cdot \frac{dV}{d\sigma} = \frac{\hbar\Delta_0(0)}{V(0)} \cdot \lambda \cdot \frac{d\varepsilon}{d\sigma},$$

(6.10)

recalling that $\lambda \equiv d\sqrt{\frac{2mV}{\hbar^2}}$. λ is approximately 16 for this defect, so

$\frac{d\hbar\Delta_0}{d\sigma} = 1.2 \cdot 10^{-24} J = 7.5 \cdot 10^{-6} eV$. This implies a large relative change in $\hbar\Delta_0$ over the scale of experimentally applied strains of roughly $+/-10^{-5}$; the value of $\hbar\Delta_0$ at zero strain was $2.5*10^{-29}$ J or $1.6*10^{-10}$ eV. The deformation potential for the tunneling matrix element is, $7.5*10^{-6}$ eV, more than 5 orders of magnitude less than the deformation potential for asymmetry. The large relative change in $\hbar\Delta_0$ occurs because this experiment can only sample TLS with small tunneling matrix elements. Our experimental bandwidth, roughly 50 Hz, dictates that defects with low tunneling rates are observed. Recall that the incoherent tunneling regime requires that $\hbar\Delta_r \ll kT$, and in order for the dynamics to be dominated by tunneling, $kT \ll V$. This leads to the very small value of $\hbar\Delta_0/V$ that we see above in the expression for the off-diagonal response of the TLS Hamiltonian to strain. In Figure 6.14, we see a plot of the tunneling rate as a function of

strain for the estimated parameters describing defect C as the solid line. It describes the observed rates, also plotted, remarkably well. I reiterate that these are not the only consistent set of parameters (α, ω_c, m, and d) that produce such agreement. The point of the figure is to show that physically reasonable parameters can describe the observations and produce consistent tests of the relative energy scales defining the model of defect dynamics as a TLS in the dissipative regime.

IV.   Conclusion

In conclusion, we report direct measurements of the dynamics of single defects in bismuth films as a function of applied strain. The model of a TLS in a dissipative environment is consistent with the observed changes in both the asymmetries and total tunneling rates. The deformation potential for ε is shown to vary from defect to defect, with minimum and maximum magnitudes of 0.1 eV and 1.7 eV and random signs.
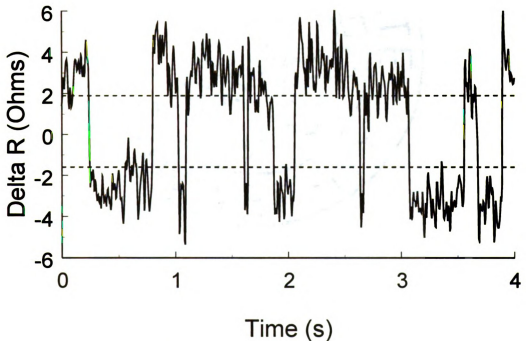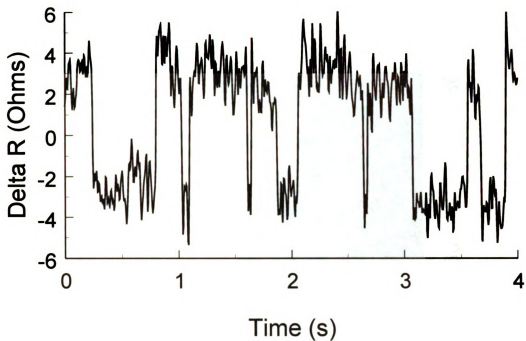
Figure 6.1 Example of Raw Data and Comparator Analysis Method

In the top of the Figure, we see a four second time trace for a sample with a single fluctuator present. With careful placement of Schmidt triggers in the analysis program, we can divide the data unambiguously into "up" and "down" states.
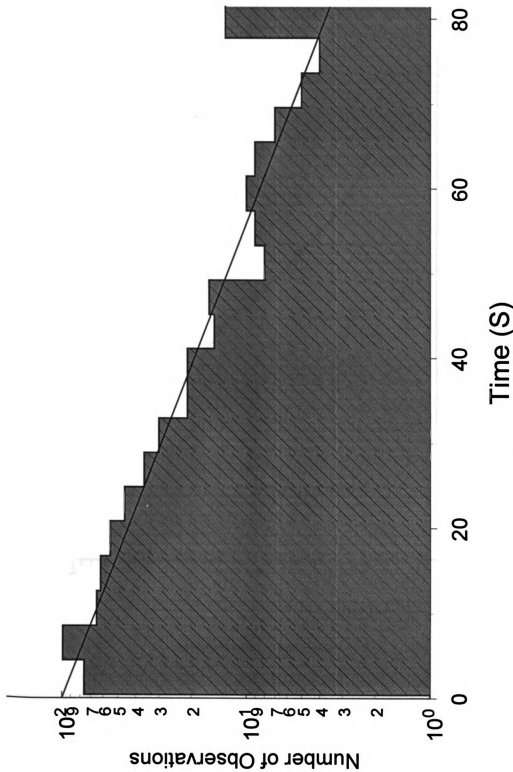
Figure 6.2 Histogram of Dwell Times For a Mobile Defect

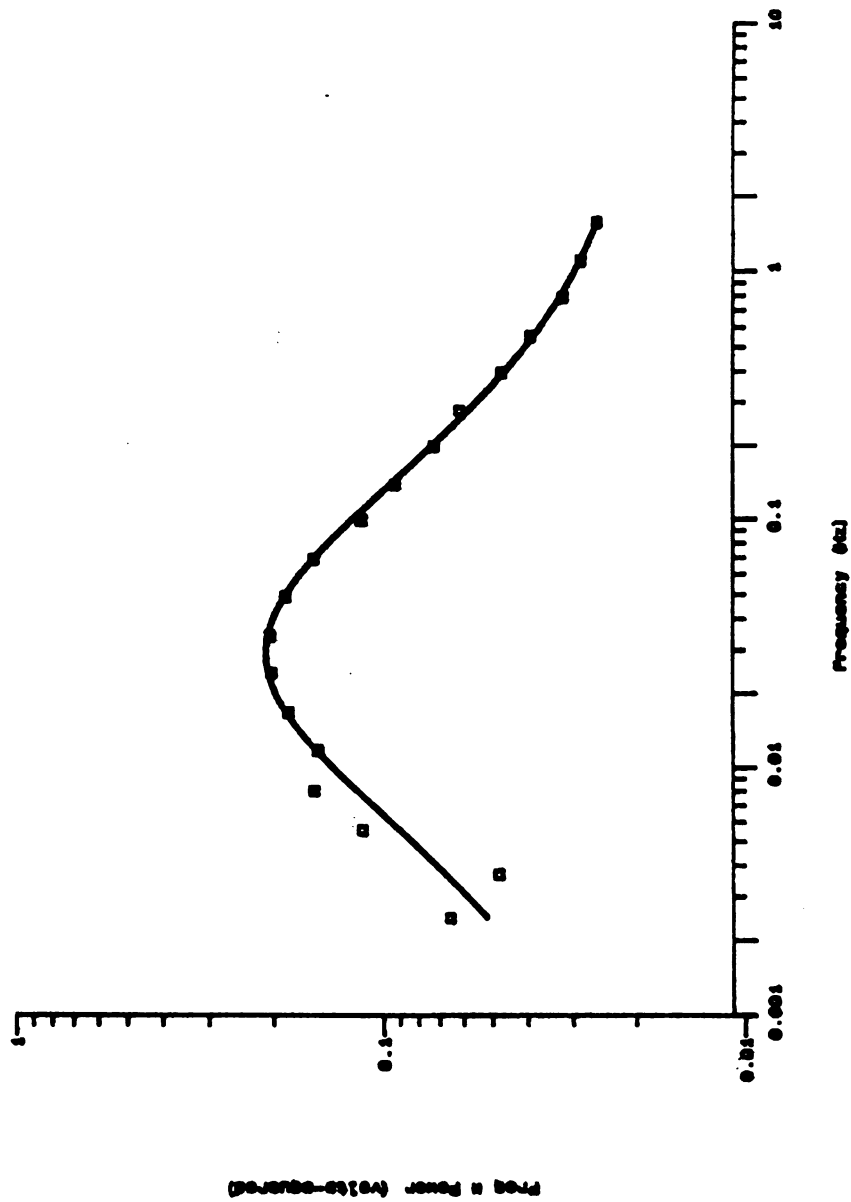The line corresponds to the best fit to an exponential distribution of dwell times, $P(\tau) = N_{tot} e^{-\tau/<\tau>}$.

Figure 6.3 Fit of f*S(f) for the Debye-Lorentzian Power Spectrum of a Switching Defect. The frequency of the peak in f*S(F) is given by $f = 2\pi/\tau$, where τ is the total defect relaxation rate.
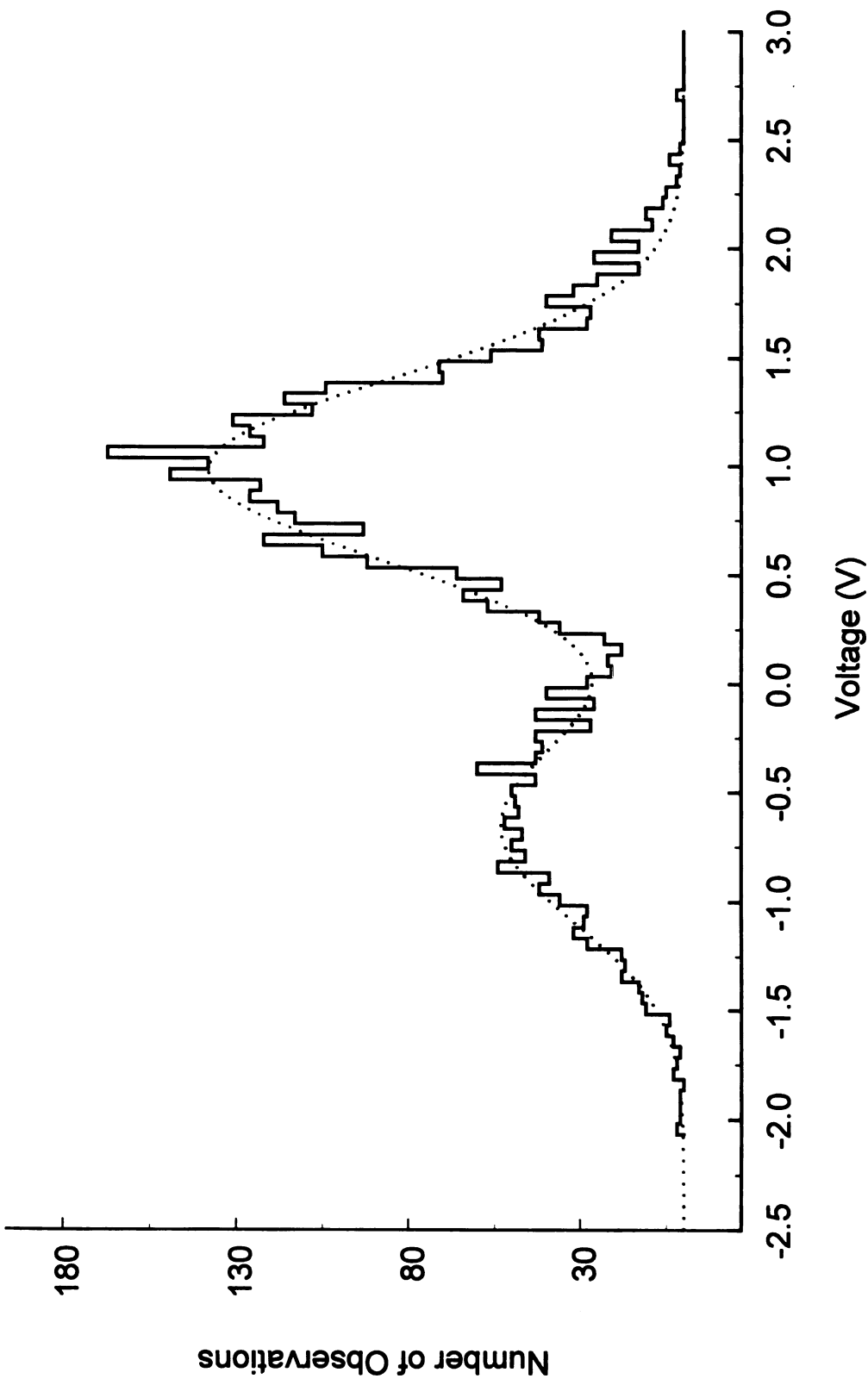
Figure 6.4 Histogram of Voltage for Defect Data

The dotted line corresponds to a fit corresponding to two Guassians with equal widths.

93
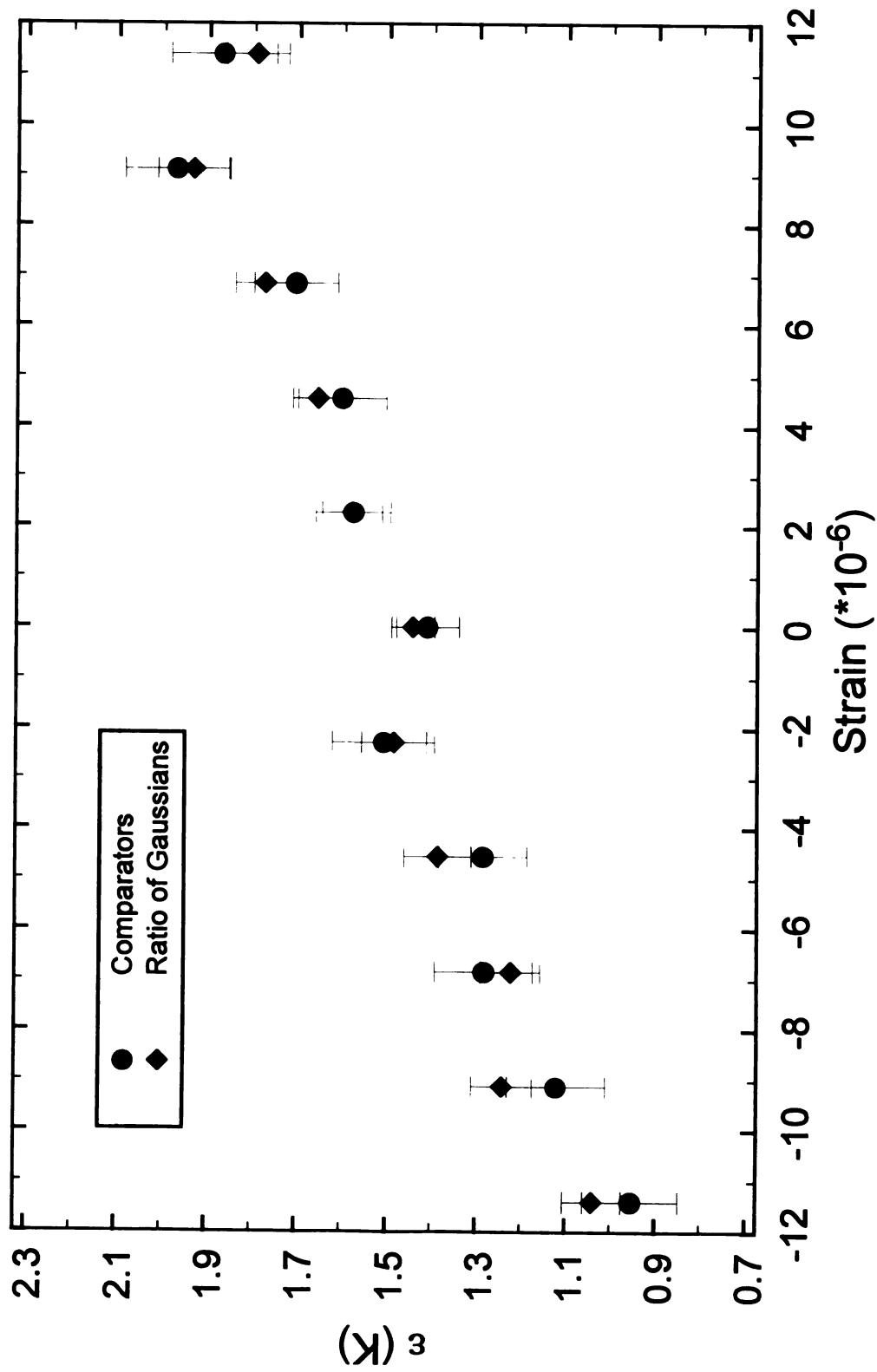
Figure 6.5 Comparison of ε Determined by Both Methods of Data Reduction
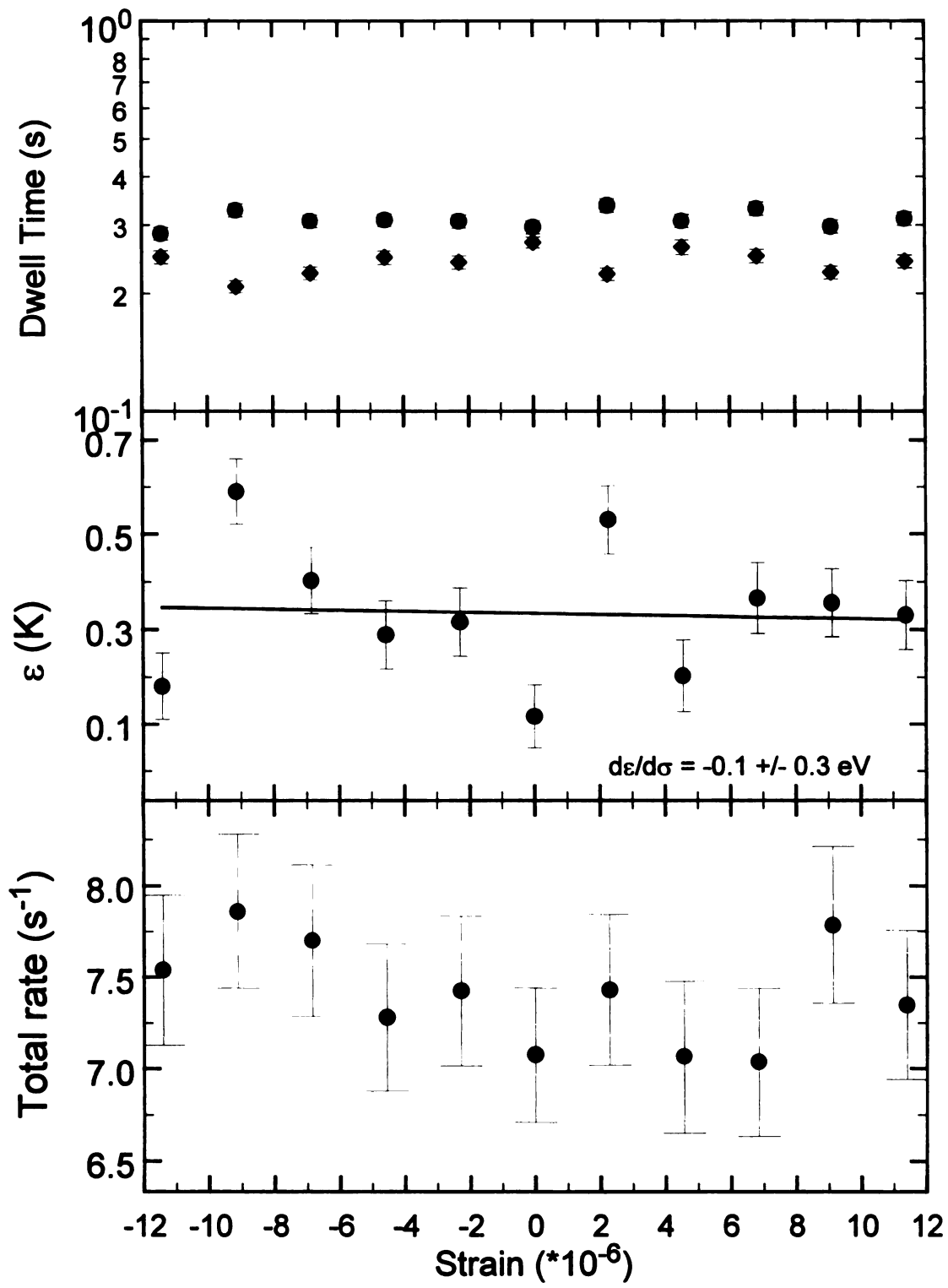
The Figure shows data for defect C.
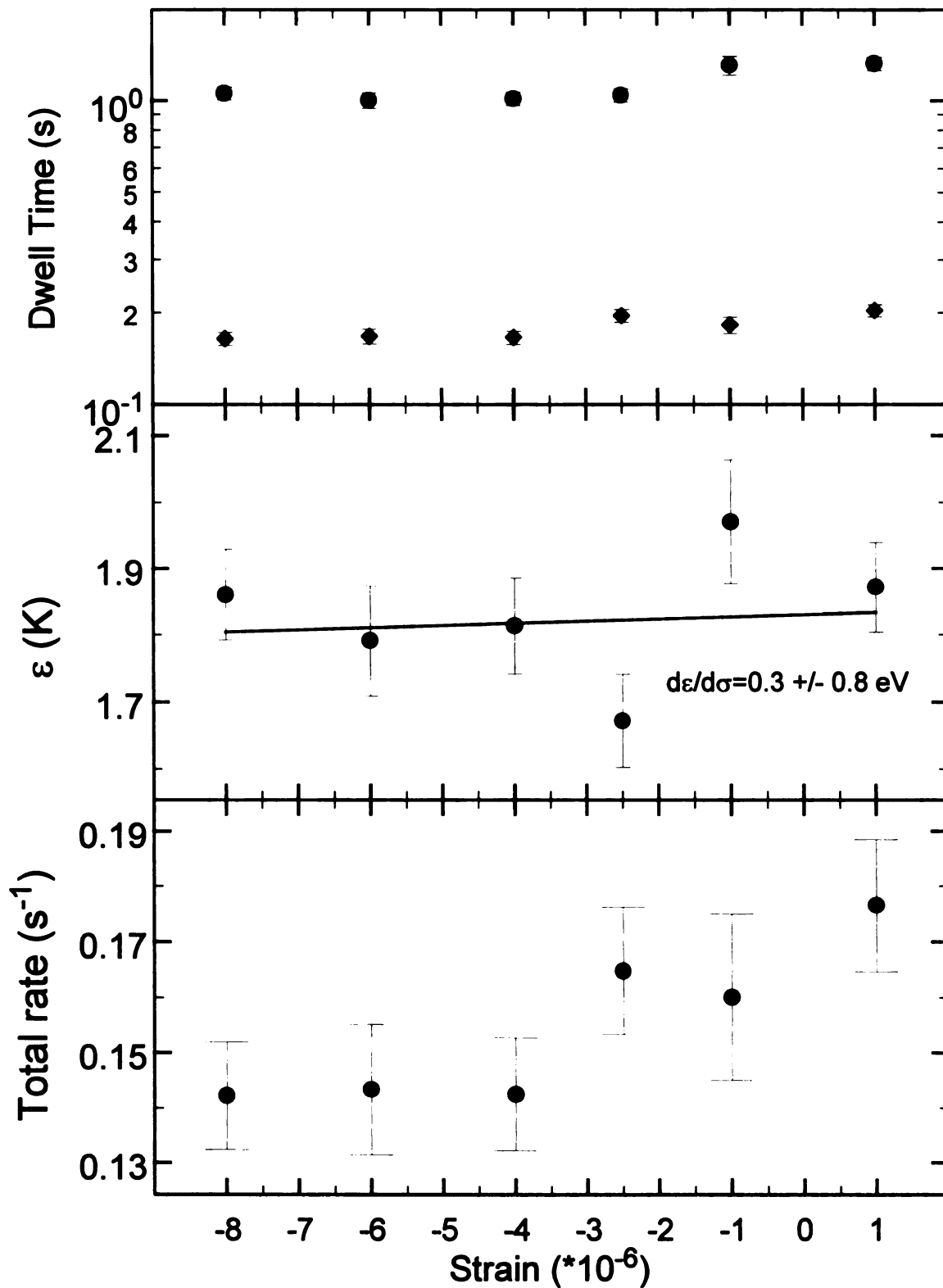
Figures 6.6 a-c Dwell Times, Energy Asymmetry, and Total Tunneling Rate for
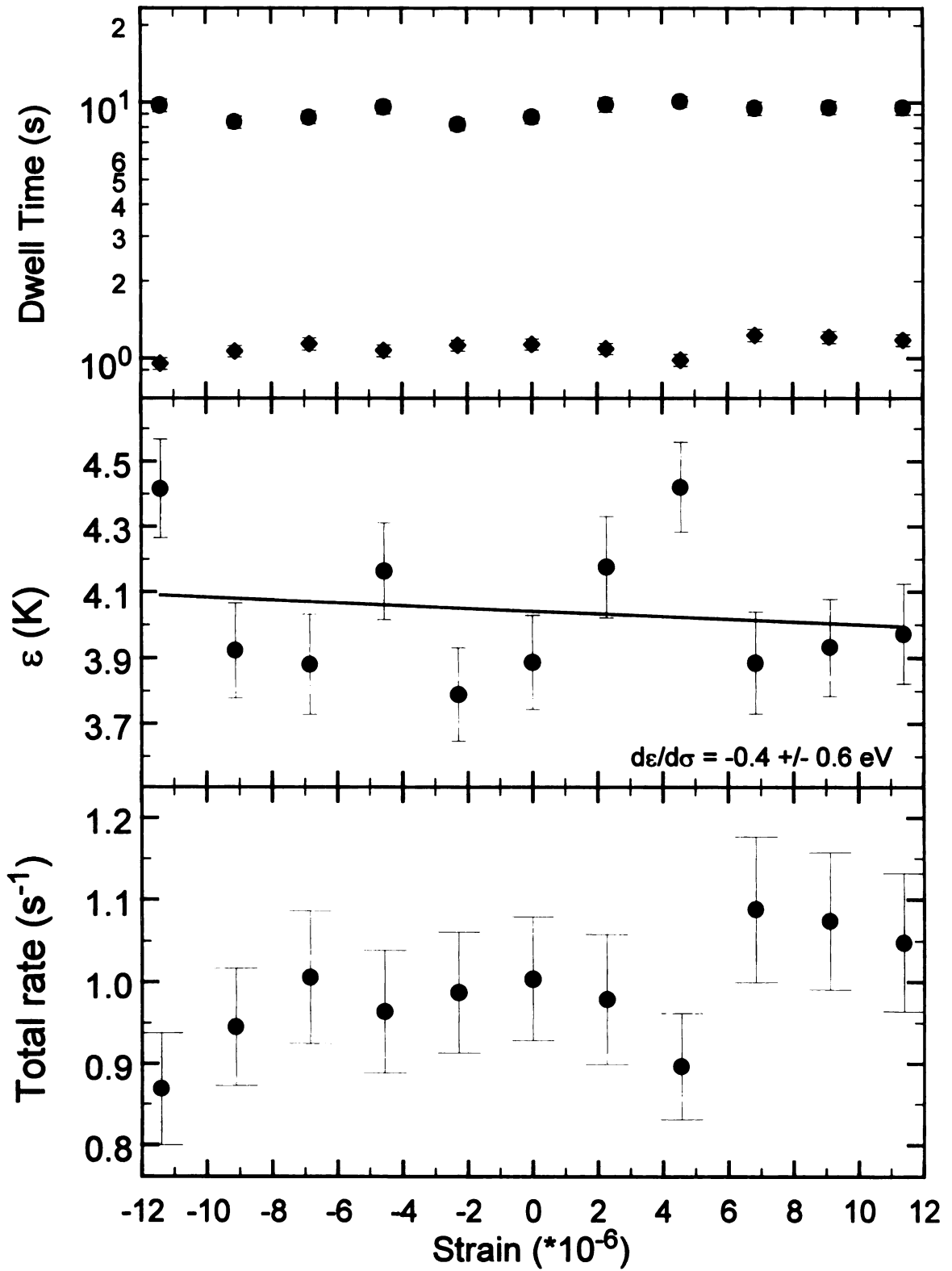a Single Defect: Defect A at T=1 K
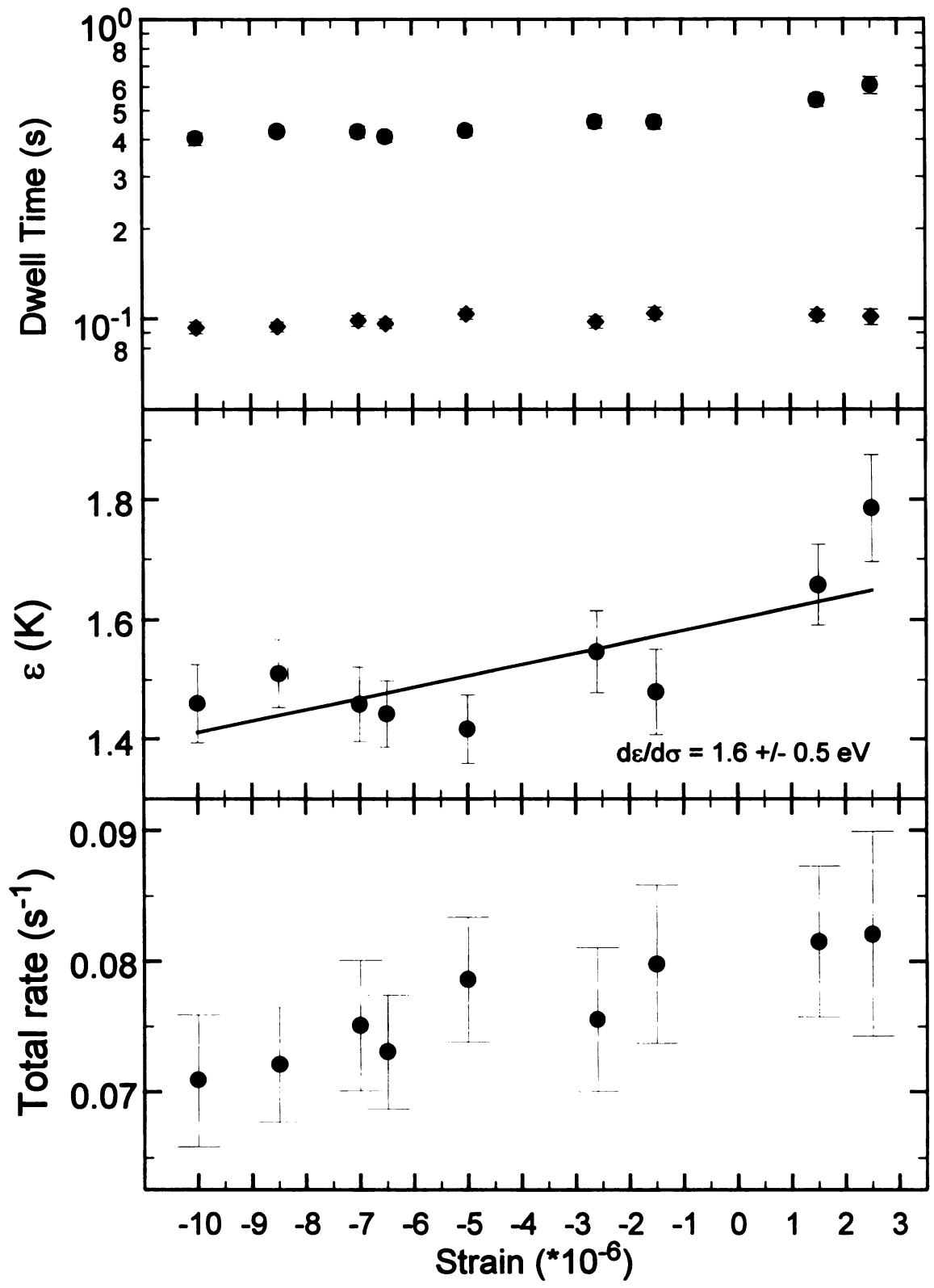
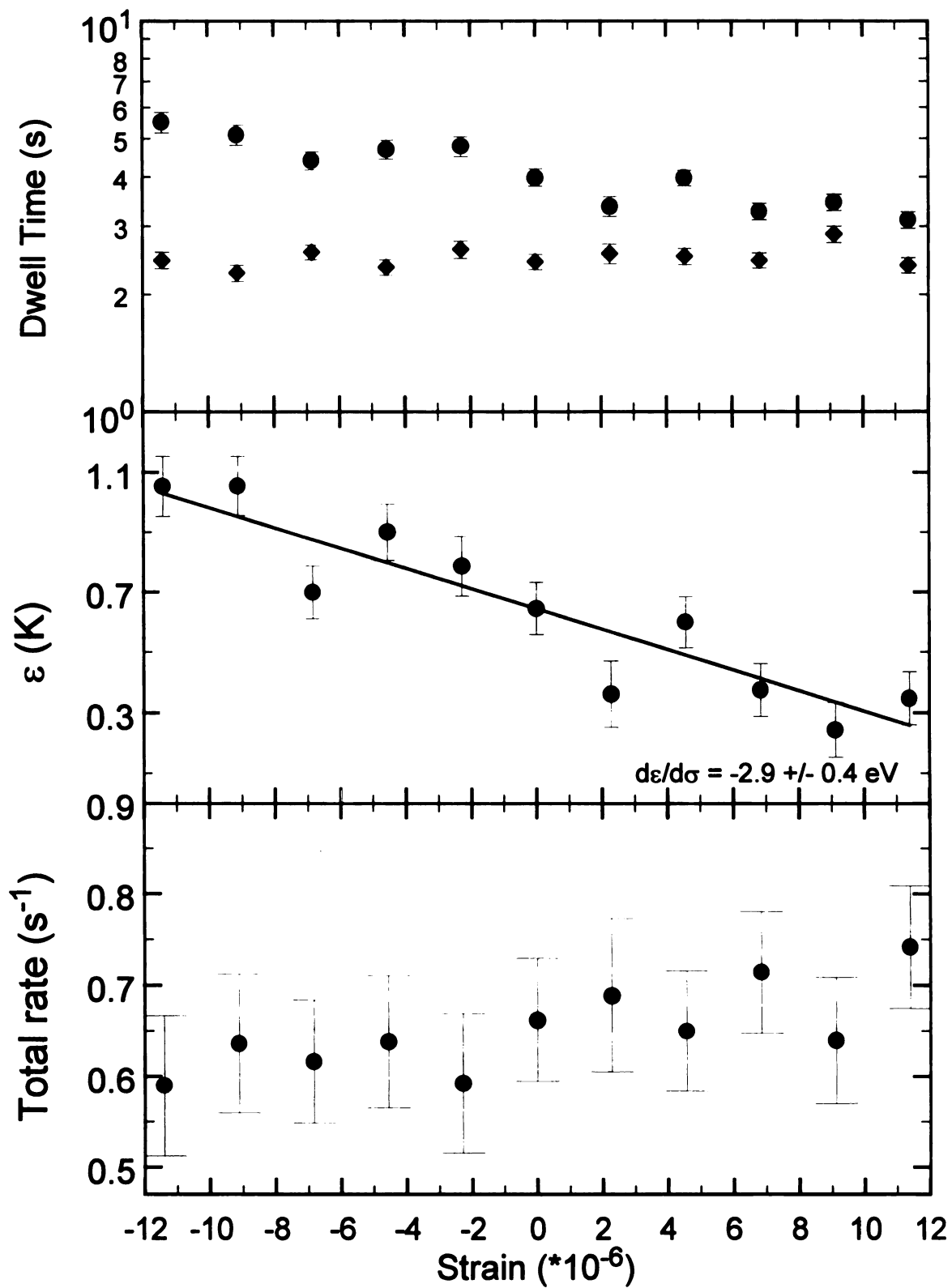Figures 6.7 a-c Dwell Times, Energy Asymmetry, and Total Tunneling Rate for a Single Defect: Defect B at T=1 K
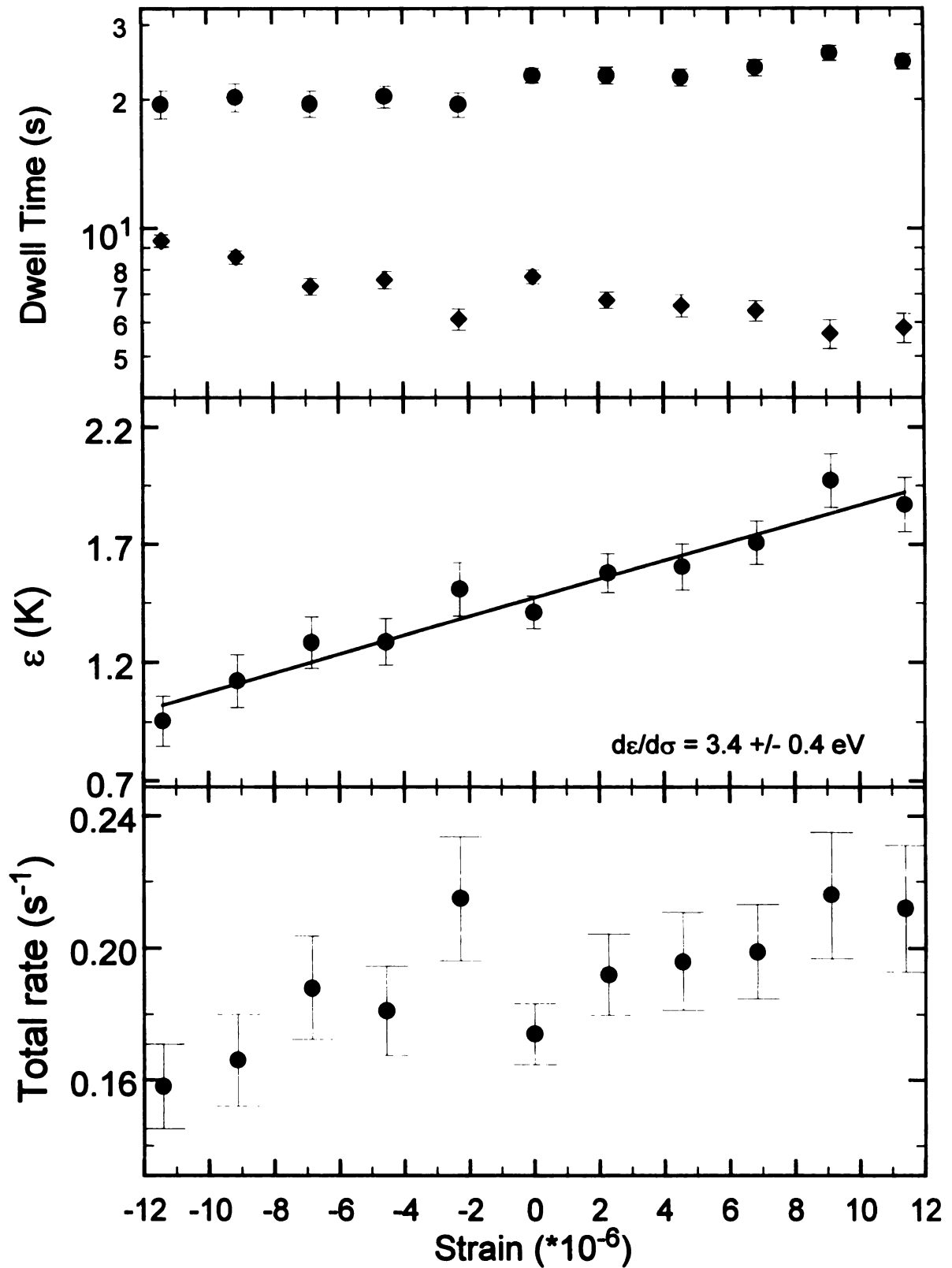
Figures 6.8 a-c Dwell Times, Energy Asymmetry, and Total Tunneling Rate for a
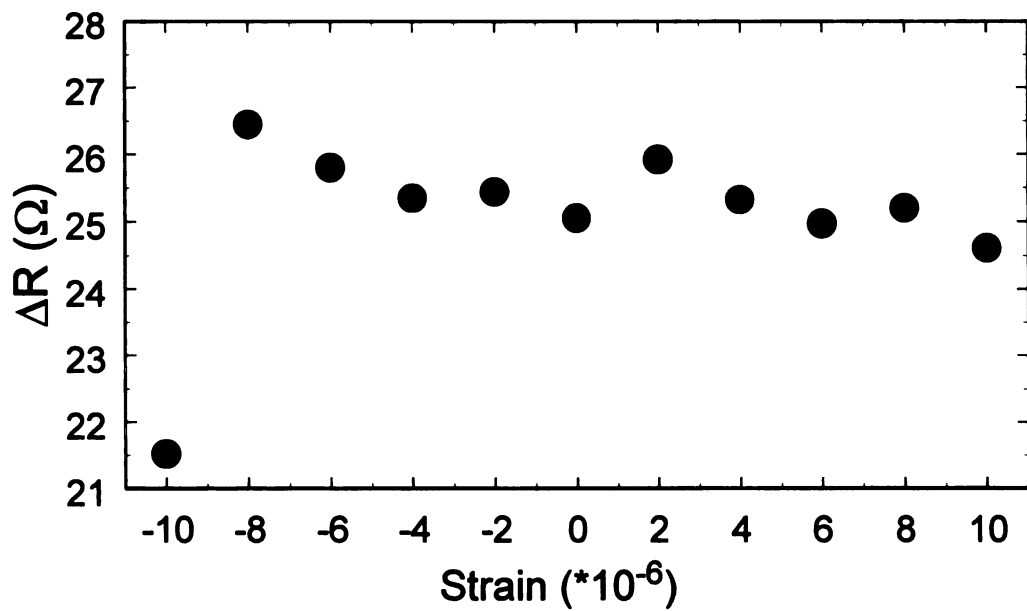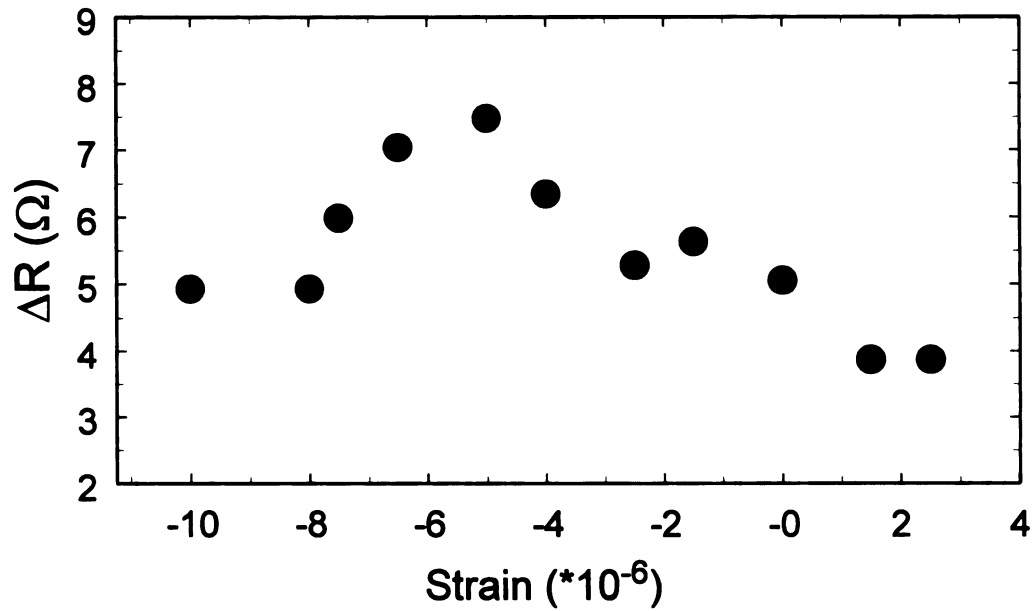Single Defect: Defect C at T=1.3K

97

Figures 6.9 a-c Dwell Times, Energy Asymmetry, and Total Tunneling Rate for a
Single Defect: Defect D at T=1.3K

Figures 6.10 a-c Dwell Times, Energy Asymmetry, and Total Tunneling Rate for a
Single Defect: Defect E at T=1.9K

Figures 6.11 a-c Dwell Times, Energy Asymmetry, and Total Tunneling Rate for a Single Defect: Defect F at T=1.3K

Figures 6.12 a and b Resistance Jumps as a Function of Strain

In the top Figure (a), we see the resistance jump due to the motion of defect B as a function of applied strain. For strains larger than 2.5 * 10^{-6}, the jump was not clearly resolvable from the backgound noise. Below (b) we see the jumps vs. strain for defect C.
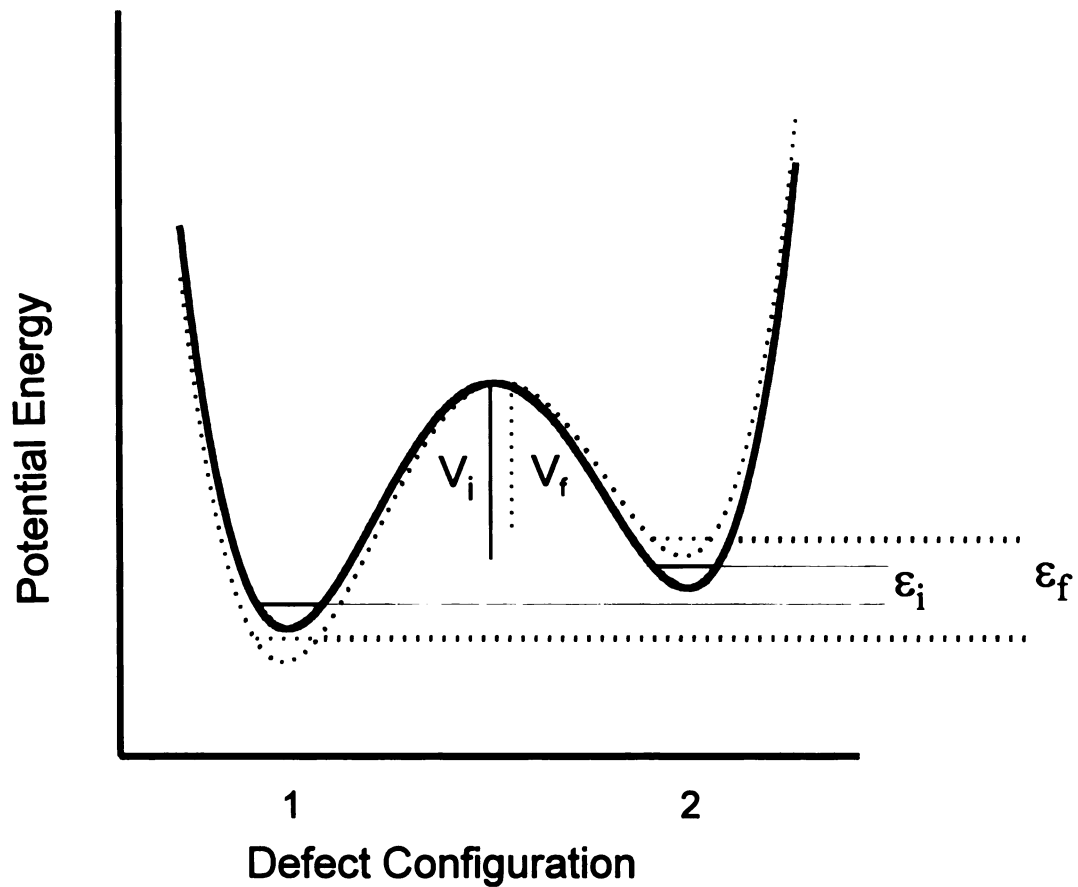
Figure 6.13 Response of a TLS to Strain

The solid lines refer to the potential before the strain is applied, and the dotted lines refer to that after the asymmetry has changed, perhaps due to an applied strain. The effective tunneling matrix element increases because the high energy state now experiences a smaller energy barrier.
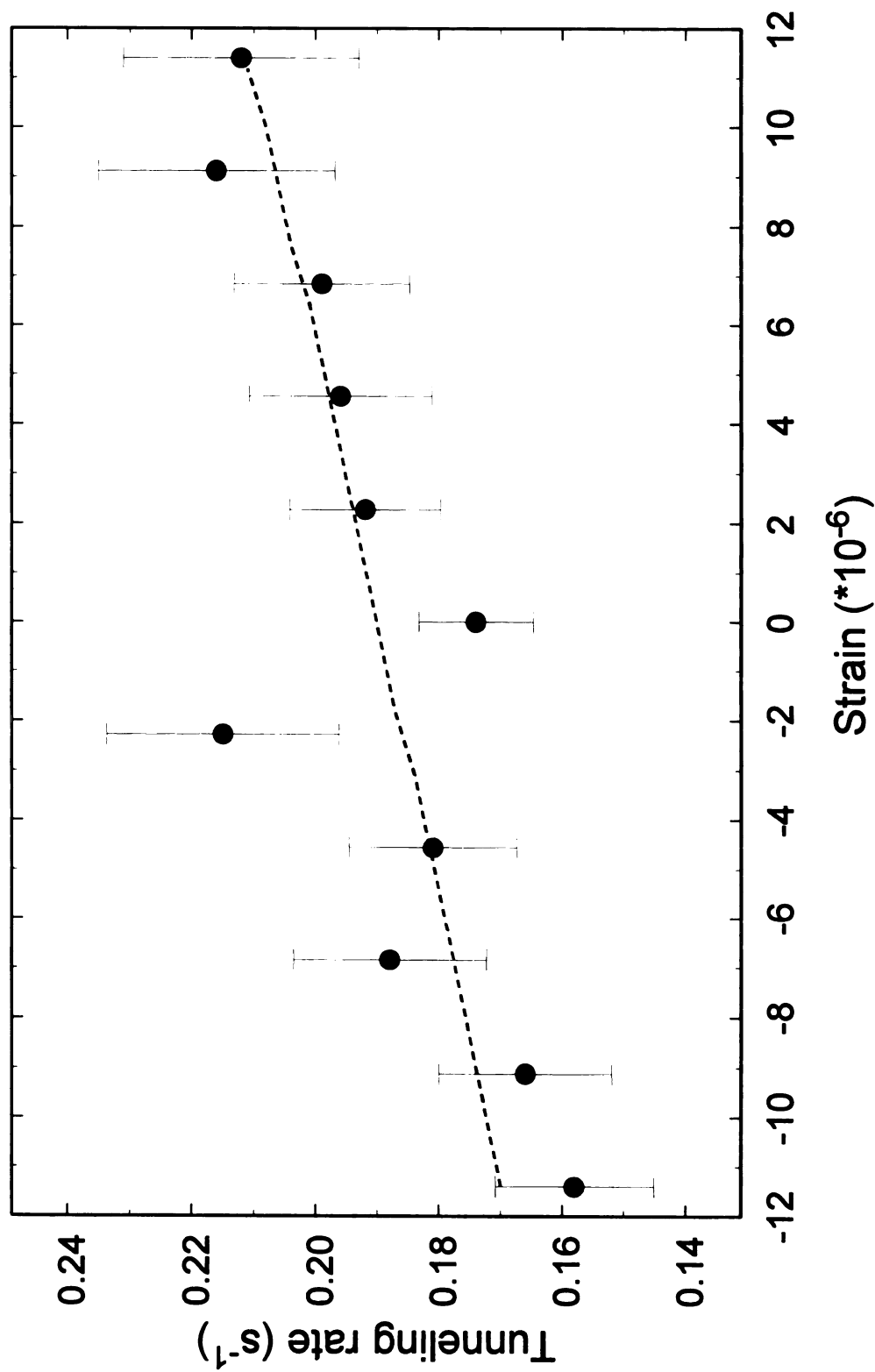
Figure 6.14 Variation of Tunneling Rate With Strain

Total tunneling rate data for Defect C is plotted as a function of strain. The dashed line represents the results of a calculation for the variation of tunneling rate induced by changes in the potential barrier of order $d\varepsilon/d\sigma$.

Chapter 7

Summary and Conclusions

We have seen that the introduction of mechanical strain to mesoscopic, metallic

samples produces interesting phenomena. The conductance of a bismuth wire with

dimensions that are comparable to the phase-breaking length for conduction electrons

varies as a function of applied strain. The average amplitude of the variance of these

aperiodic, random fluctuations is the same as that of the Universal Conductance

Fluctuations seen as a function of magnetic field in the same sample, of order e^2/h. A

consistent description of this "strain fingerprint" follows from the deformation potential

of the Fermi energy in bismuth, which is several eV. According to UCF theory, changes

in the Fermi as small as E_c (equation 3.7) can alter the sample's conductance by up to

e^2/h. Our observations show that at 29 mK, strains as small as $4*10^{-7}$ satisfy this

condition.

The tunneling model of amorphous solids describes a set of excitations

fundamental to the disordered state. The low-temperature thermal and acoustic properties

of glasses are dramatically influenced by the dynamics of these two-level tunneling

systems, but fairly little can be determined about the microscopic identity of the tunneling

agents by studying them with bulk measurements in insulators. One microscopic

parameter of particular interest is the response of the potential of a TLS to strain, realized

in the Tunneling Model as a change in the asymmetry of the two energy levels. The ensemble average of this deformation potential is large, as is evidenced by the strength of phonon relaxation caused by the TLS's in glasses. Here I have reported the first measurement of the response of individual TLS's to strain. I have studied the dynamics of mobile defects in polycrystalline bismuth, observed through fluctuations in their conductance caused by TLS motion. From the ratio of the tunneling rates we recover the energy asymmetry and measure it as a function of strain. I report deformation potentials that vary from 0 to 1.7 eV for six different TLS's. The tunneling matrix element also varies with strain, in a manner that is microscopically plausible. This variation is seen as a change in total tunneling rate as a function of strain, or perhaps more accurately, as a function of ε. I have shown that mechanical strain is a useful tool to probe the microscopic world of an atomic-scale TLS.

APPENDIX

Appendix

Strain Calibration

As described in the text, we chose to fabricate samples on a thin substrate that was then mounted atop the PZT-5A wafer, which produced the desired mechanical strain. The joint between the substrate and the PZT was formed from a thin layer of Apiezon N-grease. The grease has a very convenient viscosity at room temperature, making sample mounting and alignment simple. At low temperature, we expected the grease joint to become extremely rigid. It was necessary to test this hypothesis, however, and calibrate for strain losses due to the grease and the substrate, since these nominally .005"-thick substrates were not substantially thinner than our 20 mil wafers of PZT.

We used commercial K-alloy strain gauges manufactured by Measurements Group, Inc to measure the strain produced by the PZT wafers. These strain gauges are composed of meander-pattern metal film wires that change resistance when a strain is applied. This occurs because the length of the wire and its cross-sectional area (due to Poisson's ratio) change under strain. The response of the gauge to strain is specified by the manufacturer's quoted gauge factor,

$$G_f = \frac{\Delta R / R}{\Delta L / L}.$$ (A.1)

One advantage of this particular alloy is that the thermal response of the gauge factor is only -0.8 % / 100 ° C.

The calibration consisted of two steps. In the first, we glued a strain gauge directly onto a PZT-5A wafer, in order to measure its response as a function of temperature. We find a low-temperature response of d_{31} for the wafer as $33*10^{-12}$ m/V. The room temperature value we found was $250*10^{-12}$ m/V. Recall that d_{31} is the strain induced in the plane perpendicular to the applied voltage. A previous study showed that we could expect reduction in the strain produced at a given voltage from room temperature to 4.2 K of roughly a factor of 5 [Fein, et al.] [Vandervoort, et al.]. We found that our PZT response was decreased by a factor of 7.7 upon cooling from 295 K to 4.2 K. This result could differ from the previous studies in part because there the PZT was formed as a tube for use in an STM, where we use a thin wafer.

Once we had determined the low-temperature response of the bare PZT, we could determine the losses associated with the grease and substrate. The substrates reduced strain by approximately 20%, and the grease layer produced a reduction of another 6%. We glued strain gauges onto both glass and silicon substrates and measured the strain once again. Figure A.1 shows part of the calibration at 1.6 K for the silicon substrate. There we see a strain response of $1.15 * 10^{-7}$ V^{-1}. At temperatures near 1 K, we found that the strain induced in our samples on the glass substrates was reduced to 10^{-7} V^{-1}, and those on the silicon substrates experienced strains of $1.15*10^{-7}$ V^{-1}.
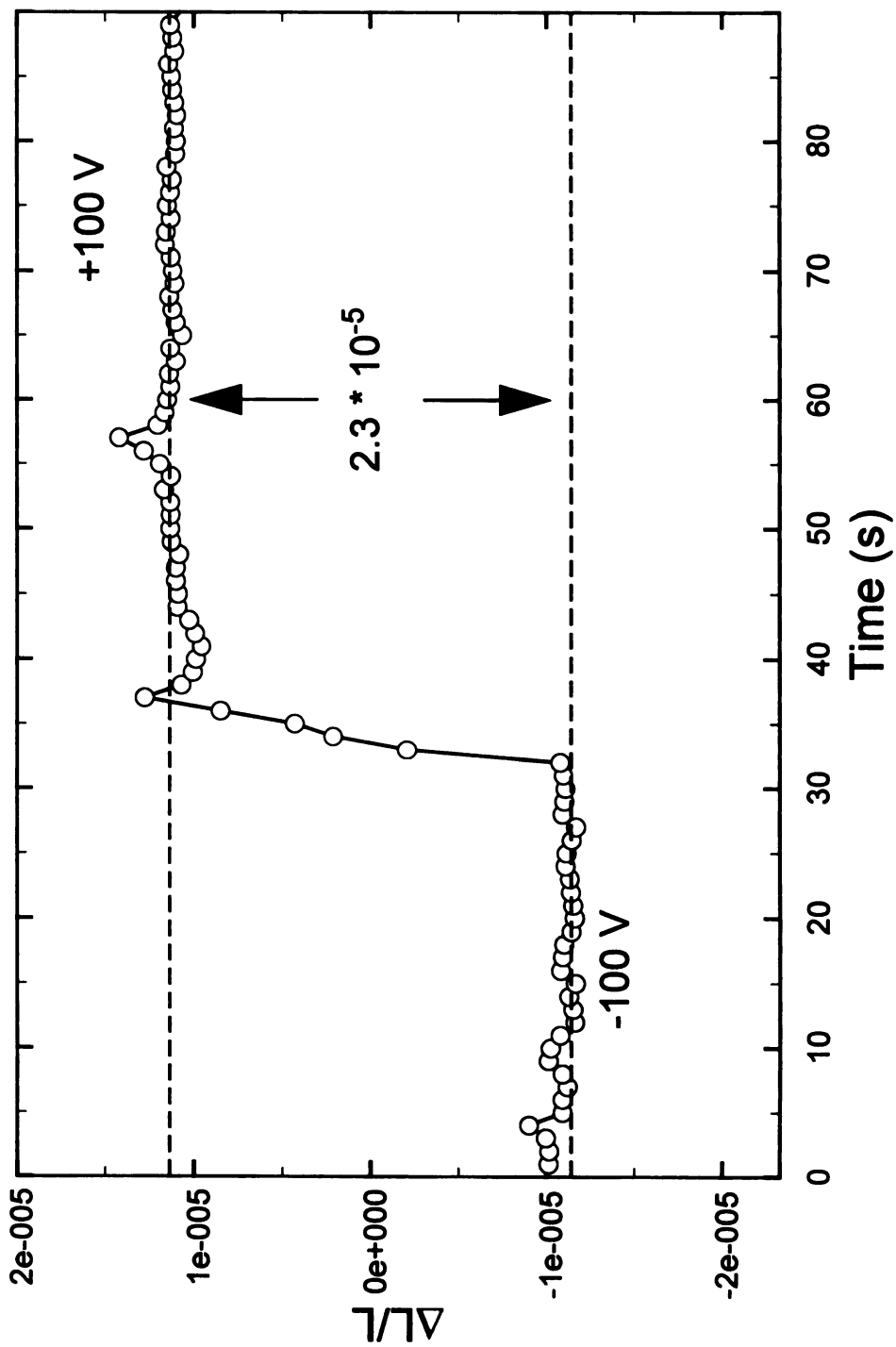
Figure A.1 Strain Calibration for 5 mil Silicon at 1.6 K
In this Figure, we see an example of data from a commercial strain gauge, converted to dimensionless untis of strain.
The gauge was glued to a 5 mil silicon wafer, which was then attached with Apiezon N-grease onto the PZT-5A.
The response seen corresponds to a strain of $1.15 * 10^{-7}/V$ when a potential is applied to the PZT-5A wafer's electrodes.

BIBLIOGRAPHY

Bibliography

Abrahams, E., P.W. Anderson, P.A. Lee, and T.V. Ramakrishnan, Phys. Rev. B **24**, 6783 (1981).

Allen, L. and J.H. Eberly, *Optical Resonance of Two-Level Atoms*, New York : Wiley, 1975.

Al'tshuler, B.L., Pis'ma Zh. Eksp. Teor. Fiz. **41**, 530, (1985), [JETP Lett. **41**, 648 (1985)].

Al'tshuler, B.L., A.G. Aronov, M.E. Gershenson, and Yu.V. Sharvin, Sov. Sci. Rev. A. Phys. **9**, 223 (1987).

Al'tshuler, B.L., A.G. Aronov, and D.E. Khmel'nitskii, Solid State Comm. **39**, 619 (1981), J. Phys. C., **15**, 7367 (1982).

Al'tshuler, B.L. and D.E. Khmel'nitskii, Pis'ma Zh. Eksp. Teor. Fiz. **42**, 291 (1985), [JETP Lett. **42**, 359 (1985)].

Al'tshuler, B.L., D.E. Khmel'nitskii, A.I. Larkin, and P.A. Lee, Phys. Rev. B **22**, 5142 (1980).

Al'tshuler, B.L., P.A. Lee, and R.A. Webb, eds., *Mesoscopic Phenomena in Solids*, New York : North-Holland, 1991.

Al'tshuler, B.L. and B.I. Shklovskii, Zh. Eksp. Teor. Fiz. **91**, 220 (1986) [Sov. Phys. JETP **64**, 127 (1986)].

Al'tshuler, B.L. and B.Z. Spivak, Pis'ma Zh. Eksp. Teor. Fiz. **42**, 363 (1985), [JETP Lett. **42**, 477 (1985)].

Anderson, A.C., W. Reese, and J.C. Wheatley, Rev. Sci. Instrum. **34**, 1386 (1963).

Anderson, P.W., Phys. Rev. **109**, 1492 (1958).

Anderson, P.W. and P.A. Lee, Prog. Theor. Phys. Suppl. **69**, 212 (1980).

Anderson, P.W., B. I. Halperin, and C. M. Varma, Philos. Mag. **25**, 1 (1972).

Arnold, W., S. Hunklinger, S. Stein and K. Dransfield, J. Noncrys. Solids **14**, 192-200 and references therein (1974).

Ashcroft, N.W. and N. D. Mermin, *Solid State Physics*, New York : Sanders College Publishing, 1976.

Beenakker, C.W.J., Phys. Rev. Lett. **70**, 1155 (1993); Phys. Rev. B **47**, 15763 (1995).

Bergmann, G., Phys. Rep. **107**, 1 (1984).

Bergmann, G., Phys. Rev. Lett. **43**, 1357 (1979).

Bergmann, G., Phys. Rev. Lett. **48**, 1046 (1982).

Bergmann, G., Solid State Comm. **42**, 815 (1982).

Berret, J.F. and M. Meißner, Z. Phys. B **70**, 65 (1988).

Beutler, D.E., T.L. Meisenheimer, and N. Giordano, Phys. Rev. B **58**, 1240 (1987).

Birge, N.O., B. Golding, and W.H. Haemmerle, Phys. Rev. Lett. **62**, 195 (1989).

Birge, N.O., J.S. Moon, and D. Hoadley, Czech. J. of Phys. **46**, (1996) Supplement S4 - Proceedings of the 21st Conf. on Low Temp. Phys.

Black, J.L., Phys. Rev. B **17**, 2740 (1978).

Broers, A.N., J.M.E. Harper, and W.W. Molzer, Appl. Phys. Lett. **33**, 392 (1978).

Büttiker, M., Phys. Rev. Lett. **57**, 1761 (1986).

Caldiera, A.O. and A.J. Leggett, Ann. Phys. **149**, 374 (1983).

Chakravarty, S. and A.J. Leggett, Phys. Rev. Lett. **52**, 5 (1984).

Chandrasekhar, V., M.J. Rooks, S. Wind, and D.E. Prober, Phys. Rev. Lett. **55**, 1610 (1985).

Chun, K., "Dissipative Quantum Tunneling of a Single Defect in a Submicron Bi Wire Below 1K", Ph.D. dissertation, Michigan State University (1993).

Chun, K., and N.O. Birge, Phys. Rev. B **49**, 2959 (1994), Phys. Rev. B **48**, 11 500 (1993).

Clawson, C.W., K.M. Crowe, S.E. Kohn, S.S Rosenblum, C.Y. Huang, J.L. Smith, and J.H. Brewer, Phsyica B & C **110**, 2164 (1982).

Cukier, R.I., M. Morillo, K. Chun, and N.O. Birge, Phys. Rev. B **51**, 13 767 (1995).

Dolan, G.J., and D.D. Osheroff, Phys. Rev. Lett. **43**, 721 (1979).

Dutta, P., P. Dimon, and P.M. Horn, Phys. Rev. Lett. **43**, 646 (1979).

Dutta, P. and P.M. Horn, Rev. Mod. Phys. **53**, 497 (1981).

Dyson, F.J., J. Math Phys **3**, 140 (1962); **3**, 157 (1962); **3**, 166 (1962).

Dyson, F.J., and M.L. Mehta, J. Math, Phys. **4**, 701 (1963).

Fein, A.P., J.R. Kirtley, and R.M. Feenstra, Rev. Sci. Instrum. **58**, 1806 (1987).

Feng, S., P.A. Lee, and A.D. Stone, Phys. Rev. Lett. **56**, 1960 (1986).

Fisher, M.P.A. and A.T. Dorsey, Phys. Rev. Lett. **54**, 1609 (1985).

Fukuyama, H., and E. Abrahams, Phys. Rev B **27**, 5986 (1983).

Garfunkel, G.A., G.B. Alers, and M.B. Weissman, Phys. Rev. B **41**, 4901 (1990).

Golding, B. and J.E. Graebner, Phys. Rev. Lett. **37**, 852 (1976).

Golding, B., J.E. Graebner, B.I. Halperin, and R.J. Schutz, Phys. Rev. Lett. **30**, 223 (1973).

Golding, B., J.E. Graebner, and A.B. Kane, Phys. Rev. Lett. **37**, 1428 (1976).

Golding, B., J.E. Graebner, and R.J. Schutz, Phys. Rev. B **14**, 1660, 1976).

Golding, B., N.M. Zimmerman, and S.N. Coppersmith, Phys. Rev. Lett. **68**, 998 (1992).

Grabert, H. and U. Weiss, Phys. Rev. Lett. **54**, 1605 (1985).

Graebner, J.E., and B. Golding, Phys. Rev. B **19**, 964 (1979).

Graebner, J.E., B. Golding, R.J. Schutz, F.S.L. Hsu, and H.S. Chen, Phys. Rev. Lett. **39**, 1480 (1977).

Halperin, B.I., Annals of NY Acad. of Sci. **279**, 173 (1976).

Hanson, O.P., I.F.I. Mikhail, M.Yu. Lavrenyuk, and N.Ya. Minina, J. Low Temp. Phys. **95**, 481 (1994).

Hikami, S., A.I. Larkin, and Y. Nagaoka, Prog. Theor. Phys. **63**, 707 (1980).

Hoadley, D., P. McConville, and N.O. Birge, Phys. Rev. B **60**, 5617 (1999).

Hunklinger, S., W. Arnold, and S. Stein, Phys. Lett. A **45**, 311 (1973).

Hunklinger, S., W. Arnold, S. Stein, R. Nama, and K. Dransfield, Phys. Lett. **42A**, 253 (1972).

Imry, Y., Europhysics Lett. **1**, 249 (1986).

Jäckle, J., Z. Physik **257**, 212 (1972).

Kagan, Yu., and N.V. Prokof'ev, Zh. Eksp. Teor. Fiz. **90**, 2176 (1986) [JETP **63**, 6 (1986)].

Kehr, K.W., D. Richter, J.M. Welter, O. Hartmann, E. Karlsson, L.O. Norlin, T.O. Niinikoski, and A. Yaouanc, Phys. Rev. B **26**, 567 (1982).

Kobayashi, S., F. Komori, Y. Ootuka, and W. Sasaki, J. Phys. Soc. Jpn. **49**, 1635 (1980).

Kochowski, S. and A. Opilski, Thin Solid Films **48**, 345 (1978).

Komnik, Yu. F., E.I. Bukhshtab, Yu. V. Nikitin, and V.V. Andrievskii, Zh. Eksp. Teor. Fiz. **60**, 669 (1971) [JETP **33**, 364 (1971)].

Komori, F., S. Kobayashi, and W. Sasaki, J. of the Phys. Soc. of Japan **52**, 368 (1983).

Kondo, J., Physica **124B**, 25 (1984); **125B**, 279 (1984); **126B**, 377, (1984).

Landauer, R., IBM J. Res. Dev. **1**, 223 (1957).

Lee, P.A. and A.D. Stone, Phys. Rev. Lett. **55**, 1622 (1985).

Lee, P.A., A.D. Stone, and H. Fukuyama, Phys. Rev. B **35**, 1039 (1987).

Lee, P.A. and T.V. Ramakrishnan, Rev. Mod. Phys. **57**, 287 (1985).

Leggett, A.J., S. Chakravarty, A.T.Dorsey, M.P.A. Fisher, A. Garg, and W. Zwerger, Rev. Mod. Phys. **59**, 1 (1987).

Licini, J.C., D.J. Bishop, M.P. Kastner, and J. Mengailis, Phys. Rev. Lett. **55**, 2987 (1985).

Loponen, M.T., R.C. Dynes, V. Narayanamurti, and J.P. Garno, Phys. Rev. B **25**, 4310 (1982).

Ludvikssen A., R. Kree, and A. Schmid, Phys. Rev. Lett. **52**, 950 (1984).

Maekawa, S., and H. Fukuyama, J. Phys. Soc. Jpn. **50**, 2516 (1981).

McConville, P. and N.O. Birge, Phys. Rev. B **47**, 16 667 (1993).

Meisenheimer, T.L. and N. Giordano, Phys. Rev. B **39**, 9929 (1992).

Meißner, M, and K. Spitzmann, Phys. Rev. Lett. **46**, 265 (1981).

Mohanty, P., E.M.Q. Jariwala, and R.A. Webb, Phys. Rev. Lett. **78**, 3366 (1997).

Moon, J.S., "1/f Noise and Quantum Transport in the Low Spin-orbit Scattering Limit", Ph.D. dissertation, Michigan State University (1995).

Moon, J.S., N.O. Birge, and B. Golding, Phys. Rev. B **56**, 15 124 (1997).

Mott, N.F., Adv. Phys. **16**, 49 (1967).

Muttalib, K.A., J.-L. Pichard, and A.D. Stone, Phys. Rev. Lett. **59**, 2475 (1987).

Phillips, W.A. ed., *Amorphous Solids, Low Temperature Properties*, New York : Springer-Verlag, 1981.

Phillips, W.A., J. Low Temp. Phys. **7**, 351 (1972).

Piché, L., R. Maynard, S. Hunklinger, and J. Jäckle, Phys. Rev. Lett. **32**, 1426 (1974).

Press, W.H., B.P. Flannery, S.A. Teukolsky, and W.T. Vetterling, *Numerical Recipes in C: The Art of Scientific Computing*, Cambridge : Cambridge University Press, 1988.

Pohl, R.O. and G.L. Salinger, Annals of NY Acad. of Sci. **279**, 150 (1976).

Ralls, K.S. and R.A. Buhrman, Phys. Rev. Lett. **60**, 2434 (1988), Phys. Rev. B **44**, 5800 (1991).

Ralls, K.S., D.C. Ralph, and R.A. Buhrman, Phys. Rev. B **40**, 11561 (1989).

Ralph, D.C. and R.A. Buhrman, Phys. Rev. Lett. **69**, 2118 (1992).

Sharvin, D.Y., and Ya.V. Sharvin, Pis'ma Zh. Eksp. Teor. Fiz. **34**, 285 (1981) [JETP Lett. **34**, 272 (1981)].

Skocpol, W.J., L.D. Jackel, R.E. Howard, H.G. Craighead, L.A. Fetter, P.M. Mankiewich, P. Grabbe, and D.M. Tennant, Surf. Sci. **142**, 14 (1984).

Stephens, R.B., Phys. Rev. B **8**, 2896 (1973).

Stone, A.D., Phys. Rev. B. **39**, 10 736 (1989).

Stone, A.D. and A. Szafer, IBM J. Res. Dev. **32**, 384 (1988).

Thouless, D.J., Phys. Rep. **13**, 93 (1974).

Thouless, D.J., Phys. Rev. Lett. **39**, 1167 (1977).

Umbach, C.P., C. Van Haesendonck, R.B. Laibowitz, S. Washburn, and R.A. Webb, Phys. Rev. Lett. **56**, 386 (1986).

Umbach, C.P., S. Washburn, R.B. Laibowitz, and R.A. Webb, Phys. Rev. B **30**, 4048 (1984).

Van den Dries, L., C. Van Haesendonck, Y. Buynseraede, and G. Deutscher, Phys. Rev. Lett. **46**, 565 (1981).

Vandervoort, K.G., R.K. Zasadzinski, G.G. Galicia, and G.W. Crabtree, Rev. Sci. Instrum. **64**, 896 (1993).

Washburn, S., C.P. Umbach, R.B. Laibowitz, and R.A. Webb, Phys. Rev. B **32**, 4789 (1985).

Webb, R.A., S. Washburn, C.P. Umbach, and R.B. Laibowitz, Phys. Rev. Lett. **54**, 2696 (1985).

Weiss, G., and B. Golding, Phys. Rev. Lett. **60**, 2547 (1988).

Welter, J.M., D. Richter, R. Hempelmann, O. Hartmann, E. Karlsson, L.O. Norlin, T.O. Niinikoski, D. Lenz, Z. Phys. B Con. Mat. **52**, 303 (1983).

Wigner, E.P., Ann. Math. **53**, 36 (1953); **62**, 548 (1955); **65**, 203 (1957); **67**, 325 (1958).

Yamada, K., A. Sakurai, and M. Takeshige, Prog. Theor. Phys. **70**, 73 (1983).

Zaitlin, M.P. and A.C. Anderson, Phys. Stat. Sol. **B71**, 323 (1975).

Zeller, R.C. and R. O. Pohl, Phys. Rev. B **4**, 2029 (1971).

Ziman, J.M., *Electrons and Phonons; the Theory of Transport Phenomena in Solids*, Oxford : Clarendon Press, 1960.

Zimmerman, N.M., B. Golding, and W.H. Haemmerle, Phys. Rev. Lett. **67**, 1322 (1991).